THE DEVELOPMENT OF THE SURFACE GEOMETRY INVERSION METHOD WITH APPLICATIONS TO MODELLING SEAFLOOR HYDROTHERMAL ALTERATION AND ASSOCIATED MINERALIZATION

by

Christopher George Galley

B.Sc. University of Victoria, 2015

A thesis submitted to the School of Graduate Studies
in partial fulfillment of the requirements for the
degree of Doctor of Philosophy

MEMORIAL UNIVERSITY

Department of Earth Sciences
Memorial University of Newfoundland

January 2022

Abstract

As the exploration and exploitation of seafloor polymetallic deposits appears to be the next frontier in mineral exploration, developing and optimizing remote sensing methods to locate and study these deposits is becoming increasingly important for understanding the resource potential and environmental implications of mining from the deep seafloor. One such deposit type is seafloor massive sulfide (SMS) deposits, which form on and below the seafloor at sites of high-temperature hydrothermal fluid venting at a variety of tectonic settings where seafloor extension and magmatism takes place. SMS deposits have promise to offer new sources of Cu, Zn, Pb, Au, and Ag, but the remote environment in which they are located creates difficulties for their discovery and resource estimates. In particular, the proportion of ore found below the seafloor, versus that found within the sulfide mound, has only been estimated from a limited number of collected drillcores. These cores are expensive, with respect to time and money, and unless collected in large numbers, and to sufficient depth, offer limited geometric information of the subseafloor components of the deposit. Alternatively, magnetic voxel-based inverse models can be used to locate SMS deposits as magnetic lows, due to the hydrothermal fluids stripping much of the magnetite from the alteration zone, and the data can be inverted with a surface geometry inverse (SGI) modelling method to resolve subseafloor structures. Additionally gravity inverse models can be used to model the SMS deposits' massive sulfide layer as a density high. The SGI method inverts for the position of nodes in a wireframe mesh rather than physical properties within a fixed mesh. This thesis demonstrates the SGI method to be an excellent tool for modelling the contact surfaces between the sulfide mound, the hydrothermally altered chloritized basalt, and least altered basaltic host rock. The volumes within these surfaces can then be used to calculate an estimated tonnage for the ore located below the seafloor, developing a better resource model for SMS deposits.

General Summary

Seafloor massive sulfide (SMS) deposits, commonly known as "black smoker" hydrothermal vents, are polymetallic deposits that form on the ocean floor. As they form in remote environments, far below sea level where there's no natural light and high water pressures, their discovery and study can be very challenging. In particular, determining the amount of metals contained within the deposits can be hard, and seafloor drilling is often relied on. Drilling on the ocean floor is difficult and expensive, often leading to few, shallow core samples being recovered from SMS deposits that are used to model the rest of the deposit. Additionally, the recovery rate of core samples from SMS deposits is low, often $<20\%$, further restricting the information that can be gathered from drillcore. To improve our ability to model SMS deposits this thesis presents a geophysical data based workflow that can model both the deep crustal alteration beneath these SMS deposits, as well as the rock units of the deposit itself in 3D. Geophysical data can be collected above the seafloor at a fraction of the price of drilling, and through inverting the data 3D models can be made to enhance our understanding of the geometry of SMS deposit below the seafloor. In particular the thesis presents the novel surface geometry inversion (SGI) modelling method that solves for a discrete, 3D wireframe model of the target SMS deposit that can be used instead of or in conjunction with sparse seafloor drilling to develop accurate deposit scale models.

Acknowledgements

I would like to thank Colin Farquharson, John Jamieson, and Peter Lelièvre for all their teaching and support throughout the degree. I would not be the scientist I am today without their guidance, and will always be grateful. I am also thankful for the help of my parents and partner in proof-reading drafts of the thesis, which was rather tedious.

My thanks also goes out to Peter Kowalczyk at Ocean Floor Geophysics, Maurice Tivey and Robert Evans at Woods Hole Oceanographic Institute, John Parianos at Deep Sea Mining, Amir Haroon, Sven Petersen, and Sebastian Graber at GEOMAR Helmholtz Centre for Ocean Research Kiel, Florent Szitkar at the Norwegian Geologic Survey, Isobel Yeo at the UK National Oceanographic Center, and Mark Hannington at the University of Ottawa for all their support and guidance throughout the projects conducted in my time as a PhD student.

I would also like to respectfully acknowledge the territory in which I performed my research as the ancestral homelands of the Mi'kmaq and Beothuk.

Contents

List of Figures

Co-Authorship Statement

The work presented in this thesis is primarily my own, except as outlined below.

Chapter 2: Voxel-based Regional Hydrothermal Alteration Inverse Modelling: East Manus Basin

This chapter presents the first three-dimensional empirical model of a hydrothermal upflow zone in seafloor crust. The concept for the study was developed by Dr. Jamieson and myself, with Dr. Lelièvre and Dr. Farquharson providing guidance throughout the modelling process and interpretation. Mr. Parianos provided the data necessary to complete the study, and assisted with the model interpretation. I performed all the inversion modelling, synthesized all the available geologic and geophysical data in the study region and wrote the manuscript. The manuscript was proof-read and edited by Dr. Jamieson, Dr. Lelièvre and Dr. Farquharson. This chapter is derived from the publication:

Galley, C.G., Jamieson, J.W., Lelièvre, P.G., Farquharson, C.G., Parianos, J.M. Magnetic imaging of subseafloor hydrothermal fluid circulation pathways. Sci. Adv. 6, eabc6844 (2020).

Chapter 3: Surface Geometry Inverse Modelling

In this chapter the updated Surface Geometry Inversion (SGI) method is introduced and its capabilities demonstrated through a series of synthetic modelling examples. The concept for the study was developed by Dr. Lelièvre and Dr. Farquharson, with Dr. Lelièvre writing the majority of the code that makes up the program. Upon joining the project the program was functioning, but did not have the capability to detect self-intersecting models and therefore was limited in the complexity of the target geometries it could solve for. I assisted in developing and implementing the self-intersection detection system by incorporating multiple intersection test options into the program. My main contribution to the project was optimizing the modelling workflow to determine how to best implement the SGI method. This chapter was derived from the publication:

Galley, C.G., Lelièvre, P.G., & Farquharson, C.G. (2020). Geophysical inversion for 3D contact surface geometry. Geophysics, 85(6), 1-76.

The publication's writing done by Dr. Lelièvre and myself, with Dr. Lelièvre compiling the manuscript's introduction and most of the discussion with the example section and associated sections in the discussion being written myself.

Chapter 4: Local Hydrothermal Alteration Modelling; Trans-Atlantic Geotraverse Active Mound

This chapter outlines the application of the Surface Geometry Inversion method as applied to magnetic and gravity data collected over the Trans-Atlantic Geotraverse seafloor massive sulphide deposit. Dr. Haroon provided the magnetic and bathymetric data and Dr. Evans provided the gravity data. Dr. Haroon, Mr. Graber, and Dr. Szitkar provided guidance on the data processing, with Dr. Jamison, Dr. Farquharson and Dr. Petersen providing guidance with the model interpretation. The modelling and manuscript writing was done myself.

Galley, C.G., Lelièvre, P., Haroon, A., Graber, S., Jamieson, J.W., Szitkar, F., Yeo, I., Farquharson, C., Petersen, S. and Evans, R.L., 2021. Magnetic and Gravity Surface Geometry Inverse Modelling of the TAG Active Mound. Earth and Space Science Open Archive ESSOAr (accepted to the Journal of Geophysical Research: Solid Earth).

Chapter 1

Introduction

This chapter reviews the background material that corresponds to the research in the thesis' chapters 2-4. The review begins with a description of the research's main target of study: the seafloor hydrothermal system and the seafloor massive sulfide deposits that they can form. The system's physical properties are then described, explaining how they are anomalous relative to the surrounding seafloor and how magnetic and gravity surveys can collect data, which can be subsequently modelled to study these anomalies using magnetic susceptibility and density. Lastly, this introduction will review the voxel inverse modelling method, which was used create the geophysical models.

1.1 Seafloor Massive Sulfide Deposits

Modern seafloor hydrothermal systems are created along spreading centers or other areas of active volcanism, such as those associated with actively subducting oceanic and submarine-continental tectonic plates (Herzig and Hannington, 1995; Ohmoto, 1996; de Ronde et al., 2001; Huston et al., 2010; Hannington et al., 2011). In these areas, heat from shallowly emplaced subvolcanic intrusions drives convecting cells of seawater within the porous oceanic crust (Fig. 1.1) (Ohmoto, 1996; Hasenclever et al., 2014). The heated convecting seawater progressively reacts with the surrounding oceanic crustal rocks and sediments, resulting in its transformation from a mildly alkali solution to a low pH, high temperature, reduced fluid capable of stripping metals and sulfur (Janecky and Seyfried, 1984). Faulting of the ocean crust classically found around spreading centers and areas of volcanism allow these fluids to migrate upwards to the seafloor along more

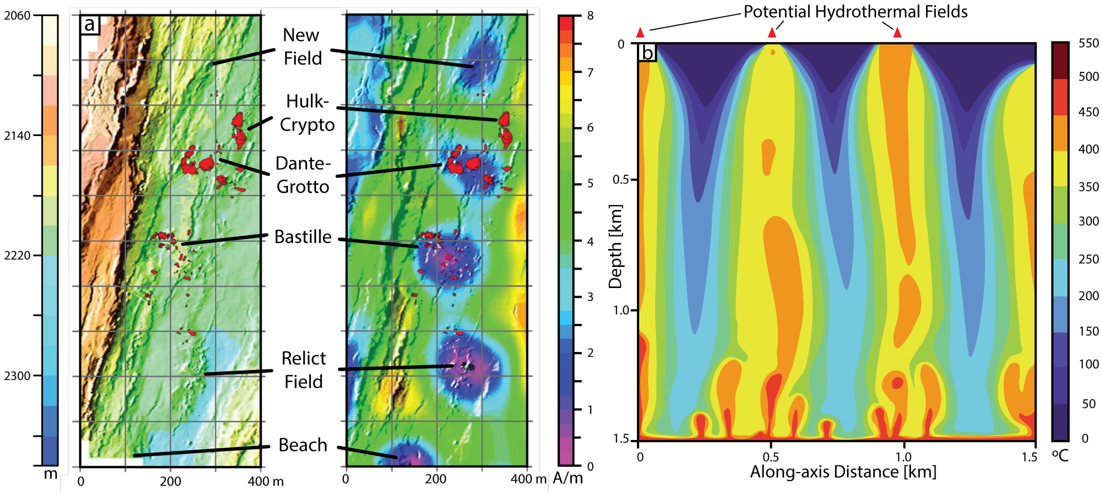

Figure 1.1: a) Bathymetric and magnetization maps of a section of the Endeavour vent field, Pacific Ocean, with venting sites labelled. Note the periodicity of the location of the venting sites. b) A numerical simulation of the hydrothermal circulation in the oceanic crust below the Endeavour vent field, reproducing the periodicity of hydrothermal upflow zones along the spreading axis. Modified from Fontaine et al. (2011) and Tivey and Johnson (2002).

focused pathways, as well as allowing the drawn-in seawater to reach greater depths into the crust during circulation (Hannington et al., 1995). As the hot (measured up to 403 °C; Von Damm et al. 1995) and acidic mineral solution ($3-4\,pH$; Hannington et al. 2005a) comes into contact with the cool (2 °C, $8\,pH$) seawater of the ocean (Chester and Jickells, 2012) the increase in pH and reduction in temperature cause the solutes to precipitate and form chimney structures (Fig. 1.2). The precipitant most commonly forms into metallic sulfides: pyrite (FeS_2), chalcopyrite ($CuFeS_2$), sphalerite (ZnS), as well as anhydrite, silica, and minor clay minerals (Knott et al., 1998b).

Over time, these sulfide-rich chimneys grow, crumble due to mechanical and thermal instability, and grow again, gradually developing a mound of sulfide debris surrounding the active chimney. The massive sulfide/ sulfate (massive by definition in having a $>60\,\%$ composition of sulfide) mound acts as an insulating layer, allowing the hydrothermal fluids to precipitate metals and associated sulfates and silicates within it, building and infilling the mound (Humphris et al., 1995). Below the mound, a high temperature alteration zone develops within the host basalt, resulting in a brecciated, sulfide-silica rich stockwork vein system (Galley et al., 2007). The result is a mature hydrothermal system, with active chimneys, a metal rich massive sulfide mound, and the underlying stockwork system of altered host rock, usually basalt, or more rarely ultramafics to felsic volcanic rocks (Fig. 1.3).

As modern equivalents to volcanogenic massive sulfide (VMS) deposits, SMS deposits may one

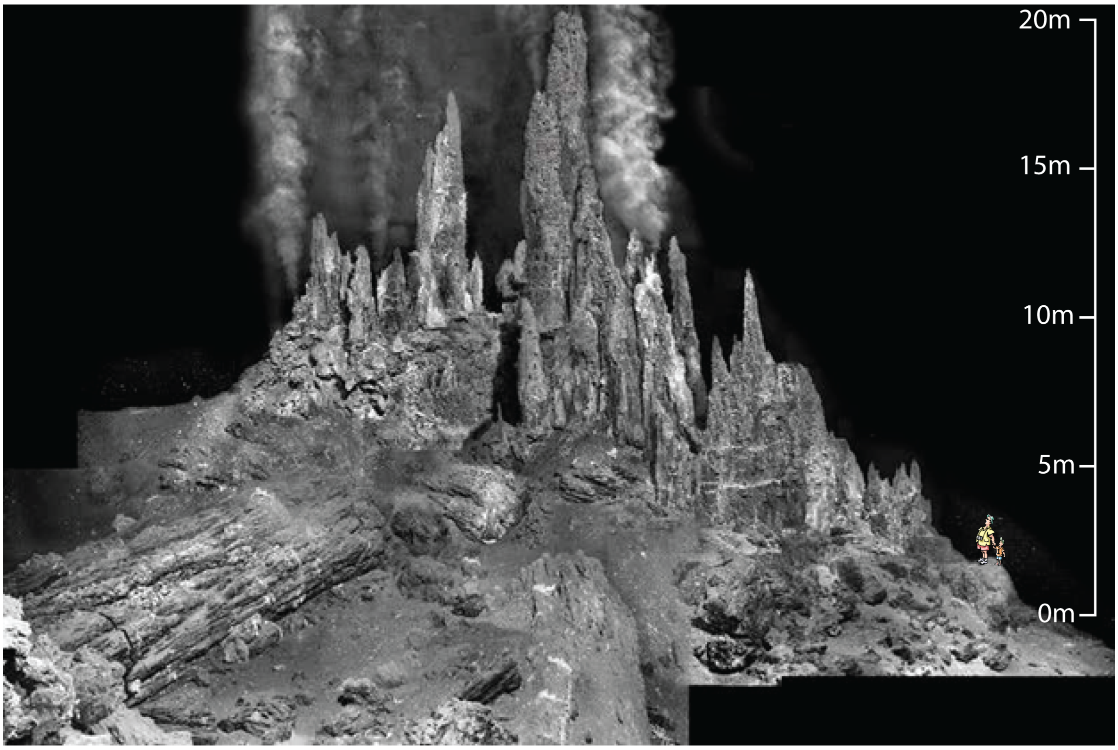

Figure 1.2: A composite image of the Faulty Towers hydrothermal vents from the Mothra hydrothermal field located on the Endeavour Segment of the Juan de Fuca Ridge. The high-temperature venting chimneys reach heights of 10 m at this location. Modified from Glickson et al. (2007).

day also be an economic source of precious and base metals (Hannington et al., 2010). The remote and challenging environment where SMS deposits form have made their mining technologically difficult, and as of yet the extraction of metals from these deposits has not been demonstrated to be economic. However, there is still great value in mapping out the locations of SMS deposits, and developing methods to estimate their size and tonnage (Petersen et al., 2016).

From a geophysical perspective, relative to the surrounding seafloor, SMS deposits are anomalous with respect to magnetic susceptibility and magnetization (Szitkar et al., 2014a,b), density (Evans, 1996; Murton et al., 2019), and conductivity (Spagnoli et al., 2016; Haroon et al., 2018; Gehrmann et al., 2019). Mafic and bimodal-mafic/felsic hosted SMS deposits are anomalously low in magnetization and magnetic susceptibility (Kowalczyk, 2011; Szitkar et al., 2014a), with ultramafic hosted systems having a magnetite enriched stockwork zone (Szitkar et al., 2014b). The deposits' massive sulfide layer has anomalously high density compared to the rest of the deposit and host rock (Evans, 1996). The massive sulfide lens, along with the stockwork zone, is also a conductivity high as a result of their metal contents (Rona et al., 1998; Gehrmann et al., 2019).

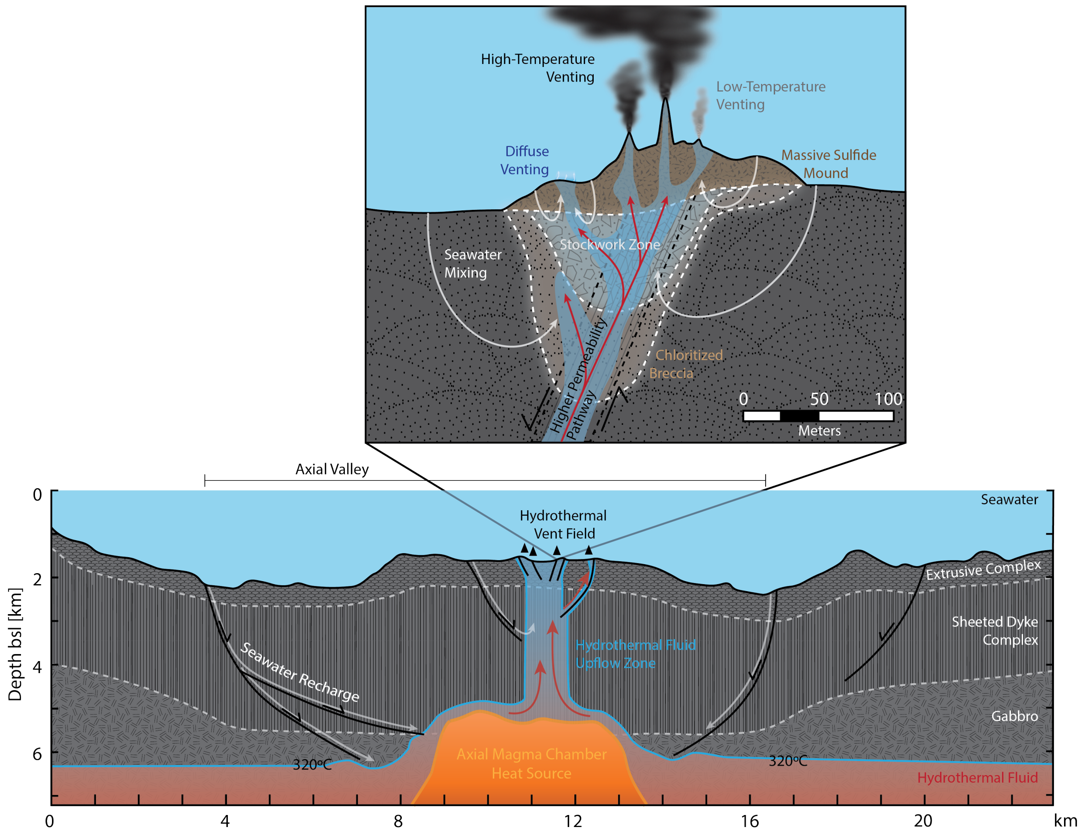

Figure 1.3: Above: an inset model representation of an idealized extrusive rock-hosted seafloor massive sulfide deposit. Below: a cross-section displaying the convective circulation of seawater and hydrothermal fluid which feeds the SMS vent field, driven by an axial magma chamber-like heat source.

1.2 Magnetism of the Seafloor

The study of seafloor magnetism, which is the analysis of the petrophysical properties of seafloor rocks as well as the magnetic fields they produce, has been integral to advancements in the fields of plate tectonics and seafloor setting kinematics (Vine and Matthews, 1963). This section outlines the primary magnetic minerals found in oceanic crust, and factors that affect their magnetic properties and abundance. The magnetism of the three main seafloor tectonic settings: mid-ocean ridges, back-arc basins and island-arc settings, and sedimented ridges and related rifts, are also discussed.

1.2.1 Magnetism

The magnetism of a material is a general term used to describe its magnetization, that is a vector field defined by the density of magnetic moments in the material (Griffiths, 2005). The magnetization of a rock is defined by two types: induced and remanent magnetization.

Induced magnetization

Induced magnetization is created in a material while in the presence of an external magnetic field. In the macroscopic sense, the motion of electrons about their atoms can be approximated as the atom having a single current loop, developing in a magnetic dipole (Griffiths, 2005). An external field, also referred to as the inducing field, can apply a torque to the potentially randomly oriented magnetic moments in the material, causing them to align with the inducing field and create a secondary magnetic field. The magnitude of the induced magnetization depends on a number of factors, such as the number of unpaired valence electrons and the natural ordering of the material's atomic lattice, but for macroscopic analysis of bulk materials it can be simply quantified by the parameter magnetic susceptibility, χ:

$$\mathbf{M}_{ind} = \chi \mathbf{H}. \tag{1.1}$$

As shown in Eq. 1.1, magnetic susceptibility is a dimensionless scalar used to describe the strength of the induced magnetization, $\mathbf{M}_{ind}$, relative to the strength of the inducing field, $\mathbf{H}$. In cases where $\chi > 0$ the material is called paramagnetic, and a material is diamagnetic when $\chi < 0$. Most minerals are paramagnetic, and those that are diamagnetic have very low magnetic susceptibilities, such as quartz (-14×10^{-6} SI, Hrouda and Kapička 1986) and calcite (-12.09×10^{-6} SI, Schmidt et al. 2006), that have comparable diamagnetic properties to seawater (-9×10^{-6} SI, Müller et al. 2012).

Remanent magnetization

Remanent magnetization is the vector field produced from the sum of magnetic moments in a rock in the absence of any external magnetic field. This magnetization can form during the crystallization of the rock (thermoremanent magnetization), where the vector direction of the magnetization remains in line with the Earth's magnetic field at the time of formation (Girdler and Peter, 1960). It can also form from chemical alteration (chemical remanence), which leads to the crystallization of secondary magnetic minerals (Kobayashi, 1959). During the formation of the secondary magnetic minerals, their magnetic moments will align themselves with the Earth's magnetic field. The last major type of remanence is depositional remanence, developed in layers of sediments as they fall through the water column (Collinson, 1965). Fragments of magnetic minerals will align themselves with the Earth's magnetic field as they and the other sediments drift through the water column, as they are free to rotate in the liquid. When the sediments came to rest on the seafloor, they do so in the direction of the Earth's magnetic field.

Remanent magnetization will remain in place unless some energy is added to the system to permanently alter the direction of the rock's magnetic moments (Dunlop and Özdemir, 2001a). This can be caused by raising the temperature of the rock past its Curie point, which thermally alters the rock to allow its magnetic minerals to change their alignment. Alternatively, in the case of depositional remanence, some mechanical force can agitate the sediments, physically rotating the magnetic mineral fragments.

While in the presence of an external magnetic field a material containing remanent magnetization will have an anisotropic magnetic susceptibility as there will be a preferred orientation of the induced field in the direction of the remanent magnetization. In this case Eq. 1.1 can be generalized as the magnetic susceptibility being a tensor, rather than a scalar (Uyeda et al., 1963).

Curie Temperature

A certain amount of order in a material's magnetic moments are required for a macro-scale magnetization to be present. With regards to both induced and remanent magnetizations, a material's magnetic domains share a common alignment, through either an external field's influence or a past external field that aligned the domains as the material was formed. In the scenario that a material is heated such that the oriented ions' magnetic moments responsible for the magnetization become randomized, due to the system's increased energy, then a material can lose its magnetization. The temperature when this loss of magnetization occurs is the Curie Temperature, which can vary between materials (see Fig. 1.5b for an example of how the composition of an iron-titanium oxide's ions can affect its Curie Temperature).

1.2.2 Rock magnetism

Magnetic minerals

Iron oxides are the main magnetic minerals found within the oceanic lithosphere (Ozima and Larson, 1970; Irving, 1970; Watkins and Paster, 1971; Marshall and Cox, 1972; Shau et al., 2004; Szitkar et al., 2014a; Szitkar and Murton, 2018). Many of these oxides on the seafloor take the form of titanomaghemites,

$$Fe^{3+}_{8/3-2x}Fe^{2+}_{x}Ti^{4+}_{x}\square_{1/3}O^{2-}_{4} \tag{1.2}$$

$0 \leq x \leq 1$ and $\square$ indicating vacancy in the lattice (Stacey, 2012), but unoxidized titanomagnetite,

$$Fe^{3+}_{2-2x}Fe^{2+}_{1+x}Ti^{4+}_{x}O^{2-}_{4}, \tag{1.3}$$

contributes the most to the magnetization of oceanic lithosphere due to the greater magnetic moment magnitudes of the mineral (O'Reilly and Banerjee, 1967; Stacey, 2012).

Iron-titanium oxides are paramagnetic, but can be further classified as ferrimagnetic. Ferrimagnetic materials have positive magnetic susceptibilities, but all neighbouring magnetic moments within the material's atomic lattice are anti-parallel, see Fig. 1.4 for the structure of the titanomagnetite spinel. Titanomagnetite spinels are composed of two sublattices: a tetrahedral sublattice made up of Fe^{2+} or Fe^{3+} ions and four oxygen atoms, typically referred to as the

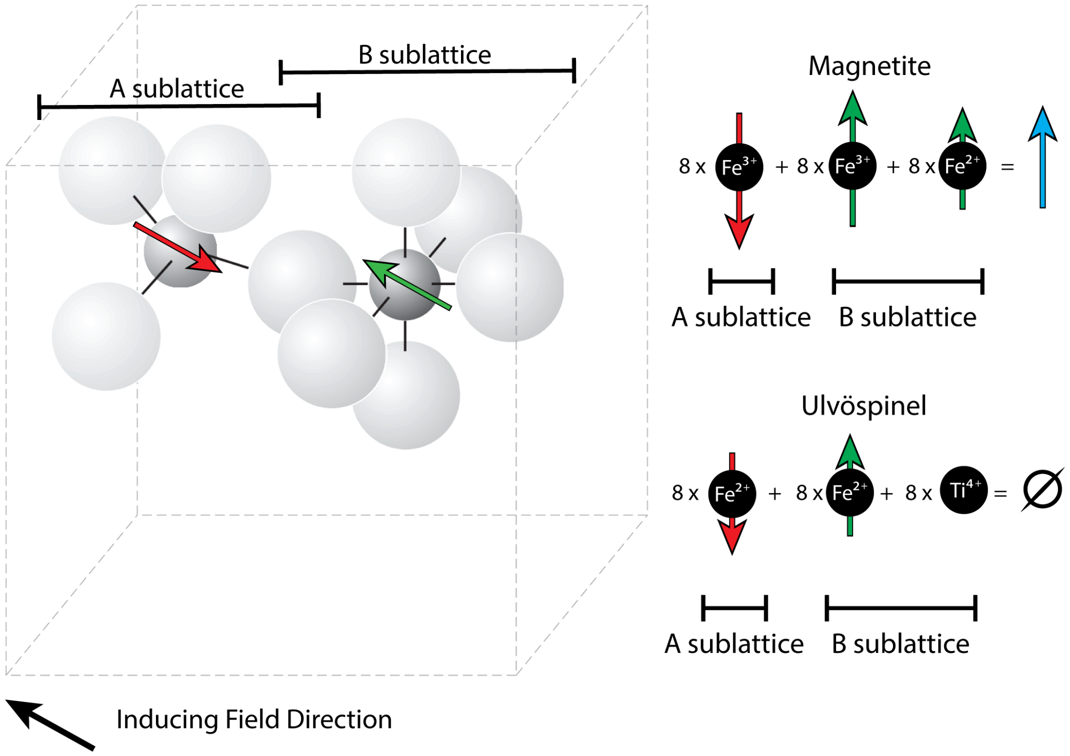

(a) (b)

Figure 1.4: The spinel structure of a titanomagnetite and the ordering of its magnetic moments. (a) The lattice contains eight tetrahedral (A) sublattice groups and 16 octahedral (B) sublattice groups, but just one of each are shown for the purposes of visualization. (b) Two examples of the magnetic moment ordering of the two sublattice groups, for magnetite and ulvöspinel. Adapted from Dunlop (1990).

A sublattice; and an octahedral group composed of Fe^{2+}, Fe^{3+}, or Ti^{4+} ions and six oxygen atoms, referred to as the B sublattice. The magnetic moments of the A and B sublattices are anti-parallel, leading to the mineral's ferrimagnetic properties. Therefore, the magnetization of a titanomagnetite spinel unit, composed of eight A sublattices and 16 B sublattices, depends on the distribution of cations within both sublattices. Using the two end members of the titanomagnetite group as examples, seen in Fig. 1.4, the Fe^{3+} cations from both sublattices will have their magnetic moments cancel out in a magnetite crystal, leaving the magnetic moment of the Fe^{2+} in the B sublattice to produce the observed magnetism. Ulvöspinel, the other titanomagnetite end member, is not magnetic as the titanium cations have replaced half the iron cations in the B sublattice, leading to a complete cancellation of the magnetic moments from the remaining Fe^{2+} in the B sublattice and the Fe^{2+} in the A sublattice (Orlický, 2010).

Additionally, increased oxidation of a given titanomagnetite lattice will decrease its magnetization. Referred to as maghemitization, the oxidation of titanomagnetite causes a replacement of its Fe^{2+} cations with Fe^{3+} cations and vacancies:

$$Fe^{3+}_{2-2x+(2/3)y}Fe^{2+}_{1+x-y}Ti^{4+}_{x}\square_{y/3}O^{2-}_{4}, \tag{1.4}$$

$0 \leq y \leq 1$.

As the degree of oxidation increases, the number of vacancies leads to the reordering of the crystal lattice, forming a more tightly packed, stable cubic lattice of titanomaghemite. The A sublattices of titanomaghemite are filled with Fe^{3+} cations, and the B sublattice is composed of the remaining Fe^{2+}, Ti^{4+}, and vacancies. As with titanomagnetite, there are eight A sublattices and 16 B sublattices, with their magnetic moments oriented anti-parallel. Unlike titanomagnetite, a higher content of titanium in titanomaghemite will lead to an increase of its magnetic properties, as the additional Fe^{2+} and Ti^{4+} decrease the magnetic moment of its B sublattice, while leaving the moment of the A sublattice unchanged.

The main parameters causing variation in the magnetization of oceanic lithosphere is then the amount of Fe-Ti oxides present, the amount of titanium in the Fe-Ti oxides, and the oxides' degree of oxidation.

Alteration processes

A prominent factor that governs the amount of titanomagnetite and titanomaghemite in a seafloor rock is the degree and type of alteration the rock has undergone. Hydrothermal convection draws seawater deep into the upper oceanic lithosphere, allowing oxidation to be an ongoing alteration process. At low temperatures (< 200°C), titanomagnetite oxidizes to the less magnetic titanomahemite (Ade-Hall et al., 1971; Watkins and Paster, 1971; Petersen et al., 1979; Worm and Banerjee, 1984; Johnson and Pariso, 1987). The degree of oxidation of the iron minerals is defined as the parameter z in

$$Fe^{2+} + \frac{1}{2}(z)O \rightarrow (z)Fe^{3+} + (1-z)Fe^{2+} + \frac{1}{2}(z)O^{2-}, \tag{1.5}$$

with $0 < z < 1$ (O'Reilly and Banerjee, 1967). See Fig. 1.5 for a ternary diagram visualizing the oxidation, z, and titanium content, x, parameters.

This low temperature oxidation (maghemitization) occurs continuously after the formation of the titanomagnetite bearing igneous rock, leading to a continuous decrease in the magnetization of the rock with time (Irving, 1970). As an analogue for time passed, the degree of maghemitization can also be observed as increasing with distance from a spreading ridge (Irving, 1970; Marshall and Cox, 1972; Sempere et al., 1988).

In addition to the continuous maghemitization described by Eq. 1.5, titanomagnetite bearing seafloor rocks also undergo further maghemitization when in contact with circulating low-pH hydrothermal fluids in the upper crust (Hannington et al., 2005b),

$$Fe^{3+}_{2-2x}Fe^{2+}_{1+x}Ti^{4+}_{x}O^{2-}_{4} + aH^{+} \rightarrow Fe^{3+}_{2-2x+a}Fe^{2+}_{1+x-(3/2)a}Ti^{4+}_{x}O^{2-}_{4} + \frac{a}{2}Fe^{2+} + \frac{a}{2}H_2, \tag{1.6}$$

for $0 \leq a \leq \frac{2+2x}{3}$ (Worm and Banerjee, 1984). The alteration of titanomagnetite, with respect to Eq. 1.5 and the amount of titanium present, x, can be visualized in the ternary diagram of Fig. 1.5. The dissolution of titanium into the hydrothermal fluids,

$$Fe^{3+}_{2-2x}Fe^{2+}_{1+x}Ti^{4+}_{x}O^{2-}_{4} + 4xH^{+} + 4(1-x)H_2O \rightarrow (1+x)Fe^{2+} + 2(1-x)Fe(OH)^{-}_{4} + xTi(OH)^{0}_{4}, \tag{1.7}$$

also plays a significant role in lowering the magnetic properties of hydrothermally altered rock (Wang et al., 2020).

With regards to ultramafic lithosphere (primarily composed of peridotite, which in turn is mainly composed of olivine and pyroxene, Green and Ringwood, 1963), serpentinization is an important alteration process that effects its magnetism. If olivine is exposed to hydrothermal fluids it will undergo serpentinization, which produces magnetite (Charlou et al., 2013; Szitkar et al., 2014b; Szitkar and Murton, 2018):

$$5\underbrace{Mg_2SiO_4}_{olivine} + FeSiO_4 + 9H_2O \rightarrow 3\underbrace{Mg_3Si_2O_5(OH)_4}_{serpentine} + \underbrace{Mg(OH)_2}_{brucite} + \underbrace{2Fe(OH)_2}_{ferrous\,hydroxide}, \tag{1.8}$$

$$\underbrace{3Fe(OH)_2}_{ferrous\,hydroxide} \rightarrow \underbrace{Fe_3O_4}_{magnetite} + H_2 + 2H_2O. \tag{1.9}$$

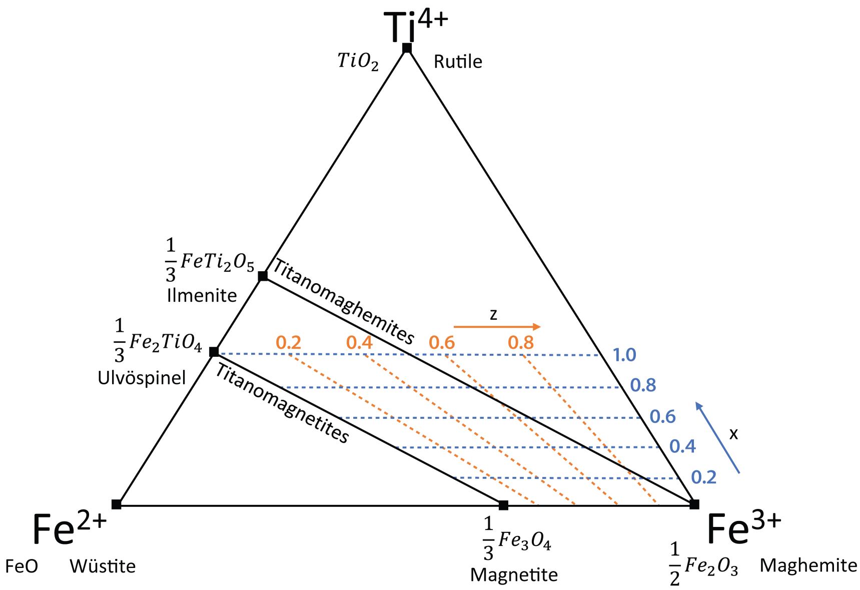

(a)

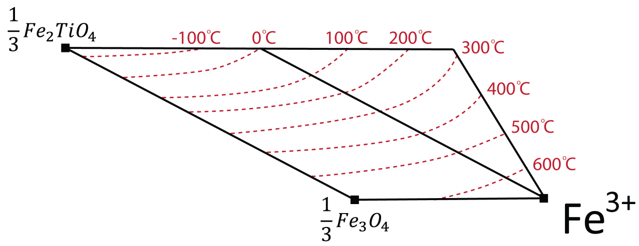

(b)

Figure 1.5: Ternary diagram of the iron-titanium oxides. (a) In orange the degree of oxidation is plotted, and in blue the titanium content in the titanomagnetite series is plotted, adapted from Dunlop (1990). (b) The $(0 \leq x \leq 1) \cup (0 \leq z \leq 1)$ section of the iron-titanium ternary diagram showing Curie temperature isothermal lines, adapted from Readman and O'Reilly (1972)

During high-temperature serpentinization ($>\sim$ 200°C), the reactions of Eq. 1.8 and 1.9 favor the production of magnetite over the less magnetic brucite ($Mg(OH)_2$) (Klein et al., 2014; Szitkar and Murton, 2018), with the opposite being true at low temperatures ($<\sim$ 200°C). The proportion of magnetite vs. brucite production during serpentinization has been observed to not share a linear relationship with temperature and alteration level, but rather increases rapidly past $\sim$ 200°C (Szitkar and Murton, 2018).

An additional product of the high-temperature reaction of Eq. 1.9 is hydrogen, which plays an important role in the preservation of the magnetic minerals as it reduces the rate of magnetite oxidation (Charlou et al., 2013). The serpentinization of ultramafic seafloor rock therefore both increases the amount of magnetic minerals and subsequently preserves them against maghemitization.

1.2.3 Seafloor tectonic settings

Mid-ocean ridges

Mid-ocean ridges (MORs) are sites of major extension along the seafloor, a result of the translation of tectonic plates, where the opening of the crust has led to the production of new seafloor from the uprising magma (Sinton and Detrick, 1992). As these settings are primarily composed of young mafic igneous rock, with minor sediment coverage, they have, on average, higher magnetization than the rest of the seafloor (i.e. the younger basalt has experienced less maghemitization) (Irving, 1970; Marshall and Cox, 1972; Sempere et al., 1988).

Mafic volcanic rocks are magnesium and iron rich igneous rocks with less than 53 $wt.\%$ SiO_2 (Le Bas and Streckeisen, 1991), and are most commonly deposited on the seafloor as basalts. In unaltered basalts, the titanium content of titanomagnetite crystals (x) tend to be in the range of $0.54 - 0.67 \pm 0.05$ (Johnson and Hall, 1978; Wang et al., 2020). Intrusive mafic rocks typically include gabbros and dolerite dykes, which are similar in chemical composition to the extrusive basalts but coarser grained (Le Bas and Streckeisen, 1991). Magnetic studies have determined the magnetic mineral composition of gabbro samples below the seafloor to be of primarily low-Ti titanomagnetites, compared to basalts, as the Curie temperature is $560 - 580$°C (see Fig. 1.5b for relationship between Curie temperature and Ti content) (Kikawa and Pariso, 1991). See Fig. 1.6 for an outline on the general composition of the seafloor at mid-ocean ridges.

MORs are often classified based on their spreading rate: fast, intermediate, slow, and ultraslow (Ridge, 2001). To further outline the magnetic properties of MORs, they will be split into two classifications: fast/intermediate spreading ridges (> 40 mm/yr), and slow/ultraslow spreading ridges ($10 - 40$ mm/yr, Fig. 1.6) (Ridge, 2001).

Fast/intermediate-spreading ridges

At fast-spreading ridges the crust is primarily composed of pillow basalt (know as Mid-Ocean Ridge Basalt, MORB), overlying a diabase sheeted dyke complex, which are the feeder dykes to the above basalt flows (Park, 1990). As MORBs cool and solidify on the seafloor, titanomagnetite crystals grow in alignment with the background Earth's field at the time of cooling, creating a strong remanent magnetization that is often dominant over the induced magnetization component (Bronner et al., 2014). As explained above, the magnetization of basalt rock at MORs is strongest close to the axis with magnetizations ranging between $10^1 - 10^2$ A/m (Irving, 1970), and diminishes exponentially with distance from the spreading center. With respect to rock in and surrounding SMS deposits the studies of Zhao et al. (1998) and Wang et al. (2020) have shown that one might expect the effective magnetic susceptibilities in this environment to be $0.033 - 0.33$ SI for background basalt and approximately 10^{-5} SI for the deposit. The East Pacific Rise is an example of a fast-spreading MOR that hosts hydrothermal vent fields (e.g. the 13^oN and 21^oN East Pacific Rise vent fields) (Hannington et al., 2011), with Central Indian Ridge and Juan de Fuca being intermediate-spreading ridges hosting the Kairei and Edmond vent field (Gallant and Von Damm, 2006) and the Endeavour Segment (Jamieson et al., 2014a), respectively.

Slow/ultraslow-spreading ridges

Slow-spreading mid-ocean ridges are also primarily composed of MORB, but are more heavily faulted (Buck et al., 2005). In cases where there is limited magmatism and new crust is not created fast enough to accommodate the spreading rate of the diverging plates the crust will undergo extensional deformation. The extension leads to deeper faulting, sometimes creating detachment faults that can expose sections of the lower crust (Fig. 1.6b, c) and/or mantle rock to the seafloor. In these regions of exposed ultramafic seafloor, serprentinization of peridotites leads to an increase in the seafloor's magnetism (Eq. 1.8 and 1.9), due to the development of chemical remanence (Maffione et al., 2014). During serpentinization peridotites develop most of

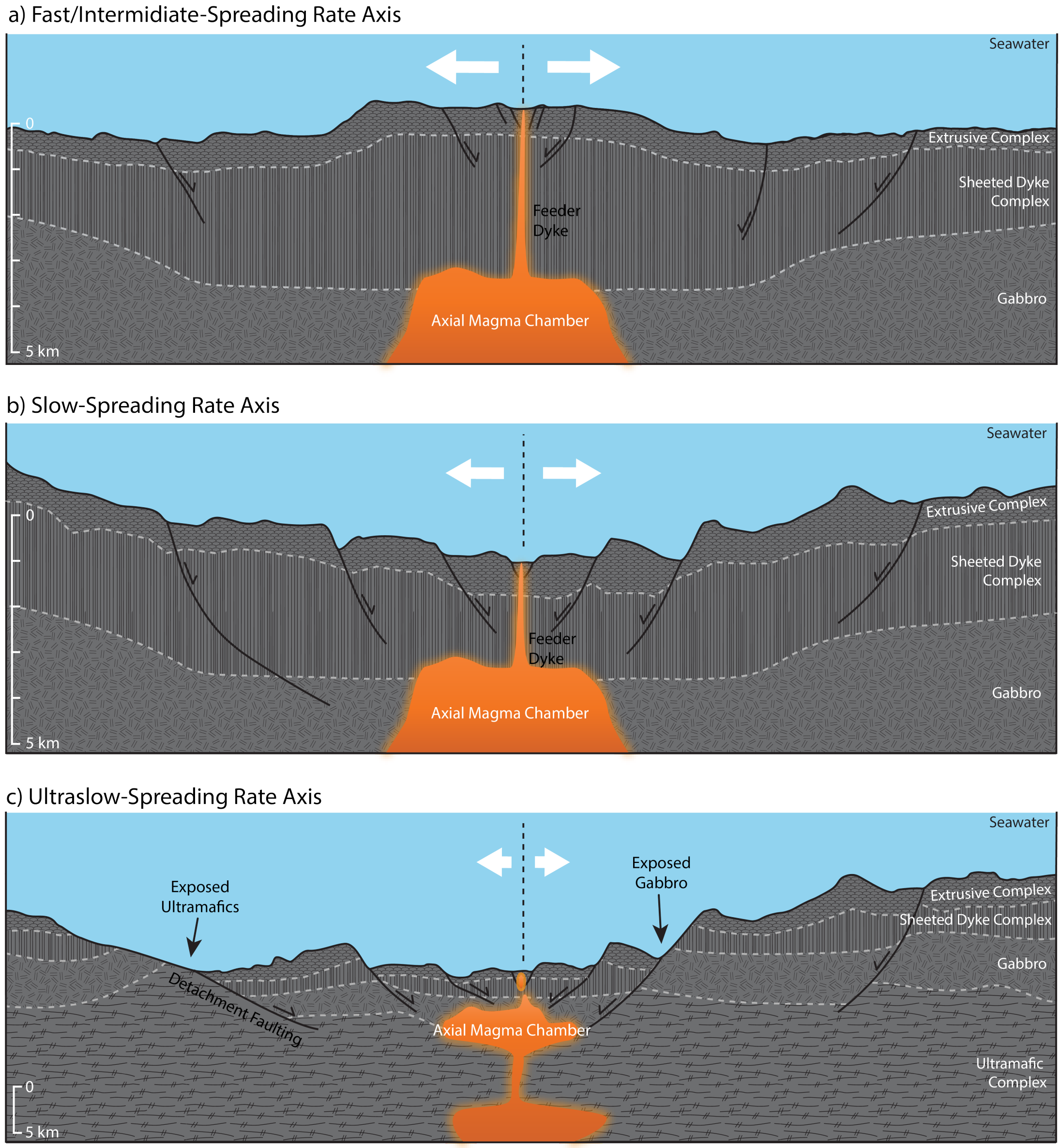

Figure 1.6: Three example cross-sections of seafloor crust. a) A fast/intermediate-spreading axis, b) a slow-spreading axis, and c) an ultraslow-spreading axis.

their magnetization, increasing from < 1 magnetite volume fraction ($m\%$) in unaltered peridotites to approximately 7 $m\%$ (Maffione et al., 2014). Szitkar et al. (2014b) showed that the effective magnetic susceptibility of the host serpentinite is approximately 0.04 SI, $0.1 - 0.36$ SI for the stockwork zone, and approximately 0 SI for the massive sulfide.

Examples of hydrothermal fields hosted by slow-spreading MORs are the Trans-Atlantic Geotraverse and Lucky Strike (Rona et al., 1976; Team et al., 1993). Ultramafic-hosted SMS deposits such as Rainbow, Lost City, Logatchev, and Ashadze have formed along ultraslow-spreading ridge segments of the Mid-Atlantic Ridge (Charlou et al., 1996; Douville et al., 1997; Kelley et al., 2001; Charlou et al., 2010).

Back-arc basins and island-arc settings

Back-arc basins form as a result of a steepening in the angle of oceanic plate subduction causing footwall plate retreat, or “rollback". This results in extension of the overlying plate and basin development behind the magmatic arc (Forsyth and Uyeda, 1975). The bimodel mafic-felsic volcanism typical of back-arc basins is the result of the partial melting of the crust by the upwelling mantle magmas (Letouzey and Kimura, 1985; Martinez and Taylor, 1996; Zhang et al., 2019a). Due to fractional melting and crystallization, the more felsic rocks will contain lower amounts of iron and titanium (Byerly et al., 1976; Yang and Scott, 2002), and as a result will contain less titanomagnetite, decreasing its magnetization compared to the basaltic seafloor rock (Oshida et al., 1992). The Lau Basin and East Manus Basin are two examples of back-arc basins that host SMS systems (Fouquet et al., 1993; Binns and Scott, 1993)

Sedimented ridges and related rifts

Much of the seafloor is covered in sediments, derived from pelagic fallout and/or the eroded sediments from land masses (Hüneke and Mulder, 2011). The sediment thickness varies greatly, from tens of meters over young crust to kilometers next to continental shelves. Sediments contain some magnetite grains, which allows them to gain a depositional remanence, but the grains are in low concentrations and do not usually have the time to fully align with the Earth's field while drifting through the water column. This results in sediments having very low magnetic properties compared to the underlying crustal rock ($\chi = 10^{-5}$ vs. $\chi = 10^{-2} - 10^{-1}$ SI for magnetic susceptibilities, and $DRM < 10^{-3}$ vs. $10^{0} - 10^{1}$ A/m) (Dunlop and Özdemir, 2001b; Font et al., 2005; Liu et al., 2008). These sediments are therefore considered magnetically transparent on the seafloor when in proximity to the much more magnetic volcanic rock (Szitkar et al., 2014a). Additionally, thick sediment cover can act as a thermal insulator, trapping or slowing hydrothermal circulation below it thereby raising the temperature of the underlying crustal rock (Levi and Riddihough, 1986; Hannington et al., 2005b). The increased temperatures can raise the crust above the $100 - 200°$C Curie temperature of the titanomagnetite typically found in seafloor basalt, significantly reducing its magnetization. The Middle Valley hydrothermal field, containing the Bent Hill SMS deposit, is an example of a sedimented-hosted SMS system, located on the northern segment of the Juan de Fuca Ridge (Ames et al., 1993; Zierenberg et al., 1998).

1.3 Magnetic Surveying of the Seafloor

1.3.1 Magnetic Induction

Magnetic field surveys are performed to collect measurements of a magnetized body's magnetic induction, $\mathbf{B}$, to gain knowledge of the sub-surface through understanding variations in its magnetic properties. A magnetized source's magnetic induction is a vector field that represents the density of magnetic flux at a given point in space, produced as a result of the body's magnetization, $\mathbf{M}$,

$$\mathbf{B}(\mathbf{r}) = -\frac{\mu_o}{4\pi}\nabla \iiint_V \mathbf{M}(\mathbf{r}_o) \cdot \nabla_o \frac{1}{|\mathbf{r} - \mathbf{r}_o|} dV_o \tag{1.10}$$

with μ_o being the permeability of free space, $\mathbf{r}$ the measurement location, $\mathbf{r}_o$ the source location, and dV_o an infinitesimal volume segment of the magnetized body of total volume V (Hansen et al., 2005). The SI unit for magnetic induction is the Tesla, which are typically measured as nT in geophysical studies as the field produced by geologic magnetic sources tend to be small.

1.3.2 Total magnetic intensity

A common magnetic measurement collected during surveys is the total magnetic induction, $|\mathbf{B}|$, called the total magnetic intensity (TMI). The TMI can be separated into two components, the geomagnetic field component, $\mathbf{B}_o$, produced by the Earth and the anomalous field component, $\Delta\mathbf{B}$, produced by magnetic sources in the subsurface. As $\Delta\mathbf{B}$ tends to be much smaller than $\mathbf{B}_o$ (orders of 10^0-10^3 compared to 10^4, Dentith and Mudge, 2014), one can define the total magnetic anomaly as:

$$\Delta T = |\mathbf{B}| - |\mathbf{B}_o|, \tag{1.11}$$

leading to the production of total magnetic anomaly maps, that can be used to more easily identify anomalous magnetic bodies in the sub-surface (Dentith and Mudge, 2014).

1.3.3 Multi-component

A multi-component magnetic survey, or magnetic vector survey, is a study that measures three orthogonal components of the magnetic field. Rather than collecting simply the magnitude of a magnetic vector field at a point (TMI), knowledge of the individual Cartesian coordinates of a magnetic field provides information on the orientation of magnetic features (Seama et al., 1993), and is necessary when processing data collected by a automated underwater vehicle (AUV) or a remotely operated vehicle (ROV) to remove system noise (Isezaki, 1986; Honsho et al., 2013). Therefore typically data collection and processing are done using all three components of the magnetic field, with TMI data generated as the product, and then subsequent modelling and interpretation is done on the TMI data.

1.3.4 Fluxgate Magnetometer

Fluxgate magnetometers are devices with the ability to measure both the magnitude and direction of magnetic fields (Auster et al., 2008). To measure the magnitude of an external magnetic field in a single direction, the fluxgate magnetometer uses two coiled wires wrapped around a magnetically susceptible core of metal. An oscillating current, I_{trans}, is applied through one coil of wire, with an amplitude high enough to fully saturate the magnetically susceptible material. The second coil of wire is then used to measure the induced current, I_{ind}, generated in that wire by the electromagnetic force created by the oscillated magnetic field. When there is an external magnetic field, B_{ext}, present, the magnetically susceptible material will reach its saturation magnetization at an off-set time, creating a change in magnetic flux that is measured in the second wire loop (see Fig. 1.7). To measure the three magnetic field Cartesian components, three such fluxgate sensors can be oriented orthogonal to each other.

An example of a magnetometer that can be attached to an AUV is that developed by Ocean Floor Geophysics Inc., which is self-compensating so it automatically filters out system noise, as described further below (see also Fig. 1.8).

1.3.5 Data Processing

After a magnetic data set has been collected, there are a few processing steps that are important to ensure the data is usable for data analysis and modelling. First, if the GPS used to measure the coordinates of the measurement locations was a separate system from the magnetometer, then the magnetic field measurements must be merged with the correct location points. Next the Earth's magnetic field magnitude (or International Geomagnetic Reference Field, IGRF) is removed from the measured data, along with the variations in the geomagnetic inducing field

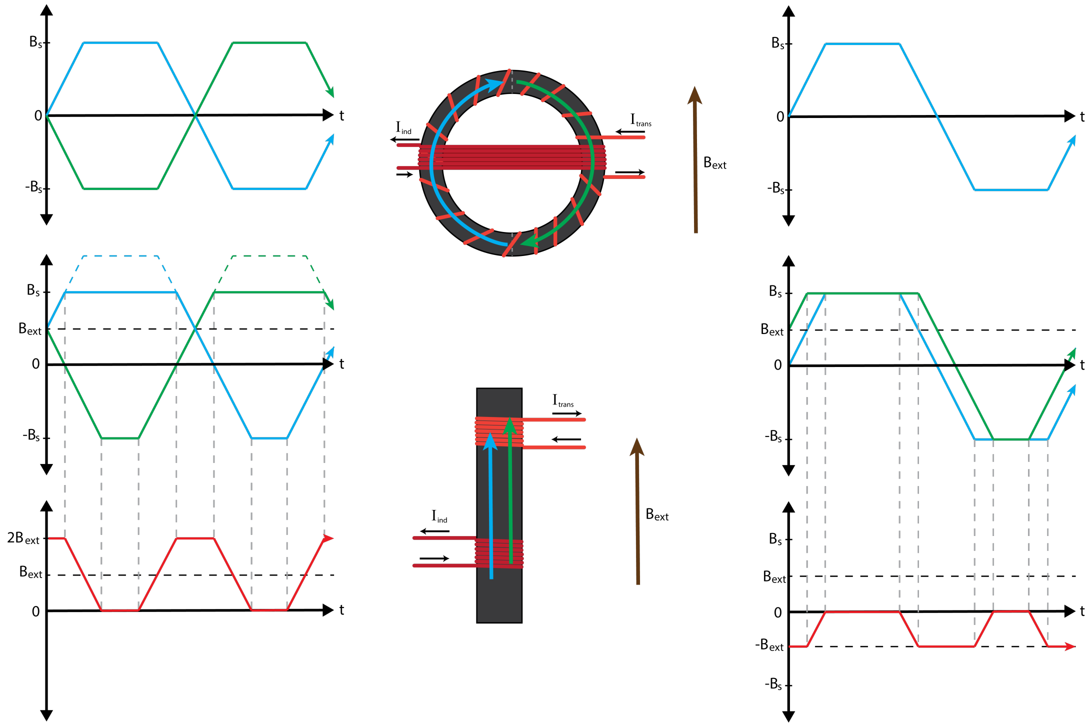

(a) (b) (c)

Figure 1.7: A diagram showing how a fluxgate magnetometer functions. (a) Magnetic field with time plots from the circular magnetic configuration, from top to bottom: the induced magnetic field from both halves of the magnet without an external field present, the induced magnetic field from both halves in the presence of an external field, and the resulting induced field in the direction of the external field. (b) The two fluxgate magnetometer configurations, on top is the circular magnetic configuration, with the bar magnetic on the bottom. (c) The same three magnetic field with time plots from (a), but for the bar magnetic configuration. Image adapted from Kwisanga (2016).

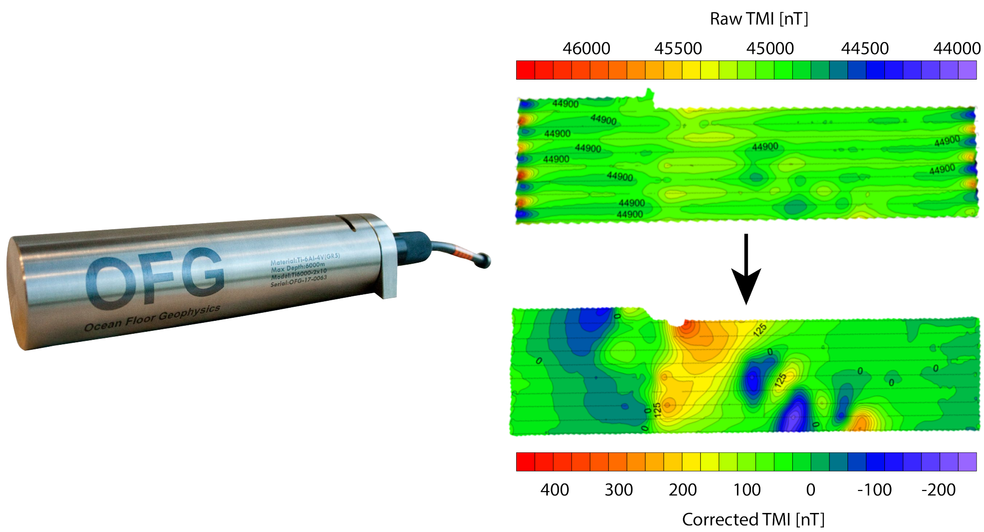

Figure 1.8: An example of a fluxgate magnetometer used during seafloor magnetic surveying. The magnetometer is attached to an AUV during the survey. On the left is the magnetometer in a protective casing, and on the right an example of raw data collected from an AUV magnetometer versus the corrected data. Modified from http://www.oceanfloorgeophysics.com/ofg-scm

as measured by a base station, if used. These variations occur over daily time scales with the presence or lack of the Sun overhead of the field site, as well as over a matter of seconds with the occurrence of solar magnetic storms.

With the IGRF removed, just the anomalous field, $\Delta\mathbf{B}$ is left for further analysis and/or processing. In scenarios where the magnetometer was close to, or attached to, a piece of machinery, such as an aircraft or underwater vehicle (ROV/AUV), additional magnetic effects need to be removed to isolate the secondary magnetic field generated by just the sub-surface features (effects such as the remanent and induced magnetization of the vehicle, Fig. 1.8) (Luyendyk, 1997; Isezaki, 1986; Honsho et al., 2013).

With the magnetic field produced by subsurface sources isolated, filtering methods can be applied to remove undesirable features from the data, such as through low-pass/high-pass filtering, smoothing, and trend removal (Dentith and Mudge, 2014). The definition of a desirable feature is completely dependant on the survey, and what the target of the study is. If larger subsurface bodies (that would produce longer wavelength magnetic signals) are the target of study, then low-pass filtering or smoothing can be applied to the data to remove small wavelength features, better isolating the long wavelength features. In contrast, high-pass filtering can help remove long wavelength features. Generally, though, some amount of small wavelength feature removal is used to help in eliminating noise from the data.

1.4 Gravity Surveying of the Seafloor

As on land, seafloor gravity surveys provide a means of collecting nearer-target data to study the finer density variations within the oceanic crust. Gravity surveys measure variations in the Earth's gravitational field to study these subsurface density distributions. Generally, the gravitational acceleration experienced at a point a distance r from a mass of arbitrary dimensions with constant density ρ and volume V positioned at r_o is

$$\boldsymbol{g}(\boldsymbol{r}) = G\rho\nabla\left(\iiint_V \frac{1}{|r - r_o|}\, dV_o\right) \tag{1.12}$$

with $G = 6.67 \times 10^{-11}$ m^3 kg^{-1} s^{-2} being the gravitational constant. Similar to the magnitude of magnetic fields, gravitational acceleration is linearly proportional to its corresponding physical property (i.e. density). Practically, the vertical component of the acceleration can be measured as it is the easiest to do so (Telford et al., 1990), so Eq. 1.12 can be reduced to

$$g_z(r) = -G\rho \left(\iiint_V \frac{z - z_o}{|r - r_o|^3} \, dV_o \right). \tag{1.13}$$

Gravity surveying at sea began in 1923 by Vening Meinesz (Vening Meinesz, 1929), which was quickly followed by the installation of his gravimeter into a submersible to survey the seafloor and better define the Earth's geoid. By collecting gravity measurements below sea-level, compared to at sea-level on a ship, a gravimeter is more easily stabilized and measurements were able to be collected with better accuracy during Dr. Meinesz's many expeditions. Modern gravimeters have much more sophisticated stabilizing systems, so the issue of loss of accuracy when collecting gravity measurements at sea-level versus below it is no longer an issue. Presently, the main consideration is the desired resolution and scale of the survey. A shipboard gravimeter will be further from the seafloor, and therefore will collect data that is more sensitive to large, deep density features in the crust. Surveys conducted within a submersible have the benefit of being able to rest on the seafloor during the data collection to better detect near-surface density variations in the crust, but this is more of a lengthy process and so the surveys are on a smaller scale.

With respect to SMS exploration, gravity surveys are usually conducted manually from within a submersible (Evans, 1996), by a remotely operated vehicle (ROV) (Sasagawa et al., 2003), or by an autonomous underwater vehicle (AUV) (Shinohara et al., 2015).

Before gravity data can be interpreted there are a number of processing steps that must be done. These steps are not in place to remove noise, but rather to remove real aspects of the data that do not correspond to density variations in the subsurface that are the focus of the analysis.

Latitude Correction

This correction adjusts the gravitation acceleration measurements to offset the spheroidal shape of the Earth (i.e. greater radius at the equator) and the centrifugal acceleration due to the Earth's rotation,

$$\frac{dg_L}{ds} = \frac{1}{R_e}\frac{dg_L}{\phi} \approx \frac{1}{R_{eq}}\frac{dg_L}{\phi} \approx 0.811 \sin(2\phi) \, \mathrm{mGal/km} \tag{1.14}$$

where ds is an infinitesimal step in the N-S direction, R_e is the radius of the Earth at latitude ϕ

(in radians), and R_{eq} is the equatorial radius (Telford et al., 1990).

Free-air/ Free-water Correction

To account for the effects of variations in elevation between observation points the free-air correction (on land) or free-water correction (underwater) subtracts the material between the observation point and a datum surface the data is being reduced to. The free-air correction is

$$\frac{dg_{FA}}{dR_e} = -\frac{2GM_e}{R_e^3} \approx -\frac{2}{R_{eq}} \approx -0.309\,\mathrm{mGal/m}, \tag{1.15}$$

with the free-water correction being

$$\frac{dg_{FW}}{dR_e} = -\left(\frac{dg_{FA}}{dR_e} - 4\pi\rho_w G\right) \approx -0.222\,\mathrm{mGal/m} \tag{1.16}$$

for a seawater density $\rho_w = 1.02$ gcm^{-3} for depth below sealevel (Telford et al., 1990).

Bouguer Correction

The Bouguer correction accounts for any additional mass between a given observation point and the chosen datum, other than air or water whose effect has already been removed with the free-air or free-water correction. Classically this is done by removing the gravitational acceleration of an infinite slab of thickness equal to the elevation difference between the given observation point and the datum,

$$\frac{dg_B}{dR_e} \approx \frac{dg_B}{dR_{eq}} = 2\pi\rho_{background}G = 0.01277\,\mathrm{mGal/m} \tag{1.17}$$

for a background rock density of $\rho_{background} = 2.67\,gcm^{-3}$ (Telford et al., 1990).

Next, a terrain correction would be performed to account for the topography/bathymetry around the data not being a planar slab, but variable. Alternatively, the Bouguer correction can be done with the same assumed background density, $\rho_{background}$, but rather than treating the material under the observation points as an infinite slab a digital elevation model (DEM) can be used to define its upper surface.

1.5 Voxel-based Inverse Modelling

Inverse modelling is a predictive method used by earth scientists to create a model of the subsurface that produces a geophysical signal closely resembling that which has been observed through surveying. Its name is derived from being the inverse of the forward modelling process, which calculates the geophysical signal produced from a physical property model. An example of a forward model is the TMI data calculated from a magnetic susceptibility model. Therefore, if given a magnetic field data set, inverting it will result in a magnetic susceptibility model of the subsurface, and through that a geologic interpretation.

1.5.1 Data misfit

Mathematically, an inversion method solves for a model, $\mathbf{m}$, whose forward signal, $F(\mathbf{m})$, closely matches the observed data, $\mathbf{d}$, by minimizing this measure

$$\sum_{i=1}^{N} \frac{(F(\mathbf{m})_i - d_i)^2}{\sigma_i^2} \tag{1.18}$$

known as the χ^2 measure of the data misfit (Lines and Treitel, 1984; Constable et al., 1987b). In any real data set there will be some noise that is generally assumed to be Gaussian. This assumption comes from random noise typically being Gaussian, but it also simplifies the mathematics as a datum's noise can be represented by its standard deviation, σ_i. Weighting the difference between the observed data, $\mathbf{d}$, and the predicted data, $\mathbf{F}(\mathbf{m})$, by the Gaussian noise, ε, with standard deviation σ allows for Eq. 1.18 to be reduced to the number of data points, N, when the predicted data matches the noiseless observed signal, $\mathbf{d_o}$, with

$$\begin{aligned} \sum_{i=1}^{N} \frac{(F(\mathbf{m})_i - d_i)^2}{\sigma^2} &= \sum_{i=1}^{N} \frac{(d_{oi} - (d_{oi} + \varepsilon_i))^2}{\sigma^2} \\ &= \sum_{i=1}^{N} \frac{\varepsilon_i^2}{\sigma^2} \\ &= \frac{\sigma^2 N}{\sigma^2} \\ &= N. \end{aligned} \tag{1.19}$$

using the definition of the standard deviation of the noise, ε, with a mean of zero,

$$\sigma^2 = \frac{1}{N}\sum_{i=1}^{N}\varepsilon_i^2. \tag{1.20}$$

It has become the norm to normalize the χ^2 measure by the number of data points in the observed data set to make the normalized χ^2 measure equal to 1 when the model has produced a forward signal that matches that of the observed data, excluding its noise,

$$\Phi_d = \frac{1}{N}\sum_{i=1}^{N}\frac{(F(\mathbf{m})_i - d_i)^2}{\sigma_i^2}. \tag{1.21}$$

which is known as the data misfit.

In vector notation the data misfit is written as

$$\Phi_d = \frac{1}{N}\left\|\mathbf{W}\left(\mathbf{F}(\mathbf{m}) - \mathbf{d}\right)\right\|^2 \tag{1.22}$$

with $\mathbf{W}$ being a matrix with diagonal elements equal to the observed data's standard deviation,

$$\mathbf{W} = diag(1/\sigma_1, 1/\sigma_2...., 1/\sigma_N). \tag{1.23}$$

1.5.2 Objective Function

The classic minimum-structure style of inverse modelling, by far the most common type of voxel-based inverse modelling, solves for a discrete distribution of a physical property in the Earth's subsurface (e.g. a density distribution to fit a gravitational acceleration data set, see Fig. 1.9a). The result is typically one or many blurred anomalous regions of the modelled physical property, indicating the location and size of the anomalous bodies being studied.

The voxel-based inverse problem is often under-determined, meaning there are usually more cells in the voxel mesh whose parameters are being solved for versus the number of observation data points. This is the case as many cells are needed to create an Earth model of sufficient resolution. The problem is also ill-posed, which results from several factors, including the presence of noise in the data, and the natural decay in model sensitivity with distance from the observation points. Hence, it is not enough to only fit the data, as there are infinitely many models that fit the modelling requirements. Additional measures of model structure must be put in place to provide unique and reliable solutions to the inverse problem (Constable et al., 1987b). An

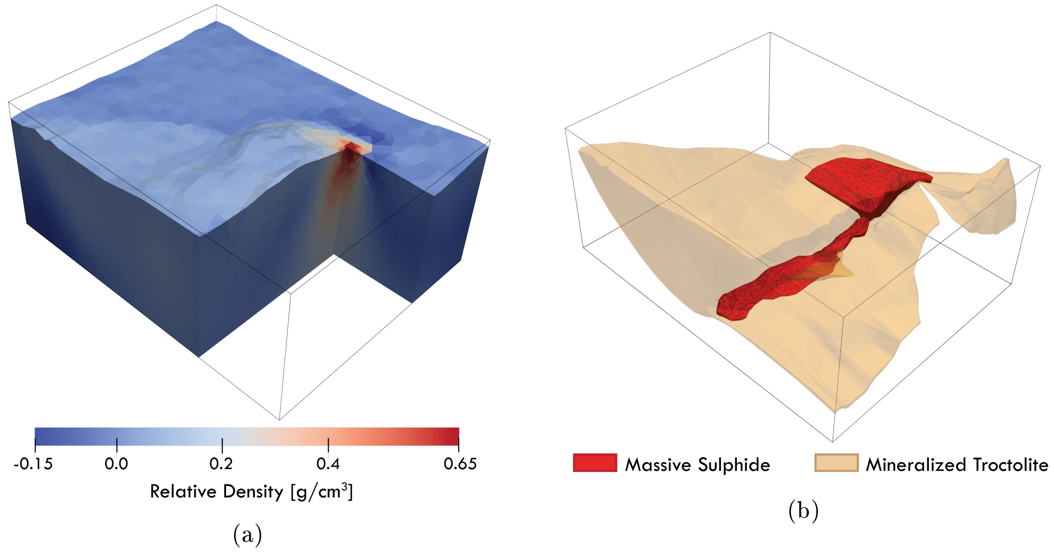

Figure 1.9: Two figures of the Voisey's Bay Eastern Deeps deposit, depicted as (a) a voxel-based inversion model and (b) a surface based geologic model.

objective function is therefore minimized to solve for a model that not only fits the data but is also geologically realistic:

$$\Phi = \Phi_d + \beta \Phi_m \tag{1.24}$$

with data misfit Φ_d, trade-off parameter β, and model measure

$$\Phi_m = \boldsymbol{v}_c^T \boldsymbol{W}_c \rho(\mathbf{m}) \tag{1.25}$$

in its generalized form. The general model measure term is composed of a product of the vector of the inverse model's cell volumes, $\boldsymbol{v}_c^T$, the weighting matrix, $\boldsymbol{W}_c$, and a vector holding the physical property information $\rho(\mathbf{m})$. The main purpose of the model measure term is to minimize the amount of unnecessary structure generated during the inversion modelling. Following Occam's Razor, the simplest model which provides an adequate fit to the observed data is most likely to be the most geologically accurate (Constable et al., 1987a).

Depending on the geophysical method there can be a difference in scale between the data misfit and the physical property values in the model measure function. To properly weight the components of the objective function a trade-off parameter is added, classically multiplied to the model measure. The trade-off parameter, also known as the Tikhonov parameter (Tikhonov and Arsenin, 1977), gets adjusted over the course of the inversion until the optimal value is found

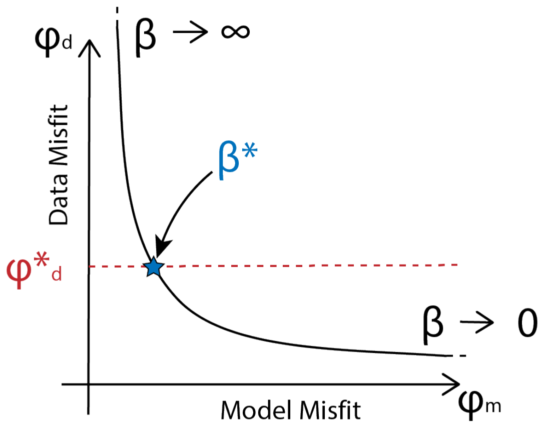

Figure 1.10: A trade-off curve, graphically showing the optimal value of the trade-off parameter, β^*, given a data misfit target value ϕ_d^*. Modified from Oldenburg and Pratt (2007).

that both minimizes the data misfit to its desired value and minimizes the model measure (Fig. 1.10).

Model Smoothing

The most fundamental part of the model measure component of the objective function is its smoothness function. The main aspects of the model smoothing norms is to promote smooth features in the final inversion model. Promoting smoothness helps to keep the inversion program from producing models composed of very small and unrealistic features with isolated very high or very low physical property values with respect to the background. Figure 1.11 demonstrates the effects of using a model smoothing during voxel inversion modelling. The smoothing is accomplished by adding a term to the objective function that measures the difference in physical property values between neighbouring voxels or spatial gradients in the mesh. As this term is minimized, along with the rest of the objective function, the differences in physical property values between neighbouring voxels are reduced.

The classically used smoothing function is the L2 norm (Constable et al., 1987a; Li and Oldenburg, 1996),

$$\rho\left(\boldsymbol{D}_f \mathbf{m}\right) = \|\boldsymbol{D}_f \mathbf{m}\|_2^2, \tag{1.26}$$

used to smooth the spatial distribution of physical properties in the voxel model by applying a general difference matrix, $\boldsymbol{D}_f$, to the vector of model parameters, $\mathbf{m}$. Note the effect of using an L2 norm during the inversion of Figure 1.11b, compared to the model using no smoothing in

Figure 1.11a.

As shown in Eq. 1.26 the L2 norm calculates the difference between neighbouring voxels, squares that difference and sums all the values together to get a single scalar value. Squaring the difference in physical property values in the mesh makes the L2 norm very sensitive to large differences in the model, making the inversion model composed of gradual changes in anomalous physical property values (Fig. 1.11b and 1.12b).

Another common smoothing measure is the L1 norm, which is similar to the L2 norm but does not square the difference between neighbouring voxels in the model,

$$\rho\left(\boldsymbol{D}_f \boldsymbol{m}\right) = \|\boldsymbol{D}_f \boldsymbol{m}\|_1. \tag{1.27}$$

By minimizing the absolute difference between physical property values in the model some smoothing is still enforced, but more discrete features may form compared to when the L2 norm is used (Fig. 1.11c and 1.12c).

Rather than merely calculating the difference between properties in adjacent voxels the total variation (TV) measure can be used, that calculates a difference value from all voxels within a neighbourhood of predefined radius. The TV measure improves on the L1 norm's ability to model more discrete features by removing any dependence on the structure of the mesh (Fig. 1.11d and 1.12d). The structural dependence of the L2 and L1 norms comes from the calculated differences being across the voxels' faces, so when inverting with a rectilinear mesh, for example, the L2 and L1 norms will smooth features along the three Cartesian directions, excluding any diagonals. By calculating the physical property differences within a neighbourhood defined by a radius, the TV measure no longer shows a bias for the directions of the voxels' faces' normals (Lelièvre and Farquharson, 2013). The TV measure is structured as

$$\rho\left(\boldsymbol{\omega}_t\right) = \left(\boldsymbol{\omega}_t^2 + \epsilon^2\right)^{\frac{p}{2}} \tag{1.28}$$

with

$$\boldsymbol{\omega}_t = \boldsymbol{Q}_x\left(\left(\boldsymbol{D}_x \boldsymbol{m}\right)^2\right) + \boldsymbol{Q}_y\left(\left(\boldsymbol{D}_y \boldsymbol{m}\right)^2\right) + \boldsymbol{Q}_z\left(\left(\boldsymbol{D}_z \boldsymbol{m}\right)^2\right), \tag{1.29}$$

containing three gradient operators, $\boldsymbol{D}_k$ $(k = x, y, z)$, for each Cartesian direction, and three

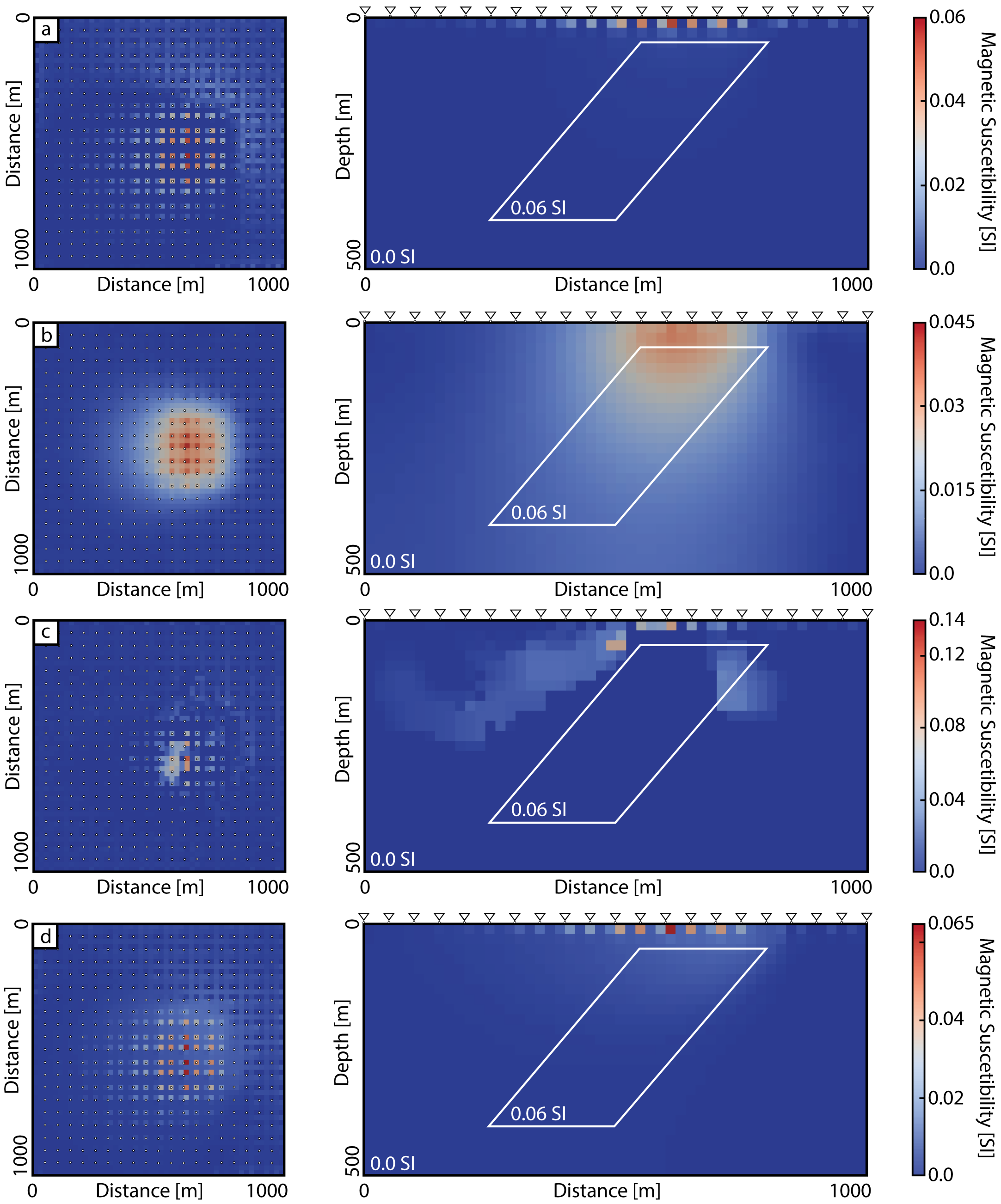

Figure 1.11: A comparison of the different smoothing model norms applied to a simple 3D prism synthetic model. a) The inversion result without any smoothing regularization, b) the result with L2 norm smoothing, c) the result with L1 norm smoothing, and d) the result with TV smoothing. The synthetic model is a 0.06 SI prism in a 0 SI half space with 2% Gaussian noise added to the data. The locations of the observation points are represented by white dots on the left-hand plan-view images of the model, and white triangles in the cross-sectional images. In the cross-sectional images on the right, which bisect the 3D model, a white wireframe model represents the outline of the 0.06 SI prism from the synthetic model. Positivity was enforced during the inversion, and no depth weightings were used.

matrices, $\boldsymbol{Q}_k$ ($k = x, y, z$), which interpolate the k-direction squared gradient values at the model cell centres. The parameter values used are typically $\epsilon = 10^{-9}$ and $p = 1.05$ (Fig. 1.11 and 1.12).

Sensitivity Weighting

Including a smooth model norm solves the problem of stopping the inversion program from fitting the data by just assigning anomalous physical property values right below the observation points, but the models will still show a preference of placing anomalous features near surface. This is because the voxels nearest the observation points have the greatest sensitivities, so changing their physical property values has the most effect. To preferentially weight cells in the model with low sensitivities (i.e. voxels further from the data points and typically deeper into the subsurface), a sensitivity weighting (Li and Oldenburg, 2000) can be used whose matrix, $\boldsymbol{W}_c$ (Eq. 1.25), is composed of elements,

$$w_j = \left(\sum_{i=1}^{N} \left| \frac{G_{ij}}{v_j} \right|^2 \right)^{\frac{1}{2}} \tag{1.30}$$

for the j^{th} model cell that has a volume of $\boldsymbol{v}_j$ and a sensitivity of $\boldsymbol{G}_{ij}$, with respect to the i^{th} observation point. $\mathbf{G}$ is the sensitivity matrix for the inverse problem

$$G_{ij} = \frac{F(\mathbf{m})_i}{m_j}. \tag{1.31}$$

This sensitivity weighting helps to prevent the inverse problem from creating a trivial solution of purely near-surface physical property anomalies (Fig. 1.12).

The sensitivity weighting is an updated version of the depth weighting (Li and Oldenburg, 1996, 1998a), whose matrix components are

$$w_j = |z_j - z_o|^{-\gamma/2}, \tag{1.32}$$

for a given voxel j whose centroid is at depth z_j and the average elevation of the observation points is z_o. The parameter γ is dependent on the geophysical data type, $\gamma = 2$ for gravity and $\gamma = 3$ for magnetics. More generally (without assuming the observation points lie on a plane at elevation z_o), the depth weighting can be converted to a distance weighting

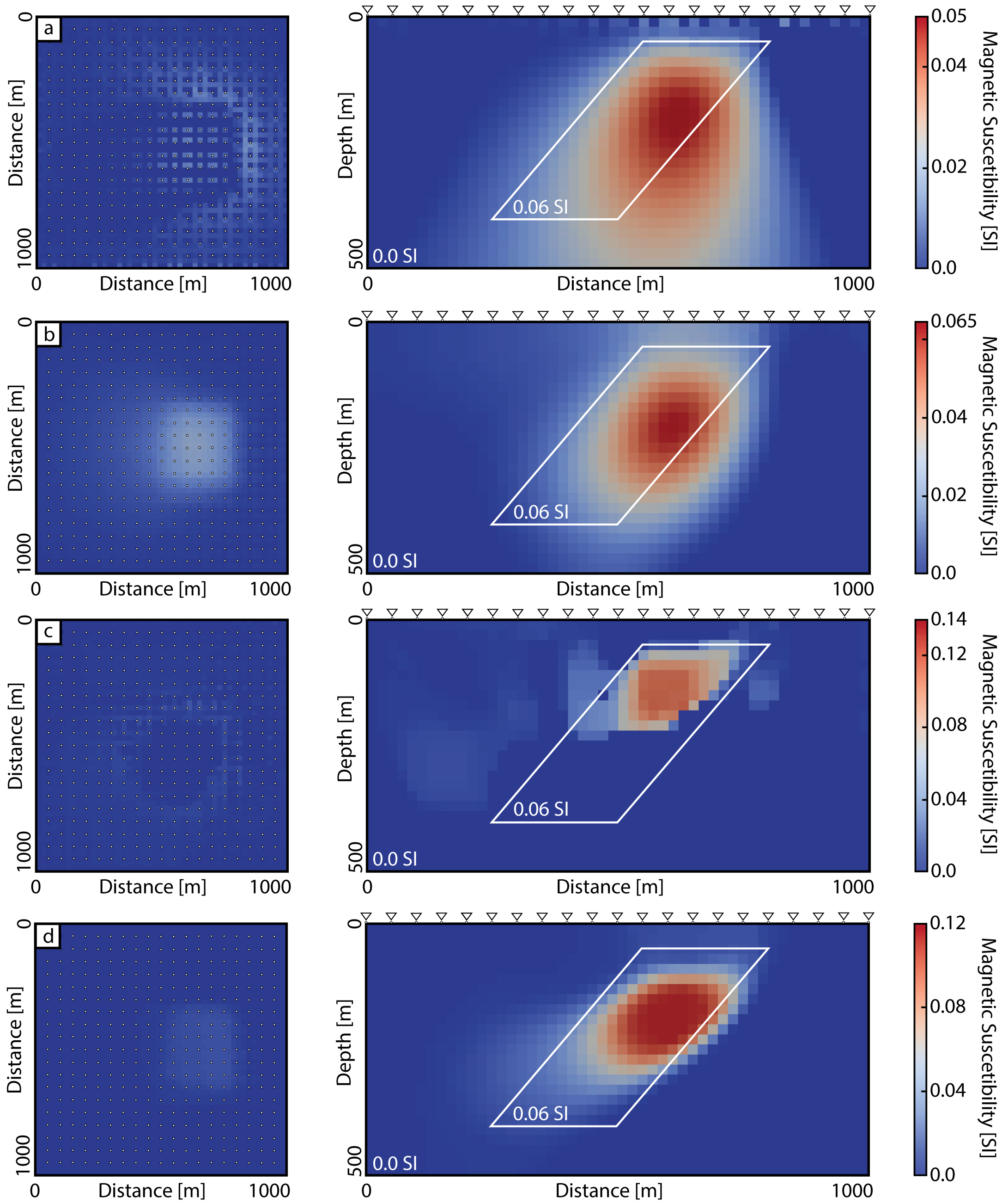

Figure 1.12: A demonstration of the effects of using a sensitivity weighting in addition to a) no smoothing, b) L2 norm smoothing, c) L1 norm smoothing, and d) TV smoothing. The synthetic model used in this example is the same as used in Fig. 1.11.

$$w_j = \left(\sum_{i=1}^{N} |r_i|^{-\gamma} \right)^{\frac{1}{2}}, \tag{1.33}$$

which is now a function of the Euclidean distance, r_i between the i^{th} observation point and the centroid of the j^{th} voxel.

Additional Objective Function Components

Given more *a priori* information on the subsurface any number of additional terms can be added to the objective function to promote the formation of certain features in the inversion model. However, with each objective function term added another trade-off parameter is also included to weight it, which must then be calculated during the inversion and therefore increases the complexity of the problem and the time needed to solve the inversion. No additional regularization terms other than those described in previous sections were used in the modelling described in this thesis.

1.5.3 Objective Function Minimization

Once the objective function has been defined for a given inverse problem a minimizing optimization procedure can be conducted to find the function's minimum. Fortunately for potential field voxel-based inversions, the forward solver is linearly proportional to the physical property, i.e. the predicted data, $\mathbf{d}_{pred}$, calculated from a model of parameters $\mathbf{m}$ which has been shown as

$$\mathbf{d}_{pred} = \mathbf{F}(\mathbf{m}) \tag{1.34}$$

can be, without approximation, represented as

$$\mathbf{d}_{pred} = \mathbf{G}\mathbf{m} \tag{1.35}$$

where $\mathbf{G}$ is the sensitivity matrix of the forward problem. For the simple case when just the data misfit and L2 norm of the model are considered for the objective function, along with keeping with model parameters unconstrained during the inversion, the objective function

$$
\begin{aligned}
\Phi &= \Phi_d + \beta\Phi_m \\
&= \left(\frac{1}{N}\,||\mathbf{W}\left(\mathbf{Gm}-\mathbf{d}\right)|\,|^2\right) + \beta||\boldsymbol{D}_f\boldsymbol{m}||^2
\end{aligned}
\tag{1.36}
$$

will minimize to (upon taking the derivative of the objective function and setting it to zero, Constable et al., 1987b)

$$
\boldsymbol{m} = \left[\beta\boldsymbol{D}_f^T\boldsymbol{D}_f + \left(\boldsymbol{WG}\right)^T\boldsymbol{WG}\right]^{-1}\left(\boldsymbol{WG}\right)^T\boldsymbol{Wd}. \tag{1.37}
$$

This scenario is of course idealized, and typically the inverse problem is not this simple, i.e. the physical property is constrained or a more complex smoothing norm is used in place of the L2 norm. In these cases an iterative minimization algorithm is implemented, which is commonly the Gauss-Newton method (Wright and Nocedal, 1999; Oldenburg and Pratt, 2007). The algorithm will begin with an initial model that is then used to calculate a quadratic hyper-surface quadratic based off the point's gradient. The algorithm then moves to the point at the minimum of the calculated quadratic and repeats this process until the global minimum is reached and a model is produced that adequately fits the observed data.

1.5.4 Advantages and Disadvantages of the Voxel-based Inversion Method

Voxel-based inversion methods have proven to be very robust by being able to produce useful Earth system physical property models with little prior information of the subsurface. This strength of the modelling method has out-weighed the fact that it produces inherently smooth and fuzzy model results, a consequence of the model regularization required to adequately minimize the non-uniqueness of the inverse problem. An example of this smoothness is shown in the Fig. 1.12d model, where its core is well resolved, but the anomaly's boundary is ill-defined.

Chapter 2 provides an example in implementing voxel-based inversion methods to modelling Earth systems, where it is used to model regional hydrothermal alteration below the seafloor.

Although the voxel inverse method produces inherently smooth Earth models, much research has been done into deriving more discrete geologic interfaces with this method. These areas of research include alternative regularization functionals (e.g Last and Kubik, 1983; Farquharson and Oldenburg, 1998; Portniaguine and Zhdanov, 1999), discrete-valued inversions (e.g Krahenbuhl and Li, 2009; Bijani et al., 2017), clustering (e.g Carter-McAuslan et al., 2015; Sun and Li, 2015), level set methods (Li et al., 2017; Zheglova and Farquharson, 2016; Zheglova et al., 2018), and shape-of-anomaly methods (René, 1986; Uieda and Barbosa, 2012); some post-inversion approaches can also achieve the desired model characteristics, e.g. Paasche (2016) and references therein. However, many of those inversion approaches involve increased numerical challenges and, ultimately, the underlying parameterization of the Earth is still inconsistent with the discrete geologists' interpretations.

An alternative to solving for the physical property values within each voxel of some discretized Earth model is to parameterize the problem by the positional coordinates of discrete, geometric shapes containing homogeneous physical property values (Oldenburg and Pratt, 2007). Chapter 3 presents a comprehensive study into the development of an inversion modelling method that has the ability to model complex targets as wireframe models. These discrete modelling methods, labelled Surface Geometry Inversion, are a more recent field of study mainly because the inverse problem is much more computationally expensive. As discussed in Section 1.5.3, a strength of the voxel-based inversion method is the linear relationship its forward solver has with the inversion parameter, i.e. the physical property values in each voxel. By instead inverting for the coordinates of geometric shapes the forward solver becomes non-linear, which in turn removes the guarantee that the inverse problem's solution space will alway be concave, i.e. there could exist local minima a decent based minimization method such as the Gauss-Newton method would get stuck in. Therefore global optimization methods are required to properly sample the solution space and find the inverse problem's global minimum. Fortunately, present day computers do offer the necessary processing power to implement Surface Geometry Inversions.

1.6 Thesis Outline

Chapter 1 of this thesis introduced the background material relevant to the research, such as the magnetic properties of the seafloor and the theory behind the the classically used voxel-based inverse modelling method. Chapter 2 demonstrates the capabilities of the voxel-based inversion method on a total magnetic field data set collected over a hydrothermally active region of the East Manus Basin. In this chapter the entire hydrothermal fluid upflow zone was modelled for the first time, addressing long held questions about the geometry of these hydrothermal systems that until now have been purely speculative. The third chapter introduces the SGI method, describes the details of its algorithm, and demonstrates its modelling capabilities on blocky synthetic models as well as a synthetic SMS deposit model. Chapter 4 demonstrates the capability of the SGI method on real data using both magnetic and gravity data collected over the active mound in the Trans-Atlantic Geotraverse hydrothermal field. The fifth and final chapter then concludes the thesis by summarizing the presented research.

Chapter 2

Mapping Hydrothermal Upflow Zones through Magnetic Inverse Modelling; East Manus Basin[1]

2.1 Introduction

Since their discovery on the East Pacific Rise in 1979 (Francheteau et al., 1979), high-temperature hydrothermal vents, and associated SMS deposits, have been identified as unique oases of chemosynthetic-based lifeforms and provide key information to the understanding of hydrosphere/lithosphere heat transfer at mid-ocean ridges and ore-forming processes on the seafloor (Hannington et al., 2011). Hydrothermal vents form as the end product of hydrothermal fluid convection systems driven by shallow magmatic heat sources (Jamieson et al., 2014b). Subseafloor fluid convection draws seawater into the crust, where it is progressively heated, and reacts with the host rock mineral assemblages before returning to the seafloor as a hot, reduced, metal- and sulfur-rich hydrothermal fluid. At the seafloor, the fluids mix with cold seawater, causing the precipitation of a portion (Jamieson et al., 2014a) of the dissolved components at focused venting sites along faults and/or fractures (Hannington et al., 2005b). Over time, the resultant accumulation of metal-rich sulfide minerals at vent sites can result in the formation of

[1] Galley, C.G., Jamieson, J.W., Lelièvre, P.G., Farquharson, C.G., Parianos, J.M. Magnetic imaging of subseafloor hydrothermal fluid circulation pathways. Sci. Adv. 6, eabc6844 (2020).

SMS deposits and continually provide sustenance for the organisms that inhabit vent sites.

Much of our understanding of hydrothermal systems is based on the study of known hydrothermal vents and associated deposits. However, the exposed vent sites represent only a small component of the overall hydrothermal system. To develop a holistic understanding of the size and sub-seafloor geometry of hydrothermal systems, previous studies have relied on numerical modelling (Fontaine and Wilcock, 2007; Hasenclever et al., 2014), seafloor heat flux measurements (Johnson et al., 2010), and studies of VMS deposits, which represent ancient analogues for modern hydrothermal systems that have been tectonically uplifted and are now exposed on land (Bosch et al., 2004). The numerical models provide the clearest depiction of a modern hydrothermal system, but are theoretical and rely heavily on assumptions and generalizations regarding the structural and thermal properties of the underlying crust and magmatic heat source. Seafloor heat flux models are limited to providing two-dimensional hydrothermal fluid flow information along the surface of the seafloor, and the ancient VMS systems have been tectonically deformed and altered making it difficult to reconstruct their original geometry.

Changes to the magnetic properties of oceanic crust caused by alteration of primary minerals along high-temperature hydrothermal fluid circulation pathways (see Section 1.2.2) can provide an alternative means to model subseafloor fluid flow geometries(Caratori Tontini et al., 2012). In hydrothermal systems hosted within mafic to felsic volcanic rocks, the alteration of titanomagnetite to titanomaghemite, as well as the dissolution of titanomagnetite and subsequent formation of pyrite, by high-temperature fluids produces zones of anomalously low magnetic susceptibility and magnetization (Szitkar et al., 2014a; Wang et al., 2020). Three-dimensional minimum-structure inverse modelling can be used to model the location and geometry of these anomalously low magnetism zones within the crust (Caratori Tontini et al., 2012; Kowalczyk, 2008). Minimum-structure inversion of a magnetic field data set constructs a three-dimensional distribution of effective magnetic susceptibility in the seafloor that closely reproduces the measured survey data, and that contains only sufficient features to reproduce those data (see Section 1.5). In this study, minimum-structure inverse modelling was applied to seafloor total magnetic field datasets centered on the Solwara 1 SMS deposit in the East Manus Basin, off the coast of Papua New Guinea.

The East Manus Basin is an actively opening back-arc basin in the Bismarck Sea (see Figure 2.1a). Back-arc rifting is associated with the active New Britain Trench that borders the southern extent of the basin (Taylor, 1979). To the north, the basin is bounded by the inactive Manus Trench. Within the basin, the crust is primarily composed of basaltic andesite, with intermittent concentrations of dacite, basalt and andesite (Yeats et al., 2014). Rifting is focused along the Eastern Manus Volcanic Zone, which comprises a series of relatively short, oblique, spreading ridges separated by large transform offsets, resulting in significant extensional faulting throughout the basin (Tregoning, 2002). Faulting is further enhanced by widespread volcanism associated with these tectonic features, resulting in a highly permeable linear fault and fracture network that is exploited by hydrothermal fluids. This results in the generation of numerous hydrothermal vent fields and SMS deposits along the length of the East Manus Basin, including PACMANUS (Binns and Scott, 1993) and DESMOS (Auzende and Urabe, 1996), and the Solwara 1 deposit (located on the Suzette volcanic edifice), located within Susu Knolls (Binns et al., 1997; Lipton, 2012). Within the region of Susu Knolls, all the known SMS deposits are located along the Tumai Ridge, a volcanically-active suture aligned orthogonal to the basin's north-west by south-east extension. The concentration of SMS deposits along the ridge suggests that a shallow magmatic heat source below the ridge drives hydrothermal circulation (Thal et al., 2016).

The variation in crustal magnetic properties in the East Manus Basin was modelled through the inversion of total magnetic field data collected during an autonomous underwater vehicle (AUV) survey in 2006 (Tivey et al., 2006) and two deep-tow surveys (2007 and 2016) that formed part of an SMS exploration program conducted by the Woods Hole Oceanographic Institute and Nautilus Minerals Inc. The deep-tow surveys covered the largest areas (5×9 km^2 and 44×24 km^2 at an average line spacing of 500 m and 200 m, respectively, and at an altitude of 40 m; Fig. 2.1b and c). The AUV data consists of two sets of grids focused directly over the Solwara 1 deposit and the North and South Su mounds (Susu Knolls; Fig. 2.1d) at an average line spacing of 50 m and an altitude of 20 m. Together, these three datasets allow the 3D magnetic structure of the crust to be modeled at both regional and deposit scale resolutions.

To numerically represent the seafloor in the East Manus Basin, a tetrahedral discretization of the sub-surface was used (Fig. 2.2). Designing a model of the study site using tetrahedra, rather than the classically used rectangular cuboids (Caratori Tontini et al., 2012), allowed the model to accurately fit the variable seafloor topography in this region. Additionally, using a tetrahedral discretization allows regions of interest, such as below the measured data, to be modelled to a higher resolution than the rest of the model, optimizing computational efficiency

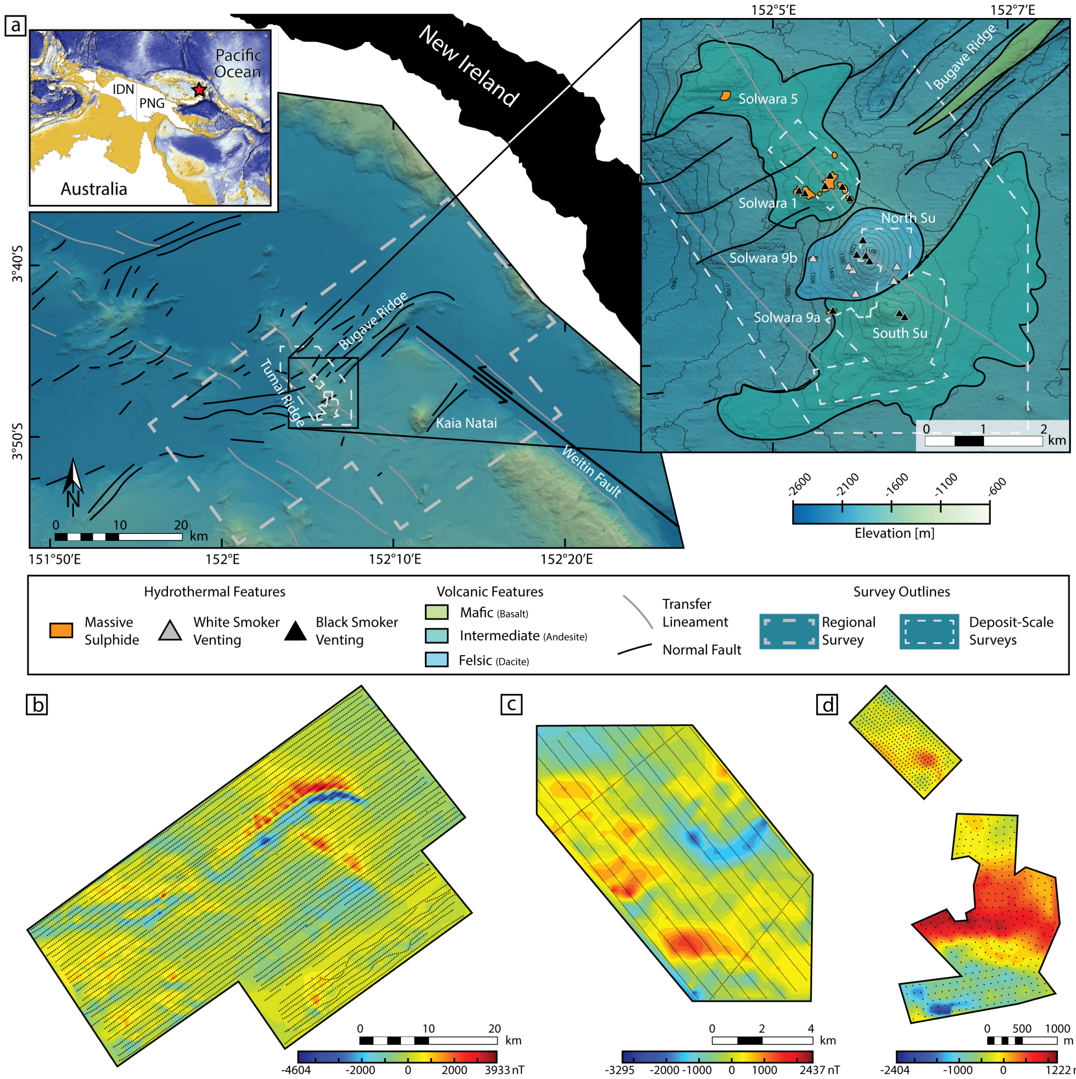

Figure 2.1: Map of the East Manus Basin in the region of the Tumai and Bugave Ridges, along with this study's total magnetic field anomaly maps. a) A 35 m resolution bathymetric map of the East Manus Basin, centered about the Tumai Ridge and Bugave Ridge intersection. The inset map shows the major geological features near Susu Knolls (Dyriw and Parianos, 2018) and the locations of the known active and inactive hydrothermal vent sites along the Tumai Ridge (Tivey et al., 2006; Seewald et al., 2019), with 50 m bathymetric contour lines. Dashed grey and white lines represent the extents of the magnetic surveys. b)-d) total magnetic field anomaly maps for the regional survey, and both deposit-scale surveys, respectively. The black dots mark the positions of the measurement locations, and fault and lineament feature as from Dyriw et al. (2021).

and model accuracy. Scalar magnetic susceptibility was inverted for assuming the total magnetization direction was parallel or anti-parallel to the geomagnetic inducing field. The magnetic property modelled is then an "effective" susceptibility that combines both induced and remanent magnetization (Lelièvre and Oldenburg, 2009). This assumes that all remanent magnetization is parallel or anti-parallel to the inducing field. Based on previous work in the East Manus Basin, this is considered a reasonable assumption within our study region (Martinez and Taylor, 1996), where there is minimal deformation of the seafloor crust that would change the orientation of any remanent magnetization with respect to the geomagnetic inducing field vector.

To date, magnetic modelling of the seafloor has been limited to the shallow subseafloor at hydrothermal discharge sites (Caratori Tontini et al., 2012; Kowalczyk, 2008; Szitkar et al., 2014a; Szitkar and Dyment, 2015). This study significantly improves upon the scale of these previous magnetic models by, for the first time, imaging the entire structure of a high-temperature convection column, including the identification of the top of the underlying magma chamber. The inversion modelling can identify such deep crustal features because of the large area that the regional deep-tow data set covers (44×24 km^2). Magnetic features located kilometers below the seafloor will impart very weak but very broad magnetic signatures due to the large distance between the feature and the measurement location. This contrasts with near surface magnetic features that would produce very strong but narrow magnetic field signatures when measured at a similar distance above the seafloor. Therefore, having a data set that samples the magnetic signatures of deep crustal features over a large area allows the broad, low amplitude signals to be adequately measured, and therefore modelled. This of course assumes that the magnetic features are large enough to produce a broad, low amplitude signal that can be measured above noise levels.

2.2 Methods

The inversions were performed with a minimum-structure modelling program developed at Memorial University (Lelièvre and Farquharson, 2013). This program uses a tetrahedral discretization of the subsurface to recover a distribution of effective magnetic susceptibility that, when in the presence of the Earth's field, generates an induced magnetic field that closely matches observed magnetic field measurements. In this study the total variation model measure was used,

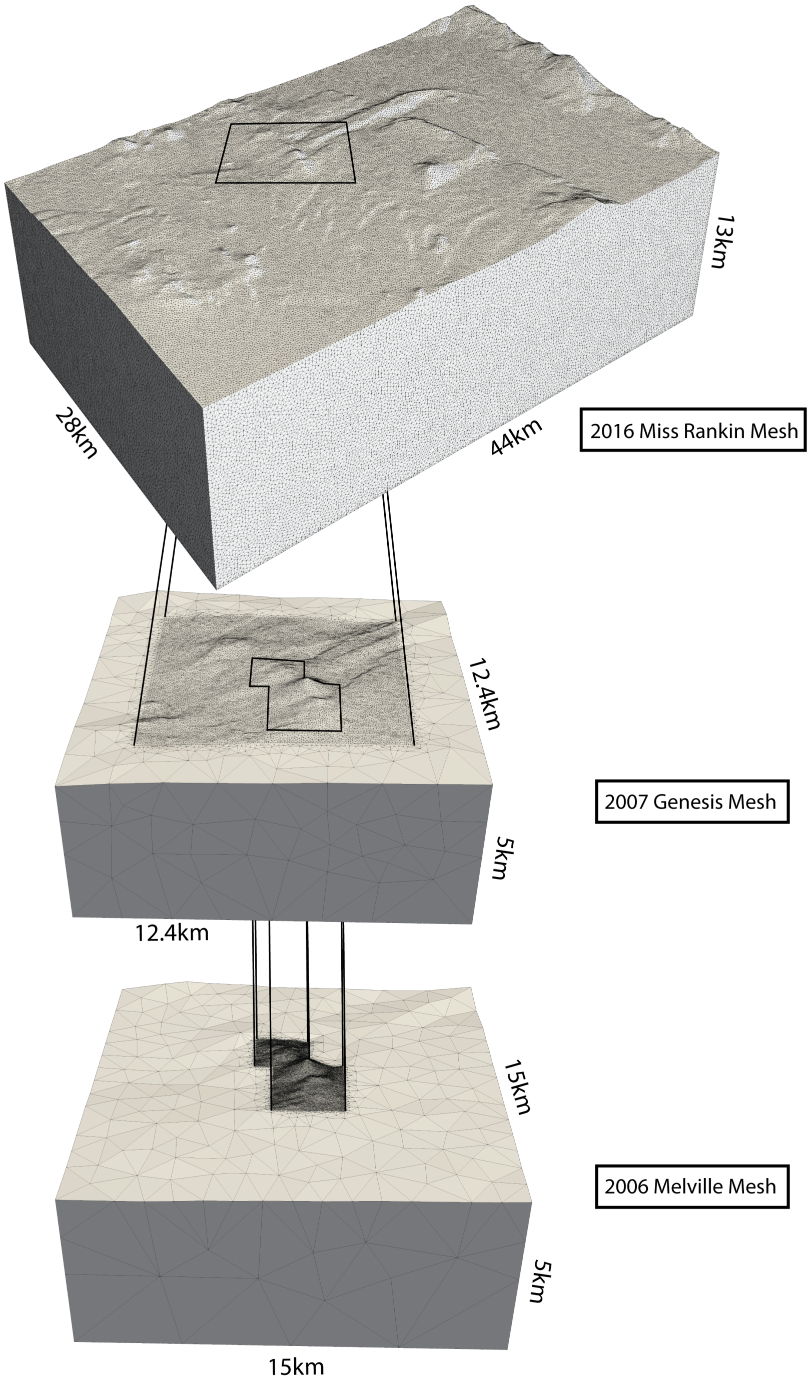

Figure 2.2: The three meshes used for our inverse modelling, shown in relation to each other. At the top is the mesh for the regional inversion model, from the 2016 M/V Miss Rankin cruise, with the two deposit-scale meshes below it in descending order of survey size, from the 2007 M/V Genesis then the 2006 R/V Melville cruises. All meshes are viewed from the south.

along with a sensitivity weighting (see Section 1.5 for more details).

To initiate the inversion, a homogeneous 0.2 SI effective magnetic susceptibility was used as a starting model. No reference models were used during the inversion, as the subseafloor geology in the East Manus Basin is fairly unknown, so we did not want to include any potentially incorrect bias into the modelling. To constrain the inversion, positivity was enforced with respect to the effective magnetic susceptibility. This was done to generate more geologically representative models, as models that we created without positivity were almost entirely positive, save for very small-scale model features indicative of data over-fitting. It is possible to have negative effective susceptibility, which would be the case where the remanent magnetization component of the effective susceptibility outweighs the induced field component, while being anti-parallel to the Earth's present field. If this were the case in this study's models then there would be larger regions of negative effective susceptibility, spanning zones of homogeneous rock and/or alteration types, which were not present.

Each inversion was performed on a separate model mesh, whose average cell size in the volumes of interest was dependent on the density of the respective data set. It was first ensured that the density of triangular facets in the bathymetry surface, as generated with the program *Triangle* (Shewchuk, 2003), was greater or equal to the density of observation points. Once a sufficiently dense surface mesh was made to fit the bathymetry of the region, the program *TetGen* (Si, 2015) was implemented to discretize the full extent of the volume of interest with tetrahedra. The volume of interest for each model was designed such that its boundary outlined the extent of each survey's data points, plus at least a 2 km thick padding cell region surrounding the volume of interest (Fig. 2.2). These padding cells limit the edge effects resulting from approximating the seafloor as a smaller, discretely bounded block.

The Miss Rankin inversion was performed on a mesh of 1,792,073 cells and 7,927 data observation points. The survey line spacing from the M/V Miss Rankin cruise was approximately 500 m, and the data were decimated to have a 200 m spacing along survey lines. The Genesis mesh contained 1,367,241 cells and 2,368 data points were used, with an approximate line spacing of 400 m, and an along-line spacing of 100 m. Lastly, the Melville inversion used a mesh of 1,345,270 cells and 717 data points. The AUV data over Susu Knolls was collected over four dives, with one dive providing a fourteen-line grid over the Solwara 1 deposit and six variably oriented and spaced grids over North Su and South Su. For the inversion, the data over the Solwara 1 deposit was decimated to 50 m along-line spacing, approximately equal to the average line spacing, and the North Su and South Su survey was decimated to 100 m point spacing (along-line and line spacing). See Fig. 2.1 for each survey's magnetic field measurements (with the normalized residuals displayed in Fig. 2.6).

The three magnetic surveys took place over a span of ten years, so three different inducing magnetic field vectors had to be used during the inversions. At the time of the 2006 RV Melville cruise at Solwara 1 the Earth's magnetic field had a strength, inclination, and declination of 39,083 nT, I = -21.714°, D = 6.535°. The 2007 Genesis magnetic anomaly was calculated with a magnetic field vector of (39,102 nT, I = -21.683^o, D = 6.61^o), and the 2016 Miss Rankin vector was (39,037 nT, I = -21.816^o, D = 6.201^o). All field vectors were calculated using the Enhanced Magnetic Model (EMM2017).

All inversions were performed on a 24 core 2.20 GHz Intel Xeon E5-2650 processor, yielding run times of 4,746, 1,368, and 564.4 CPU hours for the Miss Rankin, Genesis, and Melville models, respectively.

2.3 Regional Modelling

The most extensive model spans the length of the Tumai and Bugave Ridges, including the Kaia Natai volcano and the northern extent of the Weitin Fault (see Fig. 2.3 for the model and Fig. 2.1 for its bathymetry). The plan view of the 3D magnetic model highlights the regions of lowered effective magnetic susceptibility that correspond with Susu Knolls, Solwara 5, and Kaia Natai hydrothermal vent fields. Additionally, the basaltic Bugave Ridge stands out as a magnetic high, because the relatively younger mafic to intermediate volcanics that makes up the ridge will contain more un-oxidized titanomagnetite than the surrounding older volcanic rock (see Section 1.2.2). In cross-sections A and B of Figure 2.3, the sub-seafloor zones of low effective magnetic susceptibility were interpreted to represent pathways of hydrothermal fluid upflow below Solwara 5, Susu Knolls, and an unnamed site of sediment hosted base and precious metal anomalies. These upflow zones appear to originate from a common heat source that is approximately 3 km to the west of Solwara 5, at a depth of 3 km below the seafloor (5 km below sea level, see Fig. 2.3).

To the west of Susu Knolls lies a region with 40 to 60 m of sediment cover known as West

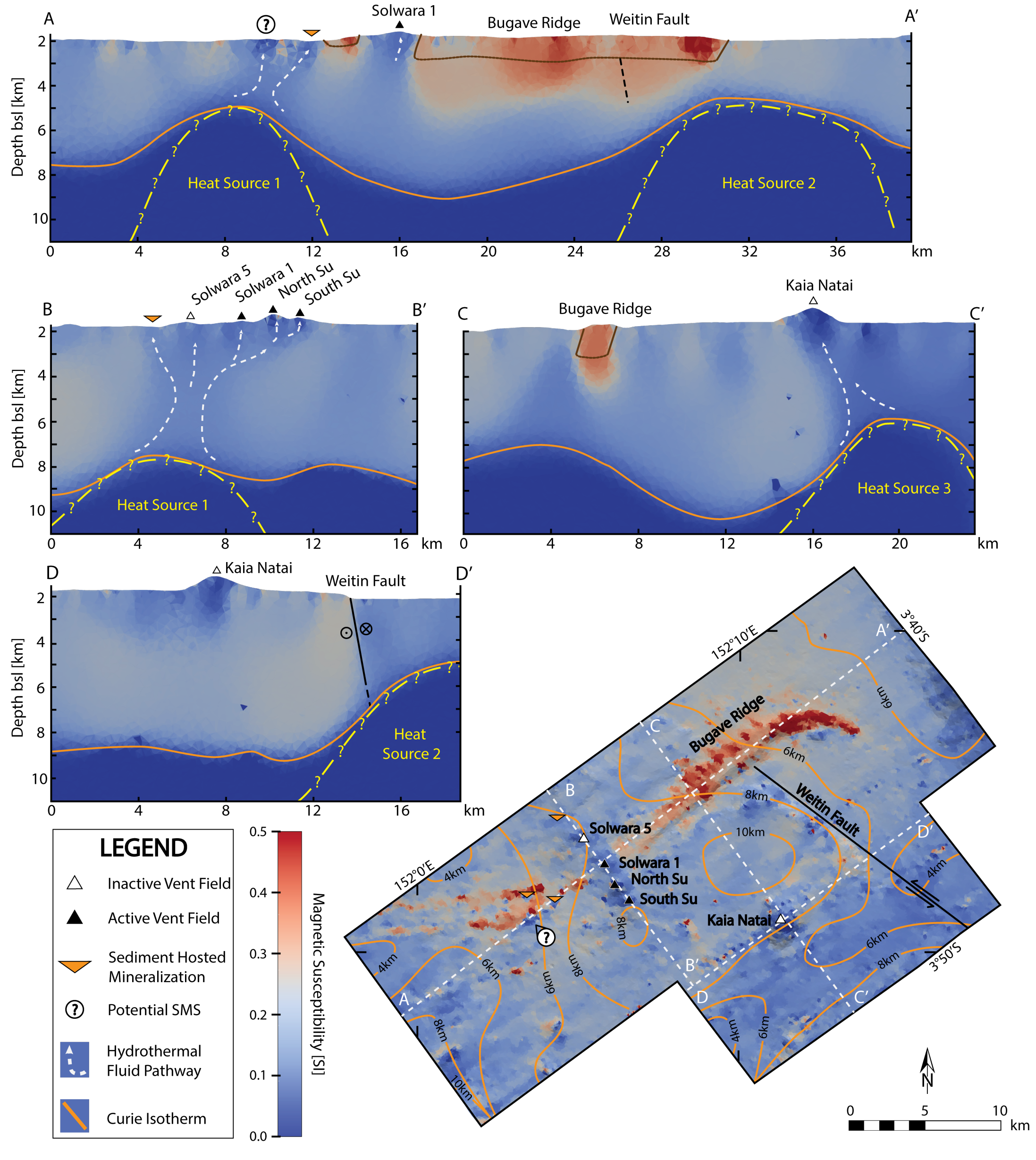

Figure 2.3: Map and cross sections of effective magnetic susceptibility from the regional 3D magnetic inversion model. A-A′ displays two prominent magnetic lows at 2 km below the seafloor, which was interpreted to be magma chambers. The southwest magma chamber is the primary heat source driving hydrothermal circulation at Solwara 5 and Susu Knolls. B-B′ shows sub-seafloor high-temperature fluid pathways that feed the venting sites along the Tumai Ridge. C-C′ & D-D′ are two cross-sections that pass through the hydrothermally active Kaia Natai volcano. The depth to the Curie isotherm is included on the plan view image as a contour map with orange lines, mapping the geometry of the underlying magmatic bodies.

Su (Yeats et al., 2014), with shallowly intruded mafic sills marked by areas of high effective magnetic susceptibility (seen near the two sites of sediment hosted metal anomalies and the one possible SMS site labelled in Fig. 2.3). Sites of sub-surface sulfide mineralization identified in this region through the gravity coring sediment collection method are underlain by a zone of low magnetization that are also interpreted to represent hydrothermal fluid pathways connected to the same heat source driving the Tumai Ridge's hydrothermal activity (Fig. 2.3).

The heat sources identified from the regional model are labelled as heat sources 1-3. Heat source 1 lies approximately 3 km below the seafloor to the south-west of Susu Knolls, and is connected to venting sites along the Tumai Ridge and the sediment hosted sites to the west by magnetically-imaged demagnetized alteration pipes (Fig. 2.3 cross-sections A and B). Heat source 2 is the top of an interpreted magma chamber that spans the length of the Weitin Fault segment. Heat source 3 is approximately perpendicular to the Weitin Fault, lying 2-4 km below the seafloor to the south of Kaia Natai.

The Kaia Natai volcano, located south-east of Susu Knolls and independent of the Tumai and Bugave Ridges, hosts a low temperature hydrothermal vent field (Auzende et al., 2000). The presence of hydrothermal alteration at this site is supported by a low effective magnetic susceptibility region that extends approximately 2 km below the volcano (Fig. 2.3).

2.4 Deposit-scale Modelling

The two inversion models centered over the Solwara 1 deposit were derived from magnetic surveys collected over a smaller area but at greater resolution than the regional survey, and therefore are able to better resolve near surface magnetic features at the expense of deeper features. Where our regional model could define alteration zones associated with hydrothermal fluid channels from heat source to seafloor, the more detailed models better illustrate the individual fluid pathways near the seafloor after they diverged from a common upflow zone (Fig. 2.4). The models indicate a more intense magnetic signature below North and South Su, compared to Solwara 5, possibly indicating greater degrees of titanomagnetite destruction (Fig. 2.4a). At Solwara 1, the area of mineralization is resolved at even greater detail by inverting magnetic data collected near the seafloor by an AUV (Fig. 2.4b). Here, the pronounced magnetic low is due to the massive sulfide layer and underlying stockwork system that have lower effective magnetic susceptibilities than the surrounding altered host rock (Zhao et al., 1998). Additional locations of further magnetic reduction are visible at sites of present (Seewald et al., 2019) and past (Thal et al., 2016) hydrothermal venting, particularly around the top of North Su and the rim of South Su where known high temperature venting occurs, as well as between the two volcanoes where lower temperature white smoker venting has been observed (Figs. 2.1 and 2.4b).

2.5 Discussion

High-temperature fluid pathways associated with sub-seafloor hydrothermal alteration, imaged using the magnetic inverse modelling, correlate with the known locations of both active and inactive hydrothermal vent sites or other areas with known surface mineralization associated with hydrothermal venting. Fluid pathways can be traced to inferred heat sources 2-4 km below the seafloor. A further two sites of possible mineralization above altered upflow zones have been identified, illustrating the potential of magnetic inverse modelling as an effective exploration tool for both active and inactive sites of hydrothermal mineralization (Figs. 2.3 and 2.4a). These sites are in close proximity to other hydrothermal features yet have their own separate zones of demagnetization. In the case of the interpreted SMS anomaly in Fig. 2.4a, a shallow 3D seismic survey collected by Nautilus Minerals identified that location as a site of possible mineralization, further supporting this interpretation.

Along the base of the regional model lies a surface of zero effective magnetic susceptibility, representing the Curie isotherm, beyond which the partially crystallized rock is too hot to maintain any magnetization (Fig. 2.3). The crust's primary magnetic minerals, magnetite and titanomagnetite, have respective Curie temperatures of 530-585 °C (Wang and der Voo, 2004) and 110-170 °C (Bina and Prévot, 1989). As shown in Fig. 1.5b, the amount of Ti in a titanomagnetite has a strong effect on the mineral's Curie temperature. The regional model indicates three zones with a prominent upwelling of the Curie isotherm, observed to the south-west of Susu Knolls (labelled heat source 1), along the Weitin Fault (heat source 2), and south of Kaia Natai (heat source 3; Fig. 2.3). These zones of upwelling are interpreted to indicate the presence of shallow magma chambers that warp the isotherms and create steep thermal gradients above the chambers (Hasenclever et al., 2014; Piercey, 2011; Cathles, 2011; Theissen-Krah et al., 2016). The melt underlying the Tumai Ridge has an estimated temperature of $\sim$ 1,010 °C (Siegburg

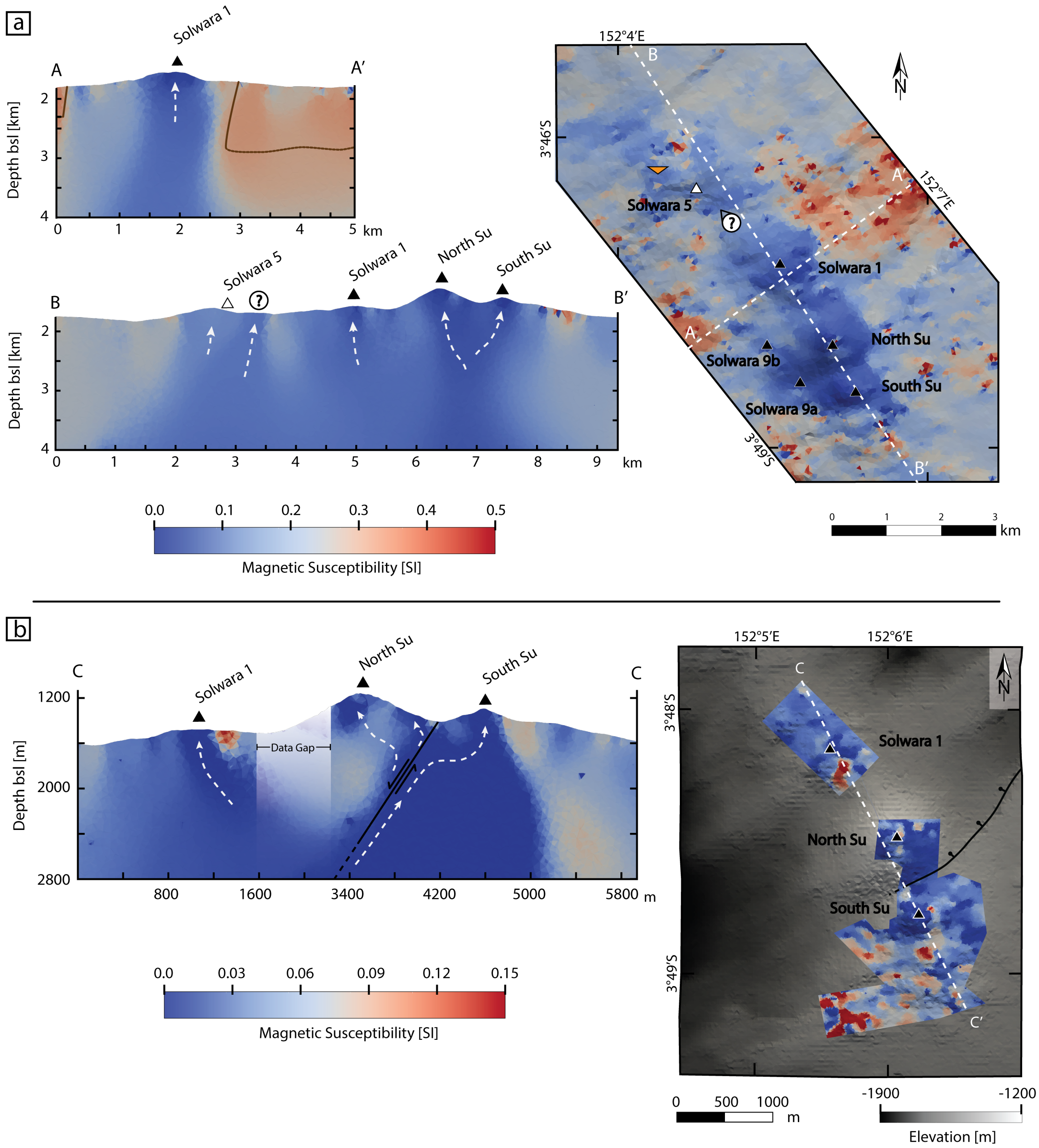

Figure 2.4: Map views and cross sections of the two deposit-scale 3D magnetic models. a) The 2007 data inversion model, with cross-sections: A-A′ shows a vertical alteration column associated with ascending hydrothermal fluids beneath Solwara 1; B-B′ shows variation in near-surface effective magnetic susceptibility along the Tumai Ridge, with focused low susceptibility zones located at Solwara 5 and the three venting sites of Susu Knolls. An additional site of possible mineralization, southeast of Solwara 5, is interpreted from its magnetic characteristics which match those of nearby known hydrothermal venting sites. b) 2006 AUV data inversion model, with a single cross-section C-C′ showing partitioning of the fluid pathways within Susu Knolls leading to known vent sites. All symbols are the same as indicated in Fig. 2.3 legend.

et al., 2018), which is much higher than the oceanic crust's Curie point, but due to the high thermal gradient above magma chambers (Hasenclever et al., 2014), the depth to the melt lens will likely be near to the Curie isotherm. Therefore, the peaks of the warped Curie isotherm are interpreted to represent the tops of the magma chambers.

Before this study, magmatic bodies had not been modelled through magnetic inversion because of the lack of seafloor magnetic surveying performed and modelled at this scale. Traditionally, the tops of magma chambers have been imaged through seismic and magnetotelluric methods, and typically occur 2-3.5 km below the seafloor along spreading ridges (Purdy et al., 1992). Specific to the Susu Knolls volcanic system, melt inclusion analyses have indicated the magma chamber to be 1-5 km below North Su (Siegburg et al., 2018), which, along with the typical depths of 2-3.5 km from other geophysical methods, is consistent with our interpretation.

The boundary between pillow basalts and underlying sheeted dykes (layer 2A/2B boundary White et al. 2014) in oceanic crust typically occurs 400-1,000 m below the seafloor (Jacobs et al., 2007). Below the Tumai ridge this depth range aligns with a branching of the near vertical hydrothermal alteration column, marking the zone where the fluid pathways separate towards the individual hydrothermal vent sites (Fig. 2.3 cross-section B-B′). This suggests that rising hydrothermal fluids closely follow the higher-permeability regime aligned with semi-vertical dykes within the sheeted dyke zone. Once the rising fluids cross the layer 2A/2B boundary and enter the layer of crust dominated by more permeable sheet flows, hyaloclastite, and pillow basalts, the fluid flow appears to gains a greater horizontal component and branching potential (Anderson et al., 1985; Nehlig and Juteau, 1988). This is counter-intuitive, as fluid pathways entering a higher permeability medium will generally thin as the fluids flow with a greater vertical velocity. This model feature may therefore be indicative of some sort of semi-conformable boundary that could have formed during the lifecycle of the hydrothermal upflowzone (Galley, 1993). Additionally, normal faults in the shallow subseafloor on either side of the Bugave Ridge (see inset from Figure 2.1a, and Figure 2.4b) provide additional permeability to focus the hydrothermal fluids to their present active and inactive vent sites.

Below the Tumai ridge and associated hydrothermal venting sites, the top of the zero effective magnetic susceptibility volume, representing the upper extent of the magma chamber, can be considered a lower boundary to the hydrothermal convection cells which feed the surface vent sites, as the melt will be an impermeable thermal boundary to hydrothermal fluids (Moss et al.,

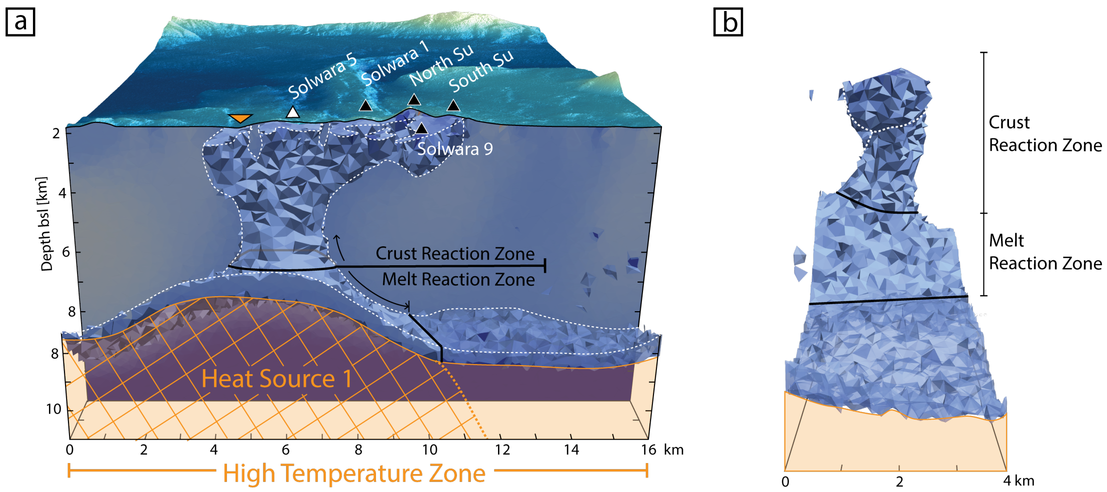

Figure 2.5: A 3D model of the high-temperature hydrothermal upflow column below the Tumai Ridge. The shown cross section is B-B′ from Fig. 2.3, with the alteration column visualized with a 0.12 SI threshold of the regional model's effective magnetic susceptibility. a) View of the column facing north-east; b) view of the same column facing north-west. All surface hydrothermal feature symbols and the colour scale follow the legend in Fig. 2.3.

2001). Laterally, the width of the column of high-temperature fluids rising from the magma chambers can be approximated by the regions of anomalously low effective magnetic susceptibility defined by a model-derived upper threshold of 0.12 SI, in contrast to the background region's susceptibility of approximately 0.2 SI (Fig. 2.5). Below this threshold, vertical connectivity along the high-temperature upflow column is no longer present. For an upper threshold, the convection column is no longer confidently distinguishable from the surrounding crust above a threshold of 0.14 SI. To study the minimum volume of crust that is exposed to high-temperature hydrothermal fluid convection, and because minimum-structure inverse modelling tends to produce blurred results, a lower approximate effective magnetic susceptibility value of 0.12 SI was chosen.

The resulting 3D model of the convection column beneath the Tumai Ridge demonstrates the connectivity and geometry of the fluid pathways with respect to their heat source and the overlying hydrothermal vent sites. Two prominent zones can be distinguished from this model: the first being the Crust Reaction Zone (CRZ) where the high-temperature hydrothermal fluids are interacting solely with the oceanic crust; and the second being the Melt Reaction Zone (MRZ) where, in addition to reacting with the crust, the hydrothermal fluids also circulate near the magma chamber and are exposed to magmatic fluids devolatilizing from the rapidly cooling and fracturing chamber margins, changing the chemistry of the fluids (Yang and Scott, 1996; Moss et al., 2001; Beaudoin and Scott, 2009; Seewald et al., 2019). Most notably, this supercritical interaction with magmatic volatiles has been shown to enrich the fluids with precious (Au and

Ag) and base metals (Cu, Zn, and Fe; Yang and Scott 1996), leading to greater likelihood of higher grade SMS deposits forming at the overlying hydrothermal vent fields. Using the regional inversion model, the volumes of the CRZ and MRZ can be measured and used to approximate the volume of rock that the high-temperature hydrothermal fluid interacts with. Under the Tumai Ridge the CRZ was found to encompass approximately 22.5 +/- 3.4 km^3 and the MRZ 27.5 +/- 3.3 km^3, with the uncertainty being derived from a +/- 0.02 SI variation from the chosen 0.12 SI threshold.

As with any voxel inversion model, there is the inherent blurriness as a result of the smoothness regularization. The smoothness of the model has the tendency to resolve singular model anomalies that might correspond to multiple real anomalies in the subsurface (see Fig. 3.7a), but this smoothing does not create multiple model features where there might be a singular anomaly. As such, the branching of the hydrothermal fluid pathways may occur somewhat below where they appear in the model (Fig. 2.5), but likely not higher, and the branching observed in the regional model would not be an artifact.

Analysing the normalized data residual plots of Fig. 2.6, two prominent features are present at the peaks of the North and South Su mounds (Fig. 2.6a). These most likely result from an error introduced by the resolution of the bathymetry used to construct the mesh for that inversion. The available 35 m resolution led to the linear interpolation of features between those bathymetric points, and at locations like the peaks of the volcanoes linearly interpolating between points spaced 35 m apart can lead to a noticeable difference from the true seafloor bathymetry. The amplitude of noise in the three magnetic data sets were unknown, so a percent noise of 1 % was assumed for the inverted data, and then a normalized target data misfit of 64 was used to generate inversion models that did not produce artifacts indicative of data overfitting. Artifacts such as strong, near-surface high and low magnetic susceptibility anomalies located below the observation points. The target misfit was iteratively increased during the modelling process, through multiple inversions, until a model was produced that no longer contained these artifacts. This target misfit indicates that the noise, if assumed to be Gaussian, is approximately 8 %.

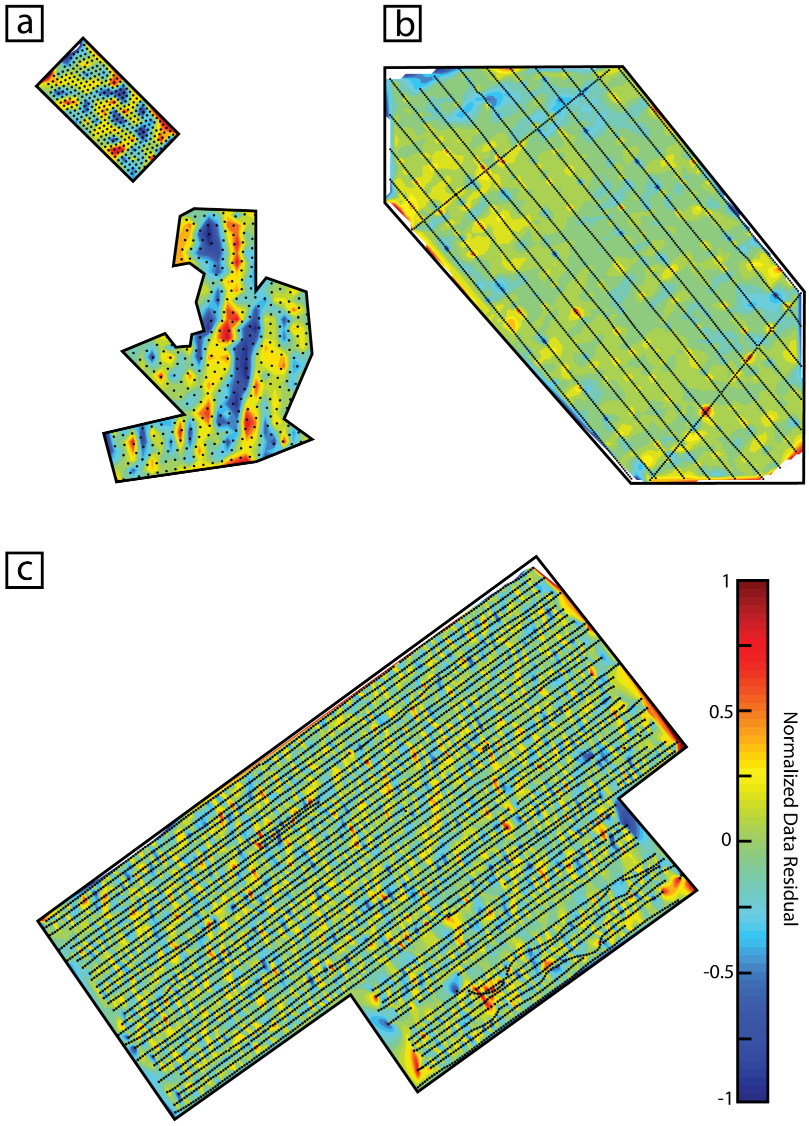

Figure 2.6: The normalized data residuals for the three inverted data sets. a) the normalized data residuals for the inverted 2006 AUV magnetic data set, b) for the inverted 2007 deep-tow magnetic data set, and c) for the inverted 2016 deep-tow magnetic data set.

2.6 Conclusion

To conclude, regional 3D inverse modelling of near-seafloor magnetic field data was used to image high-temperature hydrothermal fluid pathways from magmatic heat source and MRZ, through the CRZ, to seafloor fluid vent sites and associated seafloor massive sulfide deposits. Knowing the 3D geometry of these systems increases our understanding of the scale and connectivity of hydrothermal upflow zones, allowing us to better identify the location of undiscovered vent fields, the volume of crust that the fluids interact with, and the spatial relationship between hydrothermal discharge sites that support unique biological communities. The limitation of this method is that it relies on imaging the alteration associated with high-temperature fluid-rock interactions, and thus can only image high-temperature hydrothermal upflow and discharge at the seafloor, but cannot image fluid pathways associated with colder hydrothermal recharge.

Chapter 3

Surface Geometry Inverse Modelling[1]

3.1 Introduction

Alternatively to the voxel-based inverse modelling method, geophysical data can be inverted with a surface geometry inversion (SGI) method. This inverse method is distinct from voxel-based inverse modelling because it does not restrict itself to using a static mesh. SGI instead has the structure of its mesh parameterized into the inversion, allowing the geometry of the facets to change to fit the shape of anomalous regions in the subsurface. This would then lead to geophysical models solved for with the SGI method to be parameterized the same as classic geologic models (see Fig. 1.9b), leading to a much simpler integration of modelling results between the two fields of Earth science.

Using inversion to estimate the geometry and location of contact surfaces is certainly not new in the field. Many early geophysical inverse problems involved small computational problems that fit simple shapes to measured data, sometimes referred to as discrete body inversion: see examples in Oldenburg and Pratt (2007). These simple shapes include sheets, rods and ellipsoids, which can be represented with very few parameters that control their position, orientation and size. An underlying assumption often made is that of homogeneous physical properties inside and outside the object. Clearly, such a specific parameterization is not generally applicable. However, such

[1]Galley, C.G., Lelièvre, P.G., & Farquharson, C.G. (2020). Geophysical inversion for 3D contact surface geometry. Geophysics, 85(6), 1-76.

methods can provide acceptable results when the targets are close to the assumed shapes or, more generally, can be represented by some reduced set of parameters (e.g. Song et al., 2011; Tridon et al., 2016). In other situations, they can still provide fast, helpful, first-pass analyses (e.g McMillan et al., 2014; Tlas and Asfahani, 2015; Foss et al., 2016; Titus et al., 2017; Giannakis et al., 2019).

Tanner (1967) developed a 2D inversion approach where a lithological contact was built directly into the model parameterization. The Earth was represented as a set of horizontally adjacent vertical rectangular prisms extending below the topography surface; the bottom of these prisms represented a single sub-horizontal (non-overturned) contact between two units. Many others have extended this basic approach to allow for more complicated scenarios, such as the 3D case in Hidalgo-Gato and Barbosa (2019). Fullagar et al. (2000) generalized the approach in 3D by allowing for multiple layered rock units: their vertical rectangular prisms have internal contacts that divide each prism into homogeneous layers. The physical properties of each layer can remain fixed while the inversion controls the vertical position of the contacts within each layer. The approach requires that stacked layers are appropriate for the geological scenario, although it provides some flexibility because layers can pinch out horizontally. Auken and Christiansen (2004) developed a similar approach for a 2D electrical resistivity problem, and deGroot-Hedlin and Constable (2004) for a 2D magnetotelluric (MT) problem.

Michelini (1993) used 2D parametric curves to define interface depths and layer velocities for their 1D seismic travel-time tomography inversions. Each point in the parametric curves defined an interface depth and velocity. The velocity at depth was then interpolated between points. Michelini (1995) extended the idea to 2D using parameterized cubic B-spline basis functions. Roy et al. (2005) used parameterized functions to define a single sub-horizontal interface for a 2D joint inversion of gravity and seismic travel-time data. They used a summation of arc-tangent functions and used a known function to relate density to seismic velocity. Datta et al. (2019) used an SGI to develop an initial model for subsequent voxel-based 2D full-waveform inversion. They parameterized their 2D surfaces using nonoscillatory splines between a few control points free to move in 2D space, with the inversion determining the locations of the control points. Pereyra (1996) considered the 2D and 3D problems of inverting seismic travel-time data, parameterized their surfaces using B-splines, with the inversion determining the control points that defined the splines. Their 3D example involved a single surface representing a mushroom-shaped salt dome.

Similarly, Rawlinson et al. (2001); Rawlinson and Sambridge (2003) investigated the use of a mosaic of cubic B-spline surface patches for representing sub-horizontal layer interfaces for 3D seismic travel-time tomography. Beardsmore et al. (2016) and Scalzo et al. (2019) solved for the shape of sub-horizontal surfaces parameterized by 2D Gaussian process regression against a set of control nodes. These cannot overlap, but can pinch out to zones of zero thickness. While all of these approaches could have been applied to the problem of recovering any surface geometry, including an overturned interface, only Pereyra (1996) did so.

Peng et al. (2019) performed a 2D voxel inversion of MT and seismic reflection/refraction data while also solving for a discrete surface representing the Moho discontinuity. They iteratively updated the discrete surface using H-κ stacking of teleseismic receiver functions, solving for the vertical position of the vertices on their 2D surface. De Pasquale et al. (2019a) inverted electrical resistivity data using a 2D mesh that incorporated a parameterized interface representing a regolith-bedrock contact. They used an underlying 2D mesh of triangles and parameterized their 2D interface as a connection of the triangular edge elements. De Pasquale et al. (2019b) went a step further and conducted joint inversions of electrical resistivity and seismic refraction data. In both approaches, the location of the interface is limited by the design of the mesh but could otherwise generate any shape, including an overturned interface. Similarly, Zhang et al. (2015) inverted seismic data using a 2D mesh with an imbedded interface, but described their interface using an implicit function.

Al-Chalabi (1972) performed 2D gravity inversions that solved for the positions of the vertices in a single sub-horizontal interface. This was similar to the work of Tanner (1967) but with a parameterization that explicitly worked with polyline vertices, and hence relates directly to facetted surface model representations. Smith et al. (1999) and Chen et al. (2012) developed a multi-layer 2D MT inversion method similar to the work of Auken and Christiansen (2004) but with the sub-horizontal contacts described by polylines instead of stacks. However, both Smith et al. (1999) and Chen et al. (2012) inverted for the vertical vertex coordinates only, making their parameterization approaches effectively identical to that of Auken and Christiansen (2004). Narasimha Rao et al. (1995) did similarly to Al-Chalabi (1972), for the 2D gravity and magnetic problems, but also considered a closed polygonal body. Li et al. (2010) also developed a 2D SGI method to recover a closed polygonal body for the 2D controlled-source EM problem, and Koops (2011) did similarly for the seismic travel-time problem. Bijani et al. (2017) performed

SGIs using more complicated 2D models comprising connected polylines, allowing the models to represent arbitrarily complicated geological scenarios, with multiple rock units and different topologies.

With respect to the 3D SGI problem, there have also been many advancements. Lelièvre et al. (2016) stitched several sub-horizontal 2D polygonal interfaces together to model the 3D base of basin sediments. Mallesh et al. (2019) developed a similarly parameterized method, for a similar problem, using an ensemble of horizontally stacked thin tiles, each having an irregular polygonal outline in a vertical plane. Their inversions determined the vertical locations of the polygonal vertices. The approach of Mallesh et al. (2019) can be compared to that of Oliveira et al. (2011) and Oliveira and Barbosa (2013) who approximated a 3D isolated geological body by an ensemble of vertically stacked thin tiles, each having an irregular polygonal outline in a horizontal plane. The vertices of the polygonal outlines were parameterized in a polar coordinate system: in their inversions, the outline vertices for each tile were allowed to move radially away from some central point inside the polygon. Use of these approaches assumes a 3D geological scenario with some discernible major-axis direction for the target body.

Pilkington (2006) inverted gravity and magnetic data jointly to determine the topography of a single 3D sub-horizontal interface. The interface was defined by a uniform grid of surface vertices that could move vertically in the inversion, and forward modelling was performed by applying Fourier transform methods to the gridded information. Foks and Li (2014) performed 3D gravity inversions for a single surface representing the interface between the base of a salt body and the underlying basement rock. Their interface was represented as a sub-horizontal surface of tessellated triangles. Foks and Li (2014) also allowed the triangles' vertices to move only vertically. Hobro and Rickett (2014) used a similar surface model parameterization in their full waveform seismic inversion for a top-of-salt interface. Nishiyama et al. (2017) inverted muon tomography data to image the bedrock geometry beneath an alpine glacier. Their methods recovered a single 3D surface that was effectively parameterized in spherical coordinates, with the parameters being radii at fixed angles away from a muon receiver. Zhang et al. (2019b) also performed an SGI in spherical coordinates, inverting gravity data to estimate the crustal thickness of the Moon, and using two boundary surfaces to represent the crust. Cai and Zhdanov (2015) used a 3D Cauchy-type integral representation of magnetic fields to invert for the depth to basement using a 3D faceted surface. While Foks and Li (2014), Hobro and Rickett (2014), Nishiyama et al. (2017), Zhang et al. (2019b), and Cai and Zhdanov (2015) performed 3D SGIs, their parameterizations still limit the geometry of the recovered models.

Richardson and MacInnes (1989) performed an SGI of gravity data with a more complicated 3D polyhedral source body representing a salt dome. Their model had overturning surfaces rather than simply sub-horizontal layers, approaching the flexibility we are aiming for with our methods. Instead of moving the triangular surface facet vertices explicitly, they reduced the problem size by representing their model with a small number of shape-related parameters, including the height and radius of both the cap and stem of their mushroom-shaped salt dome. The locations of the vertices in the 3D polyhedral salt dome model are known functions of the unknown shape parameters. That is, given values for the shape parameters, one knows how to uniquely generate the corresponding polyhedral model.

3.2 The Developed Surface Geometry Inversion Method

As stated above, many authors have developed methods and examples that come close to this study's interests, although none have approached the complexity we are interested in. This study updates some of the previously published approaches for modern computing platforms, and utilizing modern optimization algorithms. We are extending previous work to: 1) allow for surface-based models of any geometrical complexity, with possibly multiple surfaces connected together; 2) allow more flexibility in the ways that the surfaces can move and contort; 3) include more rigorous, contemporary, global optimization strategies; and 4) include stochastic sampling to provide statistics and enable model appraisal. Lelièvre et al. (2015) and Galley et al. (2019) present some of our earlier work towards this goal, where we developed and refined our SGI method through application to various different geological scenarios and related topologies.

The scope of this study focuses on the numerical methods that comprise our SGI. The novel nature of this work does not lie in the details of the numerical methods themselves; rather, it lies in the integration of the various methods towards the whole SGI algorithm. Hence, the methods section that follows provides a brief global description of the SGI algorithm, followed by brief descriptions of each included method. Simpler synthetic examples are used to demonstrate the basic workings of the approach and we provide a more detailed synthetic example based on a realistic mineral exploration scenario. In the discussion section, we revisit the assumptions, limitations, and possible extensions to our methods. More in-depth investigations are left to future work, for example, questions related to best practices when applying SGI to specific data scenarios.

The presented SGI works with an explicit surface-based model, comprising triangular facets. The surfaces represent contacts between rock units, and the physical properties of the units are fixed during the inversion. The model parameters that the inversion operates on are the coordinates of the vertices of the facets. By moving those vertices in space, and thereby altering the geometry of the model, the inversion attempts to improve the fit between observed data and the calculated response for the model. This is a fairly simplistic explanation of the approach; there are additional extensions and complications that are addressed below.

3.2.1 Model parameterization

Geological models, comprising surfaces that represent contacts between rock units, can be built in many ways. Explicit modelling methods (e.g., Caumon et al. 2009, Lelièvre et al. 2018, and references therein) may build surfaces using parameterized functions, splines, or more directly using meshes of tessellated polygonal facets. Implicit modelling methods (e.g., Lajaunie et al. 1997, Caumon et al. 2013, Hillier et al. 2014, Renaudeau et al. 2019, and earlier seminal references therein) parameterize surfaces as isovalues (contours) within 3D scalar fields. Whether the surfaces are built explicitly or implicitly, ultimately the result is a collection of explicit facetted surfaces that frequently comprise tessellated triangles. Often those surfaces are built for visualization purposes only and do not connect cleanly, although methods have been developed to alleviate this issue (Anquez et al., 2019). However, the presented SGI approach assumes that an explicit surface-based geological model has been built following the requirements of a piecewise linear complex (PLC; see Miller et al., 1996; Si, 2015), which essentially stipulate that the model represents a perfectly water-tight volume (closed surfaces), and that facet edges must exist along any intersections of surfaces within the model.

The vector of model parameters, $\mathbf{m}$, is

$$\mathbf{m} = (x_1, y_1, z_1, x_2, y_2, z_2, \ldots, x_M, y_M, z_M) \tag{3.1}$$

where (x_i, y_i, z_i) are the coordinates of the i^{th} vertex or control node, and M is the number of such vertices or control nodes. There is no requirement that each vertex or control node is free to move in every dimension, and some may remain fixed in place throughout the inversion, depending on the a priori information. Such fixed vertices or nodes are referred to as being “non-dynamic”. Hence, the model may not contain all the vertex coordinate values. The number of vertices or control nodes does not change during the inversion.

Following Foks and Li (2014), Lelièvre et al. (2015) and others (refer to Section 1.5), the solution parameters for the presented SGI are the Cartesian coordinates of the vertices in the explicit surface-based model. The connections between the vertices that define the triangular surface facets remain constant during our inversions. If the physical properties of each unit were allowed to vary along with the vertex locations, this would add a significant amount of non-uniqueness to the problem. Hence, in this study, we treat the physical property information as prior information that is fixed during the inversion; we return to this assumption in Section 3.5.

For large, highly refined geological models, the number of vertices can make the problem infeasibly large to solve on modern computing platforms. Hence, we apply surface-subdivision (see Peters and Reif, 2008) to reduce the number of parameters: the inversion works on the vertices of a coarse control surface (a coarse version of a surface-based geological model) which, after subdivision and interpolation, becomes a candidate model. In 2D, this is akin to fitting a curved line through coarse points. In 3D, the surface-subdivision approach divides each triangular facet in the surface, creating a new vertex on each facet edge, and interpolation is performed to determine the locations of those vertices such that the result is a smoothed (lower curvature) version of the original. Fig. 3.1 illustrates the 3D scenario: Fig. 3.1a would represent the control surface (coarse surface-based model) and Fig. 3.1b or Fig. 3.1c would represent the candidate model (refined surface-based models). If more subdivision steps are used, the result is a smoother model. Hence, surface-subdivision is used as a simple means to define the level of smoothness we want in the models recovered from inversion. The vertices in the control surface are referred to as control nodes.

The subdivision of a coarser surface-based model, with model vector $\mathbf{m_c}$, into a refined version $\mathbf{m_r}$, can be represented as a linear operation

$$\mathbf{m_r} = \mathbf{A}\mathbf{m_c} \tag{3.2}$$

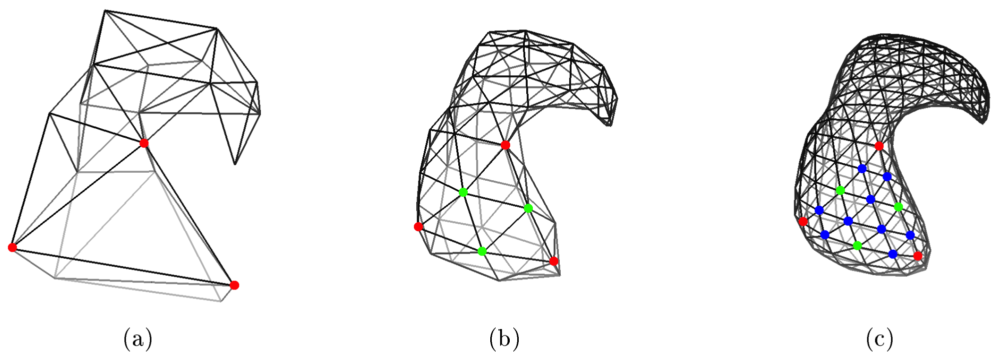

Figure 3.1: A coarse surface object a) shown as a wireframe, subdivided once b) and twice c). Red dots in a) indicate vertices around a single triangular facet. The additional green dots in b) indicate the new vertices added at each facet edge between the red vertices in a). Similarly, blue dots in c) indicate the new vertices for the second subdivision. For the SGI, the coarse object would correspond to the control surface (candidate solution) and a refined, subdivided object would correspond to the surface-based model used for forward modelling.

where **A** is the subdivision matrix. The coordinates of a vertex in the subdivided model is a weighted sum of those surrounding it in the coarse input model. When interpolating new vertex positions, those corresponding to non-dynamic control nodes are never moved from their original positions. When subdividing, if a new vertex is placed on an edge defined by two non-dynamic vertices, then that new vertex becomes non-dynamic. This is simplest to understand when looking at a 2D problem, for example Fig. 3.2, for which the linear operation might look like this:

$$\begin{pmatrix} A \\ a \\ b \\ c \\ C \end{pmatrix} = \frac{1}{8} \begin{pmatrix} 8 & 0 & 0 \\ 4 & 4 & 0 \\ 1 & 6 & 1 \\ 0 & 4 & 4 \\ 0 & 0 & 8 \end{pmatrix} \begin{pmatrix} A \\ B \\ C \end{pmatrix} \tag{3.3}$$

which uses the recipe for cubic B-spline interpolation. In Fig. 3.2a the three red-coloured vertices defining the triangular facet are subdivided by Eq. 3.3 to produce the three additional green-coloured vertices seen in Fig. 3.2b. The same process is performed again to produce the blue-coloured vertices seen in Fig. 3.2c.

Other parameter-reduction alternatives exist for representing a geological model, including the use of different types of splines and level set functions. From any such representation, an explicit facetted surface of any refinement can be built, interpolating the facet vertex positions as required. Surface-subdivision is considered here because it can be easily applied directly to a coarse version of an explicit surface-based geological model.

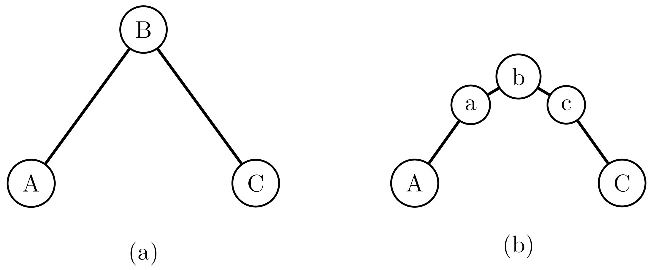

Figure 3.2: A 2D subdivision curve problem. Panel (a) is the curve before subdivision, (b) after. Vertices "a" and "c" are new vertices added on each original edge A-B and B-C. Vertex "b" is the original vertex "B" but with newly interpolated position. Vertices "A" and "C" are non-dynamic and do not move after subdivision.

3.2.2 Forward modelling

For gravity and magnetics data, Okabe (1979) and many others have developed forward modelling approaches for polygonal objects, for example the facets in a surface-based model. The calculation of those geophysical responses for a surface-based model is efficient and simply requires knowing the density or magnetic susceptibility in each region of the model, and knowing which regions are on each side of every surface facet. This form of modelling was employed by Foks and Li (2014) and Lelièvre et al. (2016).

For other geophysical data types, forward modelling methods that rely on a voxel discretization of the Earth can be used. However, this requires an intermediate mesh to be created that honours the contacts in the surface-based model. For example, Hobro and Rickett (2014) used an intermediate mesh to perform the forward modelling for their full waveform seismic problem. Meshing software such as TetGen (Si, 2017) can be used to generate an unstructured 3D mesh comprising tetrahedra that exactly honours the contact surfaces, provided the input surfaces represent a valid PLC. The triangular facets in the surfaces become faces of the tetrahedra in the unstructured mesh. Modelling methods that work on an unstructured mesh (e.g. Lelièvre et al., 2011; Jahandari and Farquharson, 2013, 2014, 2017; Ansari and Farquharson, 2014; Ansari et al., 2017) can then be applied. However, the time requirements for the inverse problem are directly related to the time required to calculate the forward solution, and if a surface-based model must first be meshed, this may add significant computational time overhead.

3.2.3 Inversion

The inverse problem was posed as an optimization problem. We assume that there are more data than model parameters, and we assume that such a situation leads to an overdetermined problem such that only a single objective function term, the data misfit, is required to sufficiently reduce the non-uniqueness of the problem and provide a unique solution. We use the traditional, well-known χ^2 measure of misfit:

$$\Phi = \frac{1}{N} \sum_{i=1}^{N} \frac{\left(F(\mathbf{m})_i - d_i\right)^2}{\sigma_i^2} \tag{3.4}$$

where d_i is the i^{th} observed geophysical data measurement; σ_i is the uncertainty assigned to that data observation; $\mathbf{m}$ is a candidate model vector containing the model parameters (control node coordinates); $F()$ denotes the forward modelling operator, and hence $F(\mathbf{m})$ is the data predicted for the candidate model $\mathbf{m}$; and we have normalized by the number of data, N.

No additional regularization terms are required, which stands in contrast to underdetermined voxel inverse problems (as used in Chapter 2). This is largely a result of the parameterization of the model: with fixed physical properties and only a single topology allowed (as specified by the initial model), the non-uniqueness of the inverse problem is greatly reduced. However, specific model characteristics may be desired and regularization may therefore be incorporated to reduce the space of acceptable models. Koops (2011) regularized their 2D polygonal shape using area, perimeter, and total distance from each polygonal vertex to the centre of mass. Foks and Li (2014) represented their 3D sub-horizontal interface as a surface of tessellated triangles and applied smoothness regularization based on methods by Lelièvre and Farquharson (2013). Adding additional regularization terms to the objective function means that appropriate values for tradeoff parameters, multiplying those terms, must now be determined. While several approaches have been developed to treat tradeoff parameters (e.g. see Hansen and O'Leary, 1993; Farquharson and Oldenburg, 2004), or to perform more thorough solutions to multi-objective problems (e.g. see Bijani et al., 2017; Schnaidt et al., 2018), these are not trivial approaches and the problem is best avoided if possible. In this paper, we adopt the surface-subdivision approach, discussed above, as a reasonable alternative to numerical regularization strategies. We simply have to ensure there are fewer control node coordinates than data measurements to obtain an overdetermined problem. Doing so adds no additional objective function terms or associated tradeoff parameters.

Global optimization

To solve their specific nonlinear SGI problems, most of the authors cited in the introduction of this chapter used iterative, gradient-based, local optimization methods. The reason for this is mostly historical: computing power at the time often limited the feasible optimization methods, and modern global optimization methods may not have been available. As such, many authors focussed most of their efforts on the optimization requirements (e.g. Pereyra, 1996). Using local optimization can be highly dependent on the initial model, particularly where there are multiple minima in the objective function, and model appraisal (e.g. uncertainty assessment) is not usually performed on the solution obtained (Pallero et al., 2015). Furthermore, gradient-based local optimization methods require that first derivatives, and often second derivatives, of the objective function be available. For voxel inversions, closed form mathematical expressions can usually be derived. However, for our highly nonlinear inverse problem, which inverts for spatial coordinates in place of physical property values, deriving the required mathematical expressions is not feasible. Calculating derivatives using numerical means, for example finite-differencing, is possible but adds greatly to the computational time.

With those considerations, employing a global optimization strategy is more appropriate for our SGI. Pereyra (1996) mentioned the possible use of global optimization techniques for solving their SGI problem, though they did not do so. Roy et al. (2005) and Datta et al. (2019) applied simulated annealing to solve their respective 2D parameterized function and 2D spline SGI problems. Paasche and Tronicke (2014) applied Particle Swarm Optimization (PSO) to solve their 2D sharp-interface, layered inverse problem. Pallero et al. (2015) used PSO for their 2D gravity inversion for basement relief in sedimentary basins. They parameterized their single sub-horizontal interface with adjacent vertical prisms, similarly to Tanner (1967). Lelièvre et al. (2016) and Bijani et al. (2017) used a Genetic Algorithm (GA) for their SGIs, and Bijani et al. (2017) also for a sharp-interface discrete-value voxel inverse problem. PSO and GA are metaheuristic algorithms that rely on a “smart random” sampling of the solution space and are able to calculate approximate uncertainty information. De Pasquale et al. (2019a) and De Pasquale et al. (2019b) formulated their SGI in a fully probabilistic framework and employed Markov chain Monte Carlo (MCMC) sampling to obtain a more rigorous statistical sampling.

Both GA and MCMC methods were used during the SGI modelling

. The GA used a single objective to find the global minimum solution, with choices for the various operators (e.g. selection, crossover, mutation) following Deb et al. (2002). However, any sufficiently capable global optimization algorithm could be employed.

Stochastic sampling

After the global minimum solution is found, the solution is fed into a more rigorous MCMC stochastic sampling to provide statistics: mean and standard deviations of the surface vertex positions. The Metropolis-Hastings (M-H) algorithm was used with a single chain. A new candidate solution, $\mathbf{y}$ is selected randomly some distance away from the current solution, $\mathbf{x}$:

$$\mathbf{y} = \mathbf{x} + \gamma \mathbf{r} \tag{3.5}$$

where $\mathbf{r}$ are random values taken from a normal distribution. The acceptance probability is a function of the misfit:

$$\alpha(\mathbf{x}, \mathbf{y}) = e^{\Phi(\mathbf{x}) - \Phi(\mathbf{y})} \tag{3.6}$$

and the scaling parameter γ is automatically determined during run-time to achieve an acceptance rate between 40 and 60 %, following recommendations in Chib and Greenberg (1995) and references cited therein. The inverse of the standard deviations of the surface vertex positions can act as a proxy for confidence in the model, assuming a uni-modal distribution.

Ideally, the GA provides a solution such that the M-H chain is immediately at the required equilibrium state, and it is then unnecessary to perform a burn-in procedure. Investigation of the convergence characteristics of the M-H chain showed this to be true for all examples presented in this paper. A single M-H chain is necessary to calculate the model uncertainty, as convergence to the inverse problem's global minima was reached with the GA optimization.

Intersection detection

A complication for SGI, not dealt with by other authors, is that the surfaces in the recovered model should not intersect, other than as indicated by the initial model. That is, if two surfaces in the initial model connect, following the requirements of a PLC, then the recovered model should have those two surfaces connecting along the same facet edges, but not intersecting elsewhere.

Similarly, if two surfaces in the initial model do not intersect, then they should not do so in the recovered model. Nor should a single surface wrap around and intersect itself. Given the semi-random alteration of the control nodes' positions via global optimization, such intersections are inevitable in the candidate models. In some simpler situations, bounds could be placed on the node positions to avoid such intersections. However, the bounds on the node positions must be made large enough to account for any geometric feature present in the true model, and generally this leads to intersections.

To check for disallowed intersections, every possible pair of facets in the model was looped over and triangle-triangle intersection (TTI) tests were performed using the method of Möller (1997). During the MCMC optimization a candidate solution containing facet intersections is not accepted. Our GA considers both the objective function (data misfit) and a constraint violation value for a candidate model; the constraint violation acts as a rejection filter for any undesirable self-intersecting surface models. The constraint violation was defined as the number of pairs of intersecting facets in the model, as determined by the TTI tests:

$$c = \sum_{j=1}^{P} \sum_{k=1}^{P} TTI(\mathbf{p}_j, \mathbf{p}_k) \tag{3.7}$$

where P is the number of facets in the surface-based model, $\mathbf{p}_j$ denotes the vertex coordinates of the j^{th} facet, and TTI denotes our triangle-triangle intersection test:

$$TTI(\mathbf{p}_j, \mathbf{p}_k) = \begin{cases} 0, & \text{if } j = k \\ 0, & \text{if facets } \mathbf{p}_j \text{ and } \mathbf{p}_k \text{ do not intersect} \\ 1, & \text{otherwise.} \end{cases} \tag{3.8}$$

The individuals in the GA population must be ranked prior to selecting individuals for crossover and mutation. Feasible solutions, which contain no intersecting facets, are ranked by their objective function value. Infeasible solutions, which contain one or more pairs of intersecting facets, are ranked by their constraint violation values. Feasible solutions are ranked fitter than infeasible solutions. While it is certainly possible for the random initial GA population to contain only infeasible solutions, it was found that the definition of constraint violation above enabled the GA to quickly find feasible solutions for all of the study's examples.

3.2.4 Overview of the SGI algorithm

Fig. 3.3 outlines the major components of the SGI algorithm and how information is passed between them. Prior information includes observed geophysical data, topological rules, an initial model (a surface-based geological model) and bounds on the model parameters (the facet vertex coordinates). The initial model and bounds are passed to the GA global optimizer, which generates an initial population of candidate solutions from that information. A candidate solution may hold the vertex coordinates for a surface-based model or for a control surface that requires subdivision and interpolation operations to generate a candidate surface-based model (see Fig. 3.1). In either case, the surface-based model gets fed into the forward solver. For each candidate surface-based model, the forward problem is solved to generate the geophysical response; each response is compared to the observed data and a data misfit is calculated. Intersection detection methods are applied to the candidate models to check they honour the topological rules; a corresponding measure of constraint violation is calculated for each model. The data misfit and constraint violation values are provided to the global optimizer which uses that information to generate a new population of candidate solutions; for example, a Genetic Algorithm would rank the previous candidate solutions by their data misfit and constraint violation values, then take the most promising individuals and use them to generate the next population through crossover and mutation operations. Convergence occurs either when a feasible solution is found with a low enough misfit value, or when a sufficient number of iterations has occurred.

The SGI is performed in two stages. First, a global optimizer is used to find a single best (globally optimal) solution, following the procedure described above. Second, that best solution is used as the initial sample in a MCMC stochastic sampling, which generates statistical information for use in model appraisal. For the MCMC sampling, Fig. 3.3 still applies but with a population of one individual.

3.3 Modelling Capabilities

Here several synthetic examples are presented to demonstrate and test the developed SGI method. The first two examples use simple blocky shapes in a half-space. Those examples serve only to assess the mechanics of our SGI and prove they can provide accurate solutions in idealized cases. The third example applies SGI to a synthetic model based on a SMS deposit, with a more

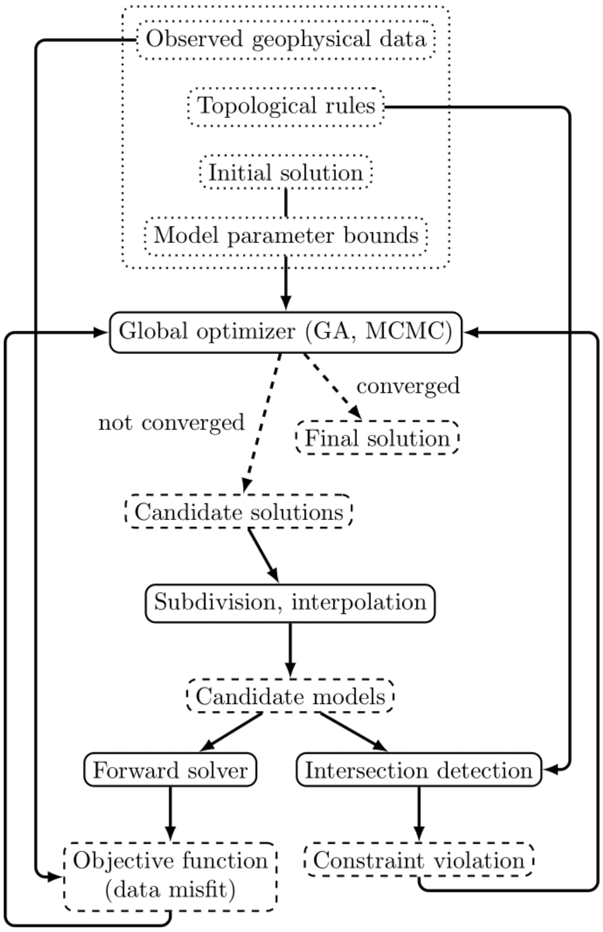

Figure 3.3: An illustrative diagram of the components of the SGI algorithm. Dots surrounding text indicates prior information. Solid lines surrounding text indicates the major components of the algorithm, while dashed outlines indicate intermediate products of those components. Dashed lines indicate two convergence decision paths.

complicated geological model comprising multiple connected contact surfaces and multiple rock units.

The first example demonstrates the SGI method's ability to resolve the geometry of a target when the initial surface model contains the same number of nodes, and the same node connections in the facet definitions, as the true model. The second example investigates the effects of assuming an incorrect topology of a two prism target. Topology is referred to as the mathematical concept: the properties of a geometrical object preserved through continuous deformations. In the third and final example the SGI method was applied to a synthetic scenario based on an SMS deposit, and a subdivision was used to reduce the number of inversion parameters. In all the examples the GA optimization was used with a population equal to ten times the number of inversion parameters.

In each example, the modelling began with a voxel inversion, then used that result to generate an initial surface model for an SGI. For the single and double prism examples, rectilinear voxel meshes were used in the inversion, whereas an unstructured voxel mesh was used for the SMS example. Voxel inversions were used first because the SGI required an initial approximation of the anomaly's topology and geometry, which a voxel inversion could provide robustly, with little a priori knowledge of the subsurface. In practice, such an initial model for SGI may come from geophysical inversion or geological modelling. In all examples, the "inverse crime" was avoided: the true data response was calculated using a different mesh than used in the inversions. Furthermore, for the latter two examples, the SGIs used models with facet definitions (node connections) that were different from in the true model.

All voxel inversions were performed with a total variation smoothness measure on the model, along with a sensitivity weighting (see Section 1.5). No explicit regularization was applied during the SGIs, although cubic B-spline subdivision was used in the final SMS example. Each inversion was run in parallel on 48 threads on a 2.20 GHz Intel Xeon E5-2650 Processor.

3.3.1 Single dipping prism

In the first example, we used the single 3D dipping prism presented in Li and Oldenburg (1996), which had a magnetic susceptibility of 0.06 SI within a zero susceptibility half-space. The synthetic data for this and all other examples were generated from the true model using an inducing field with strength 50,000nT, inclination 75° and declination 25° (values taken from

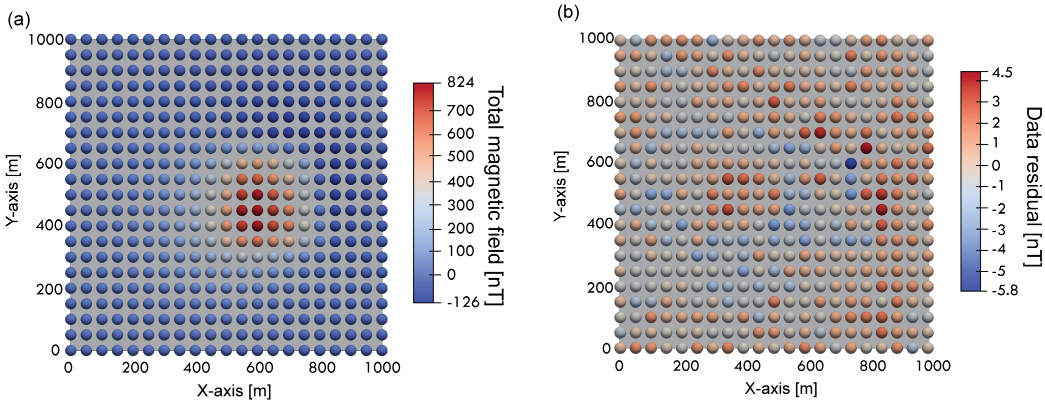

Figure 3.4: The data used in the single dipping prism example. (a) the 441 data points and their total magnetic field values. (b) the normalized data residual from the SGI.

Li and Oldenburg 1996). We added Gaussian noise of 2 % standard deviation with an absolute floor of 1 nT. This data was gridded over the 1,000 m $\times$ 1,000 m horizontal inversion domain at a constant elevation of 1 m with an observation point spacing of 50 m, yielding 441 data points (see Fig. 3.4). The rectilinear inversion mesh used in the inversion had the dimensions of 1,000 m x 1,000 m x 500 m, which was discretized into 62,500 cubic cells with side lengths of 20 m.

The intention is to incorporate The SGI methods into a workflow that includes both SGI and voxel inversion. To provide one possible example, the voxel inversion results were used to build a surface-based model estimate of the target's geometry. First, the spatial gradient of the voxel model was calculated to indicate the locations of likely interfaces between rock units, Fig. 3.5a. The program FacetModeller (Lelièvre et al., 2018) was then used to build a surface-based model that approximately followed those likely interface locations, Fig. 3.5b. This initial model was designed with the same number of nodes and facet definitions as the true model. Again, this was done to demonstrate the SGI method's ability to resolve the geometry of a target in an idealized scenario, i.e. when all prior information is accurate.

The eight nodes in the initial surface model were all allowed to move during the SGI, leading to 24 inversion parameters: eight nodes with three Cartesian coordinates each.

After the GA optimization of the surface model, an MCMC sampling was used to calculate statistics on the inversion results, including a standard deviation for the position of each node in the surface models, see Fig. 3.5c. The recovery of the bottom of the body was worse than for the top, as expected because of the lowered sensitivity of the magnetic field data with increasing depth. The MCMC sampling provided a consistent story, with higher confidence (lower standard deviations) closer to the data. Through forward modelling it was calculated that the signal

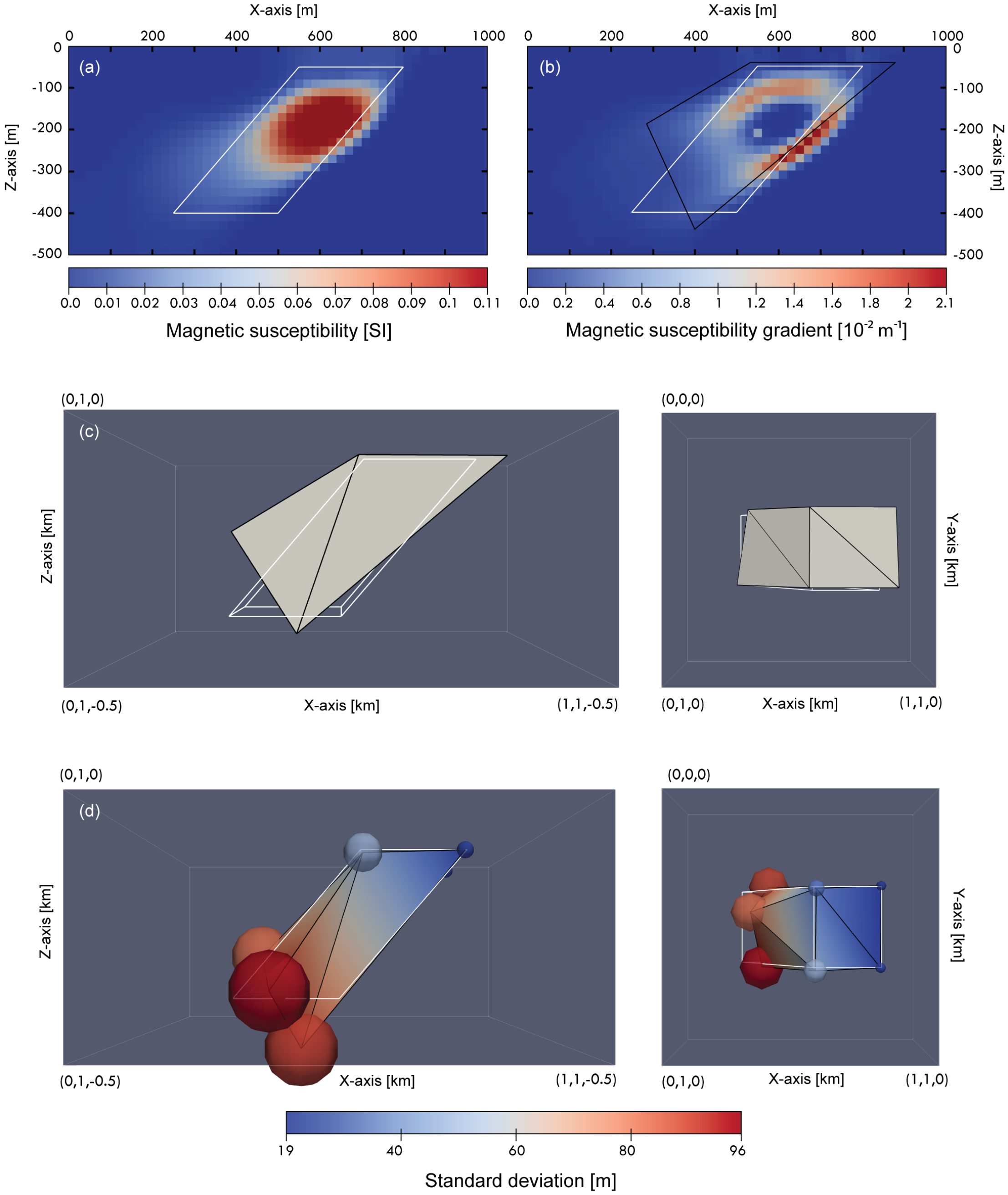

Figure 3.5: Voxel and SGI results, and the design process of the initial surface model. a) A cross section of the voxel inversion and b) its gradient model, right, of the single prism at $y = 500$ m, with the outlines of the true model in white and the intial surface model in black. c) The initial surface model in 3D, as a grey polygon outlined in black, with the true prism model outlined in white. d) The SGI result of the single prism example in 3D. The inversion model is shown with its surfaces coloured corresponding to the uncertainty of its position. As an additional visualization tool, the uncertainty of the position of each of the eight nodes is represented by coloured spheres, whose radii are equal to the nodes' standard deviations.

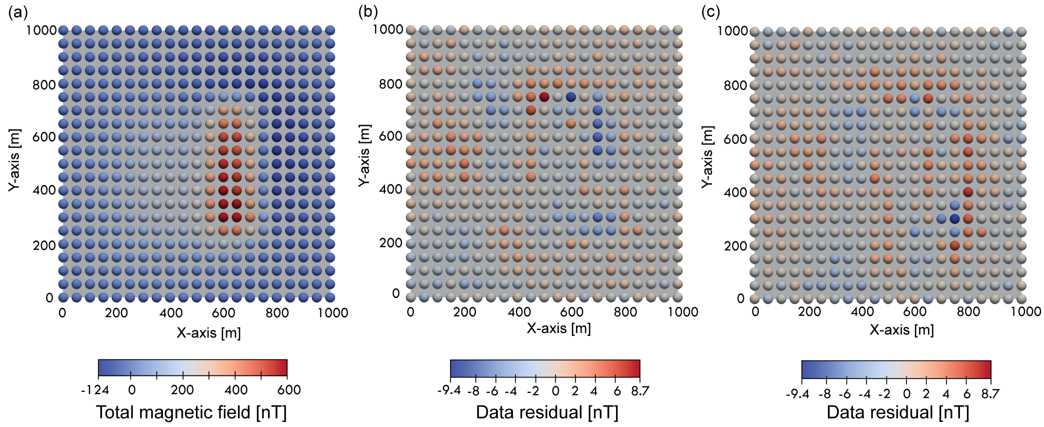

Figure 3.6: The presented three plots display the data used in the two dipping prisms example, along with both SGI's data residuals. a) The total magnetic field data observed at each data point, which lie on a plane with a constant 1m elevation. b) and c) show the data residuals from the cases where it is assumed that there are two separate volumes in the sub-surface and one single volume, respectively.

produced by a regular tetrahedron of height 100 m protruding from the base of the true model had an amplitude of 0.7 nT. If this tetrahedron was thought to represent a segment of the SGI model which expanded too far, as in Fig. 3.5d, then its contribution to the overall forward signal of the SGI model will be minimal, and well below the data's noise.

Throughout all optimizations, spacial bounds of ± 100 m relative to the initial model were used to constrain the nodes' positions. An initial population of 240 was used for the GA optimization, ten times that of the number of inversion parameters. The GA took 11 seconds and 894 iterations to converge from an initial misfit of 2.94×10^3 to a final misfit of 1.0, with 2 % of that time used to calculate possible facet-facet intersections. The MCMC sampling took 14.4 minutes to complete 1.2 million iterations.

3.3.2 Two dipping prisms

The second example followed that of the two prism model from Li and Oldenburg (1996), with two dipping prisms of equal magnetic susceptibility (0.06 SI) in a non-susceptible half-space. The data were generated in the same fashion as the previous single prism example, using 441 observation points with similarly generated Gaussian noise, Fig. 3.6.

The initial surface mesh was first designed with the correct topology: two isolated anomalous units. The same methodology was followed as the previous example, of running a voxel inversion and approximating the geometry of the recovered bodies based on the magnetic susceptibility gradients, Fig. 3.7a. This resulted in the model of Fig. 3.7b, composed of 43 nodes (129 inversion parameters) and 82 facets. The SGI was performed with a GA population of 1290.

To study the effects of incorrectly generating the initial surface model, with respect to the true model, the data was inverted assuming that there was only one anomalous unit in the subsurface, Fig. 3.7c. This single volume was defined with 40 nodes (leading to 120 inversion parameters) and 72 facets, and the GA was performed with 1200 candidate solutions.

The uncertainty in both single and double volume models was again calculated via MCMC sampling. The results of both SGI's are seen in Fig. 3.8a and Fig. 3.8b. Compared to the initial model used to begin the double prism SGI, Fig. 3.7d, the inversion result, Fig. 3.8b, demonstrated a thinning of the connector joining the two prisms. This shows that despite giving the SGI program an inaccurate starting model, it can alter it to produce an inversion model which still resembles the true model, and suggests the ground truth to the user. Along the y and z directions, the inversion was able to adequately recover the extent of the true surfaces, especially the tops of both prisms. The recovery of the ground truth became less accurate along the x direction, where the presence of the connector segment of the single anomalous volume added more susceptible material between both prisms. This additional material caused the SGI model to be offset from the true model, notably seen with the lower prism in Fig. 3.8b, where its form was resolved but offset to the left (in the negative x direction).

For the double volume model, the GA optimization took 1.5 hours and 1163 iterations to converge from an initial misfit of 409 to a final misfit of 1.0, with 3 % of that time used to calculate possible facet-facet intersections; the MCMC sampling took 1.4 hours to complete 1.2 million iterations. For the single volume example, the GA took 1,616 iterations to converge from an initial misfit of 843 to a final misfit of 1.0; the MCMC sampling took 1.9 hours to complete 1.2 million iterations.

3.3.3 Seafloor massive sulfide deposit

The last inversion example is that of a synthetic seafloor massive sulfide (SMS) deposit. These hydrothermally driven deposits, which form on or near the surface of the seafloor, are not yet being mined but are of growing importance in economic geology (Hannington et al., 2011). Being able to accurately model the sub-seafloor structure of these deposits with SGI would allow the geometry and volumes of their massive sulfide lenses and stockwork feeder systems to be

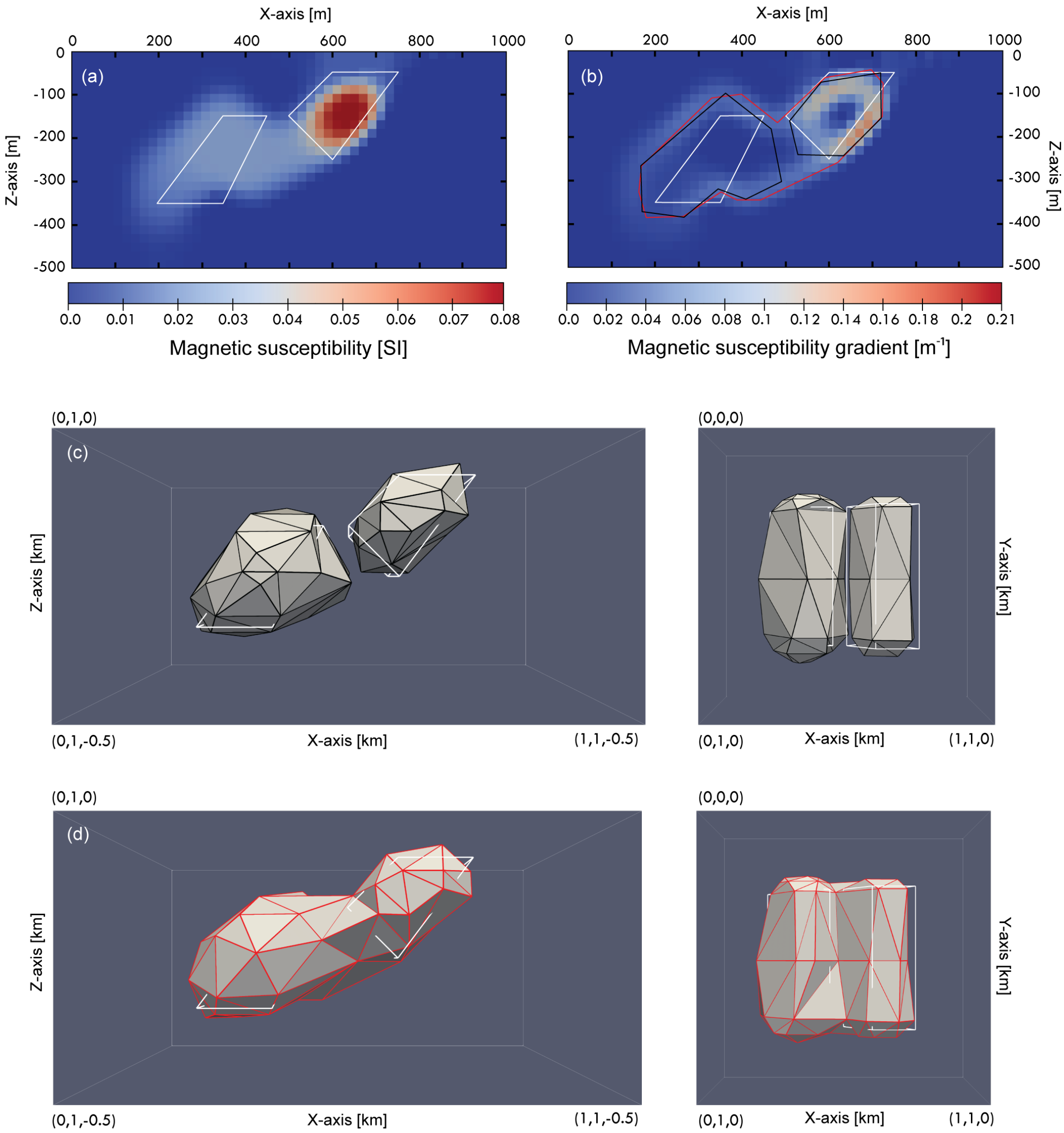

Figure 3.7: Initial model design for the two dipping prisms example. a) a cross section of the voxel inversion and b) its gradient model of the double prism at $y = 500$ m, with the outlines of the true model in white, the initial model assuming two separate volumes outlined in black, and the initial model for the single volume outlined in red. c) and d) 3D views of the double and single volume initial models, respectively, with the true model shown as a white wireframe.

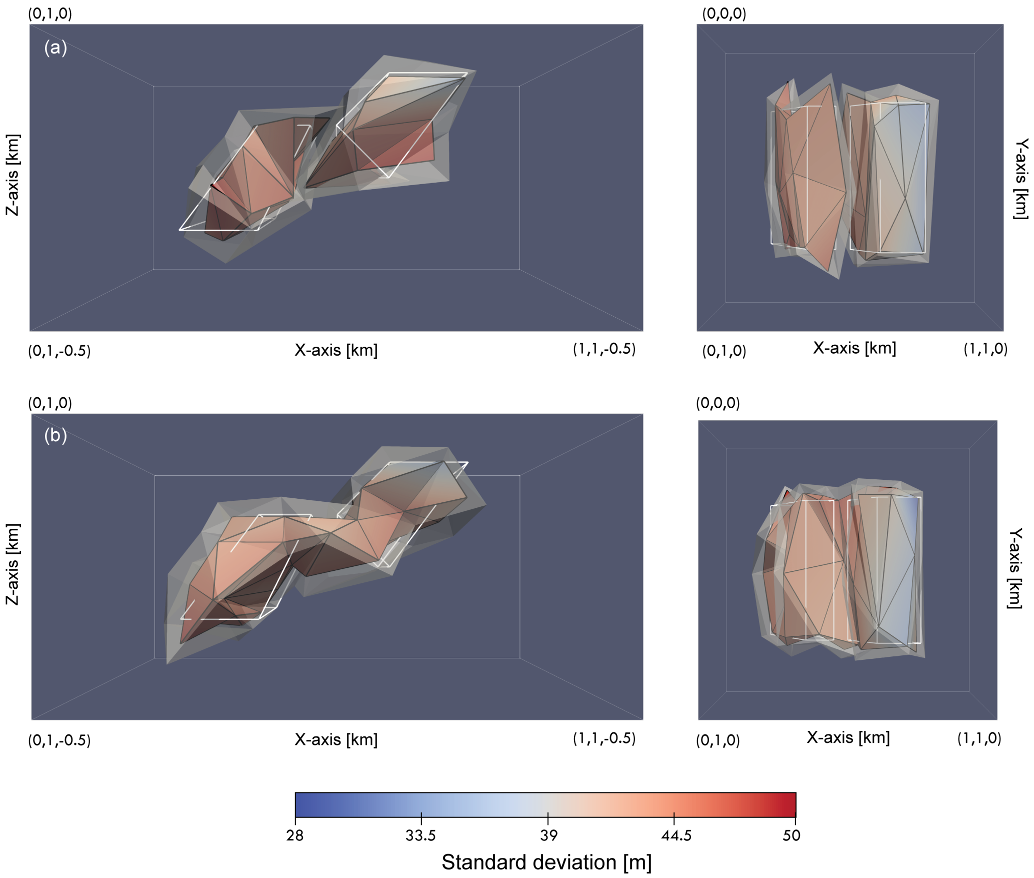

Figure 3.8: SGI inversion results for the two dipping prism example. a) Inversion results when the anomaly is assumed to contain two separate volumes. b) Inversion results when only one volume is assumed. In both, the true model is outlined with a white wireframe, and the inversion model is coloured to indicate the standard deviation of the position of the models' nodes. As an additional visualization aid, a translucent grey surface is added on top of the SGI results, which represents the inversion model expanded by one standard deviation of its position uncertainty.

approximated, leading to more accurate tonnage models for these deposits.

This example demonstrates the SGI method's ability to remove topographic surfaces from the initial surface model. This allows topographically complicated systems to be efficiently modelled without any reduction in resolution, as none of it need be included in the inversion process. Additionally, the use of subdivision during the inversion, which acts as a sort of regularization to smooth out the model and allows a few control nodes to control a finer surface mesh, was used to model the SMS synthetic.

A synthetic SMS system can be modelled by dividing the deposit into two main zones, its massive sulfide lens and the stockwork zone. The massive sulfide lens in this example is exposed on the seafloor, representing a generalized active or recently inactive hydrothermal system, akin to the Trans-Atlantic Geotraverse (TAG) deposit (Humphris et al., 1995). The stockwork zone is entirely below the seafloor, connected to the base of the massive sulfide lens, Fig. 3.9. Only the stockwork zone and the sub-seafloor region of the massive sulfide lens were actively altered during the SGI process, because the surface of the massive sulfide lens would be known through bathymetric studies.

This example is similar to the salt-dome model presented by Richardson and MacInnes (1989), in which a relatively simple shape is represented by a wireframe surface. In their example, the salt-dome shape is moved using a few shape parameters, e.g. those that describe the stem radius, height, and thickness of the cap. The SGI inversion methods differ in that they provide more flexibility in the ways in which the shape can move and contort.

The true model was designed to include a topographic surface with a normal fault hosting the SMS deposit. The background was treated as basalt, with a magnetic susceptibility 10^{-2} SI, the stockwork had magnetic susceptibility of 10^{-4} SI, and the massive sulfide lens a value of 10^{-5} SI. These physical property values were loosely based on measurements collected at TAG (Zhao et al., 1998), and were considered known during the modelling.

The observed data comprised 13 lines with 10 m spacing in the x-direction, and 5 m along line in the y-direction. This totalled 401 observation points, all positioned at an altitude of 5 m with respect to the seafloor. Each point had a 0.12 SI standard deviation Gaussian noise added to its observed signal. The 0.12 SI was derived from measuring the signal of the bottom most segment of the stockwork zone, ensuring that the noise in the system was just low enough such that all components of the true model should be able to be resolved through inversion modelling.

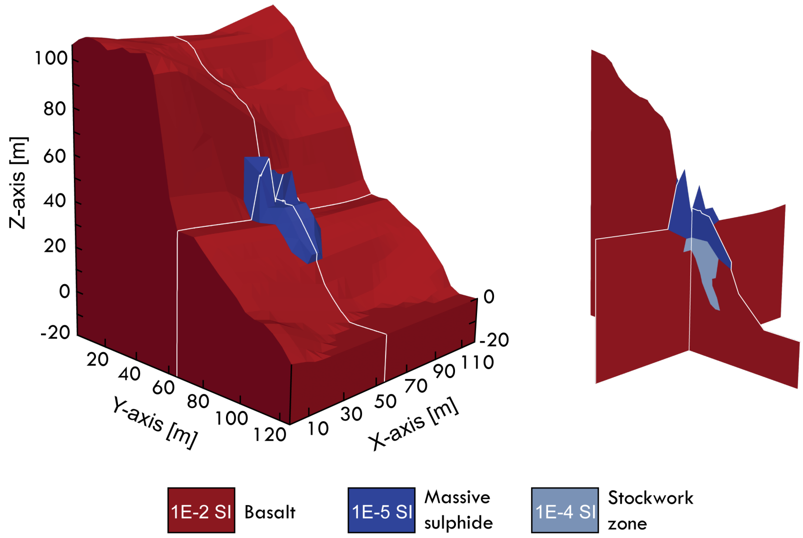

Figure 3.9: The true model used in the SMS example. On the left is the entire model, with two white lines draped on top to indicate the position of the cross sections that are shown to its right. These cross sections are at $y = 65$ m and $x = 55$ m. Both the entire model and cross-sections are coloured as explained by the legend, displaying the three unique rock units and their magnetic susceptibilities.

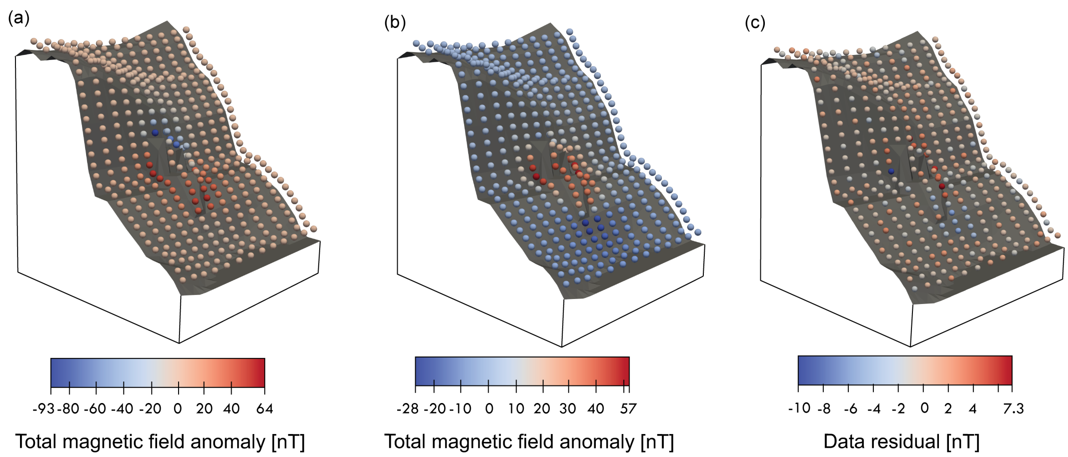

Figure 3.10: The observed data used in the SMS voxel inversion and SGI, as well as the data residual from the SGI. a) Observed data with the forward signal of a homogenous sub-surface subtracted out, leaving only the magnetic signature of the SMS deposit. b) Data from a) but with the forward signal of the top surface of the massive sulfide mound subtracted out. The remaining signal is only due to the sub-surface component of the SMS deposit, whose geometry was inverted for with the SGI method. c) Data residual from the SGI inversion result.

In preparation for both the voxel inversion and SGI, the forward signal associated with the background basalt was subtracted from the total signal by treating the subsurface as having a constant 10^{-2} SI magnetic susceptibility. The resulting signal, which was used in the voxel inversion, contains only the response of the anomalous SMS deposit, Fig. 3.10.

From the voxel inversion results, as shown in Fig. 3.11a and b, an initial model of 20 nodes and 54 facets was constructed for the subsurface massive sulfide layer and the stockwork zone, Fig. 3.11b. Only the subsurface components of the deposit needed to be modelled in the SGI, since, as said previously, the outcropping portion of the massive sulfide lens would have its geometry known. Since the faceted surface of the lens was fixed during the inversion, time would be wasted calculating its unchanging forward signal each iteration, for each candidate model. Therefore, the forward signal for the top of the lens was calculated, and subtracted form the anomalous signal. This left a magnetic anomaly purely resulting from the subsurface components of the SMS deposit, Fig. 3.9.

To demonstrate an ability of the SGI to further reduce the number of inversion parameters, a subdivision was performed on the sub-seafloor component of the SMS deposit, using a cubic B-spline interpolation. This interpolation allowed a smooth surface defined by 124 nodes to be modelled by 20 control nodes, as shown in Fig. 3.12. The subdivision was used throughout the inversion process, resulting in the model as presented in Fig. 3.13.

The GA took 17.7 minutes and 192 iterations to converge from an initial misfit of 1.36×10^3 to a final misfit of 1.0. The MCMC sampling took 9.9 hours to complete 1.2 million iterations.

3.4 Physical Property Uncertainty Assessment

A significant assumption that has been made in the developed SGI method's design is that the physical property of each rock unit in the model was treated as known information, and remained fixed during the inversion. It is trivial to allow those physical properties to change as well as the surface geometry parameters (control node coordinates) by adding the physical properties of each homogeneous model region to the model parameter vector $\mathbf{m}$ in Eq. 3.1. Beardsmore et al. (2016) and Scalzo et al. (2019) can include variable physical property values in their probabilistic framework, incorporating a priori physical property distributions for each assigned rock unit, with those PDF's coming from laboratory measurements. However, unless

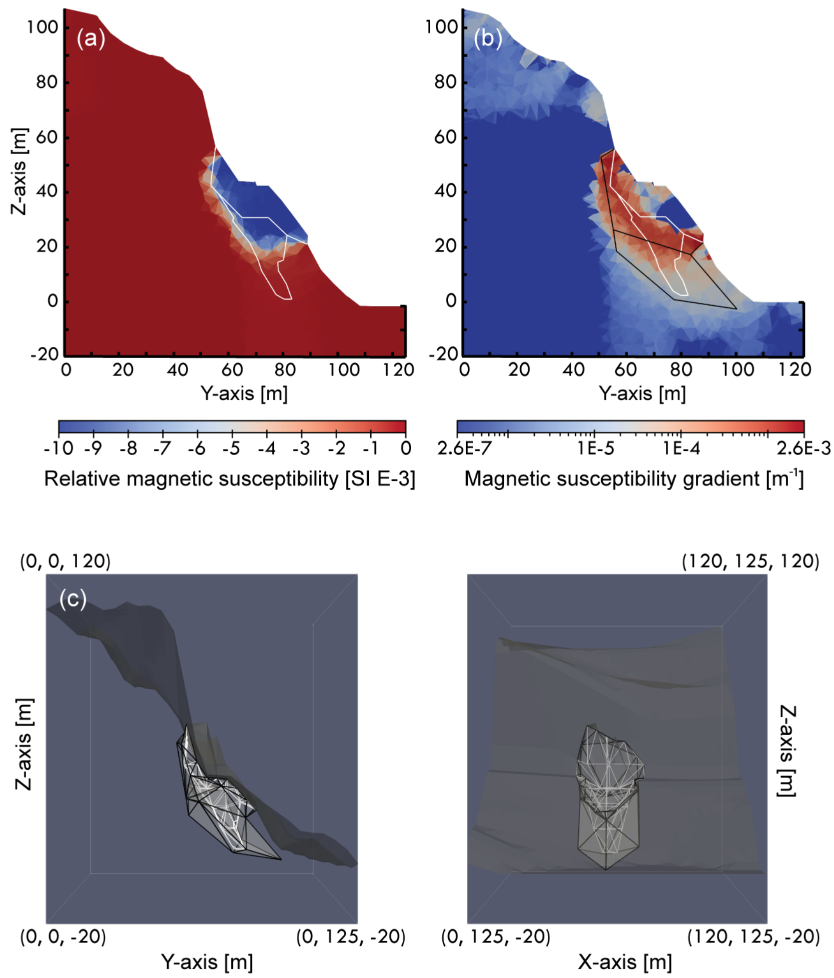

Figure 3.11: The results of the voxel inversion of the SMS target, and the initial surface model used in the SGI. a) and b) Two cross sections of the voxel inversion result at $x = 55$ m with the true model outline in white, and the initial surface model outline in black. a) The cross section shows the distribution of magnetic susceptibility across the cell on the inversion results, b) the model's magnetic susceptibility gradient magnitude at each cell. c) A 3D comparison of the initial surface model, the translucent grey surface outlined in black, compared to the true model of the SMS deposit, outlined in white. The bathymetric surface of the model is shown as a translucent dark grey mesh.

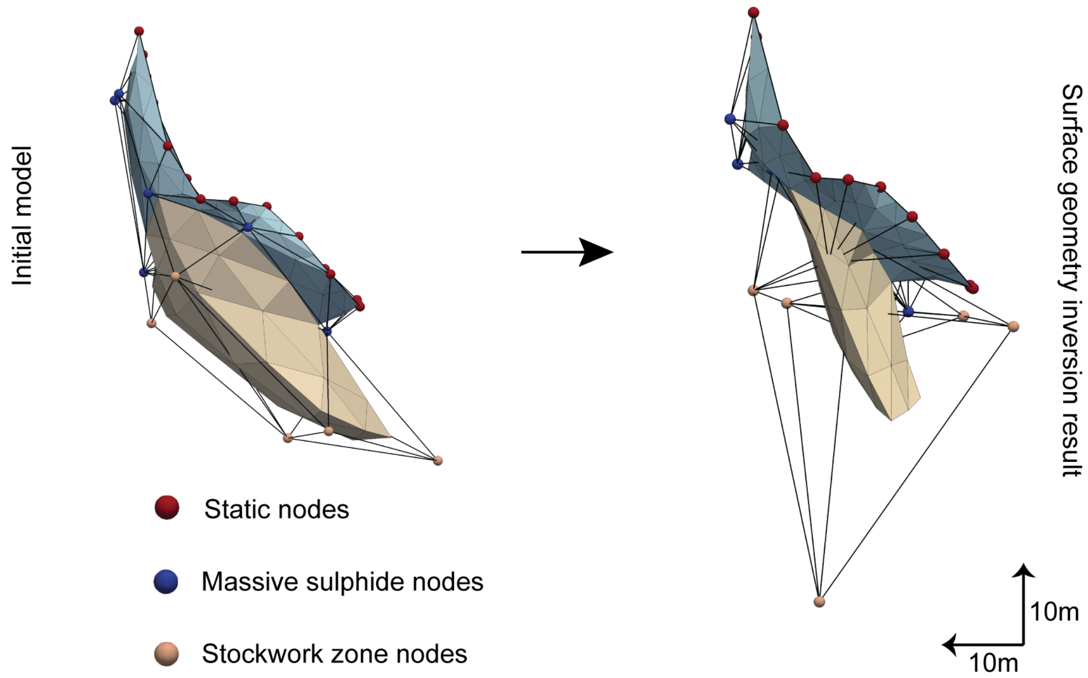

Figure 3.12: These images demonstrate the interpolation that can be performed during a SGI. The left image shows the constructed initial surface model as a black wireframe mesh, with its subdivided surface shown in grey. The right image shows the result of the SGI using the initial model. In both models, the control nodes of the wireframe model are shown, coloured based on their associated rock unit. The red nodes were fixed during the inversion, as they rest on the bathymetric surface. The blue and yellow nodes, those of the massive sulfide lens and stockwork zone respectively, were dynamic throughout the SGI.

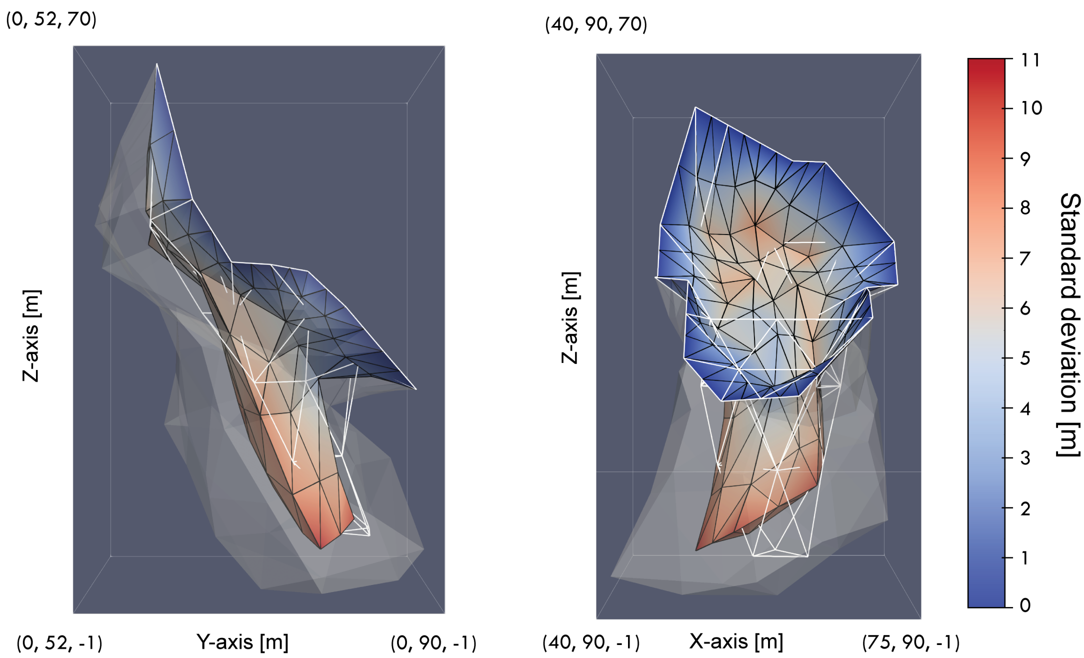

Figure 3.13: The results of the SGI from the SMS example, viewed from the side and from above. The coloured surface is the inversion model, with colours corresponding to the standard deviation of the model uncertainty. Additionally, the inversion model expanded by one standard deviation is shown as a translucent grey surface. The true SMS model is shown as a white wireframe mesh.

the physical property distributions represent a relatively tight range of values for each rock unit, allowing variable physical property values will significantly increase the non-uniqueness of the problem. This would require alterations to the SGI formulation to obtain meaningful solutions. More research is required to assess this. One alternative to allowing the physical properties to vary inside the inversion might be to perform multiple inversions with different fixed physical property values, within the expected limits, and perform some model appraisal on the suite of solutions. Based on prior knowledge, geologically unrealistic solutions could be rejected, with the remaining solutions being used to access features of higher confidence.

To demonstrate this methodology an example was developed that inverted for the single prism true model from the prior synthetic tests. In this example the magnetic susceptibility within the prism was adjusted to $\pm$ 20 % from its true value (0.06 SI, Fig. 3.14a), so one test with an internal susceptibility of 0.072 SI (Fig. 3.14b) and the other with 0.048 SI (Fig. 3.14c). To begin the SGI an initial model composed of 21 vertices was used (Fig. 3.15), leading to a GA population of 630 during the inversion. All vertices were bounded by $\pm$ 100 m relative to their position in the initial model.

Another option to assess the effects of assuming a fixed physical property is to determine an empirical relationship between the uncertainty in the model's physical properties and the resulting uncertainty in the inversion model's vertices. With this empirical relationship post-inversion calculations can be applied to the SGI model to determine any model uncertainties related to uncertain physical property values.

To determine the relationship a number of tests were designed. In each test some true model was designed, the forward signal calculated for the model, and then SGI's done using the true model as the initialization model but with varying anomalous magnetic susceptibility values. For example, consider the cubic model, made up of eight nodes with an anomalous magnetic susceptibility of 100 SI inside a 0 SI half-space. To test the cube's model uncertainty SGIs were done with anomalous magnetic susceptibilities varying between -90 % to 200 % at 10 % difference intervals with respect to the anomalous value, with three additional tests at 300 %, 600 % and 1000 %, see Fig. 3.16. This test was repeated 100 times to calculate standard deviation information.

This form of testing was done for multiple true model geometries, as well as different anomalous magnetic susceptibilities to determine a universal empirical relationship. The other models

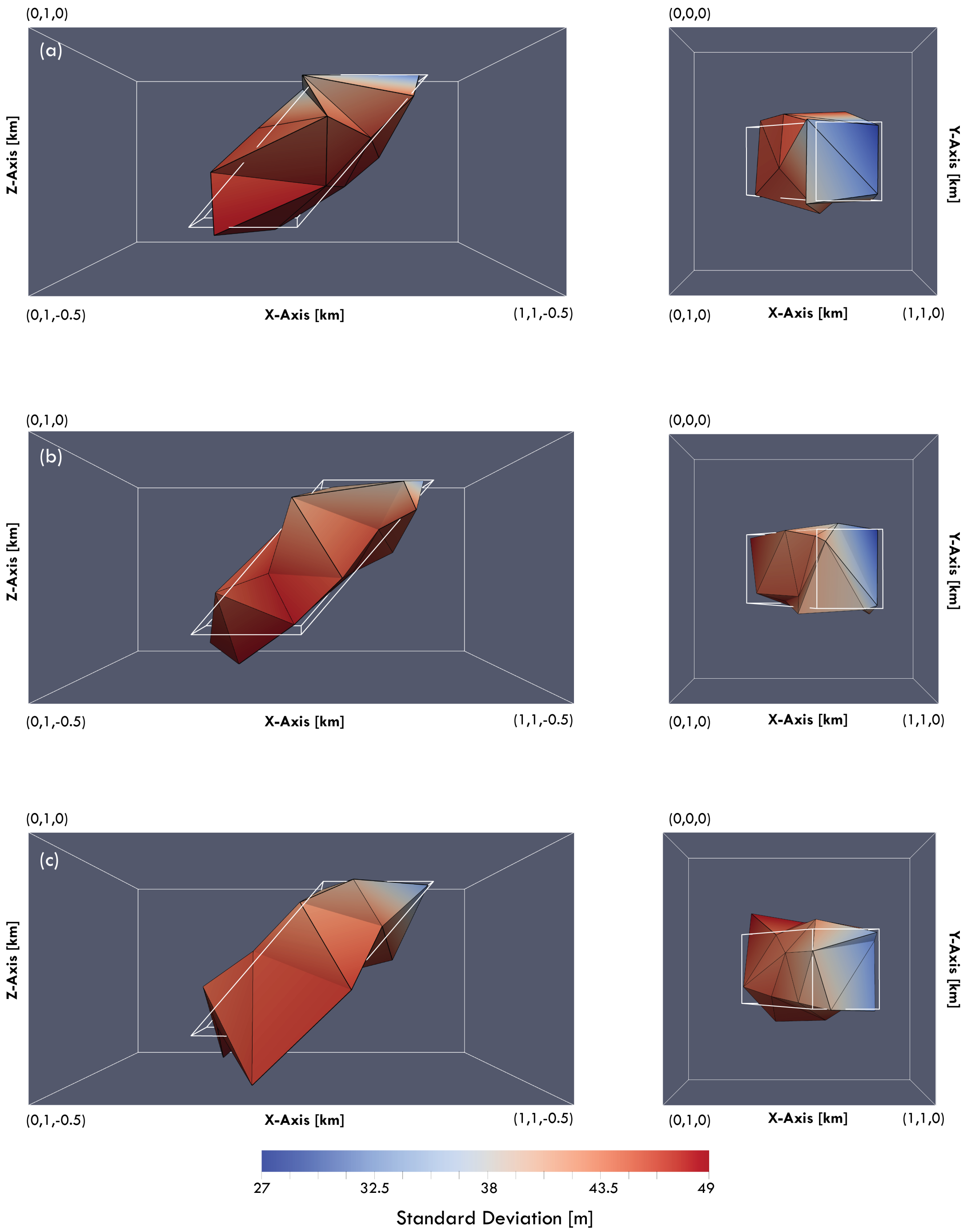

Figure 3.14: The results testing different anomalous magnetic susceptibilities during each SGI. a) The SGI model assuming the correct 0.06 SI magnetic susceptibility, b) the model assuming 0.048 SI, and c) the model assuming 0.072 SI.

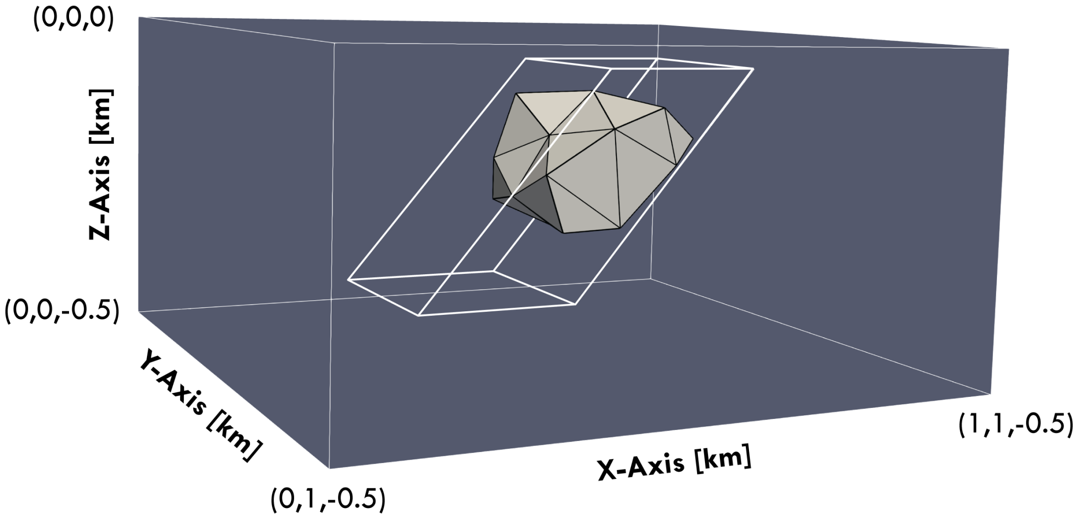

Figure 3.15: The initial model used in the testing of varying magnetic susceptibility values during an SGI shown as a grey model within a white wireframe representing the true synthetic model.

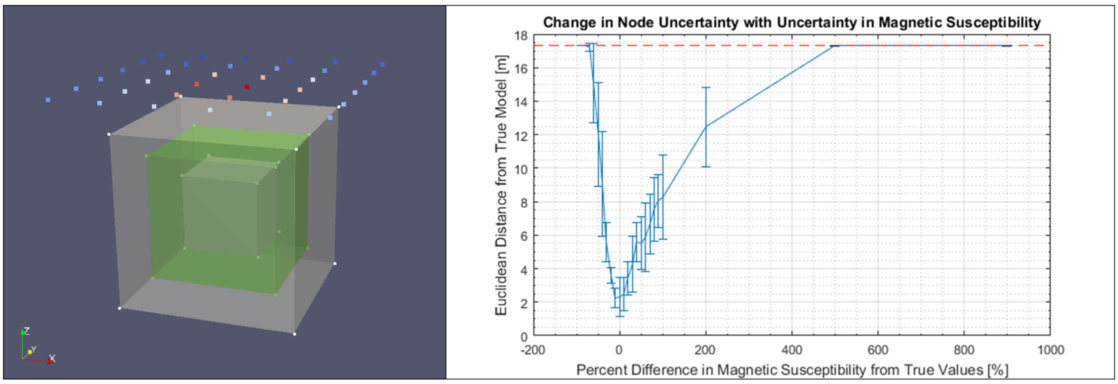

Figure 3.16: A display of the effects of the uncertainty in assumed magnetic susceptibility on the uncertainty of the inverted model's nodes. The left hand image shows the true model in green (magnetic susceptibility of 100 SI), with two resulting inverted models, the inner most model with assumed magnetic susceptibility equal to 1000 SI, and the outer model with magnetic susceptibility equal to 10 SI. The red dotted line shows the asymptote of the data ($\sqrt{300}$ m $\simeq$ 17.32 m), as in the inversion the nodes of the square model were bounded by $\pm$ 10 m in each Cartesian direction.

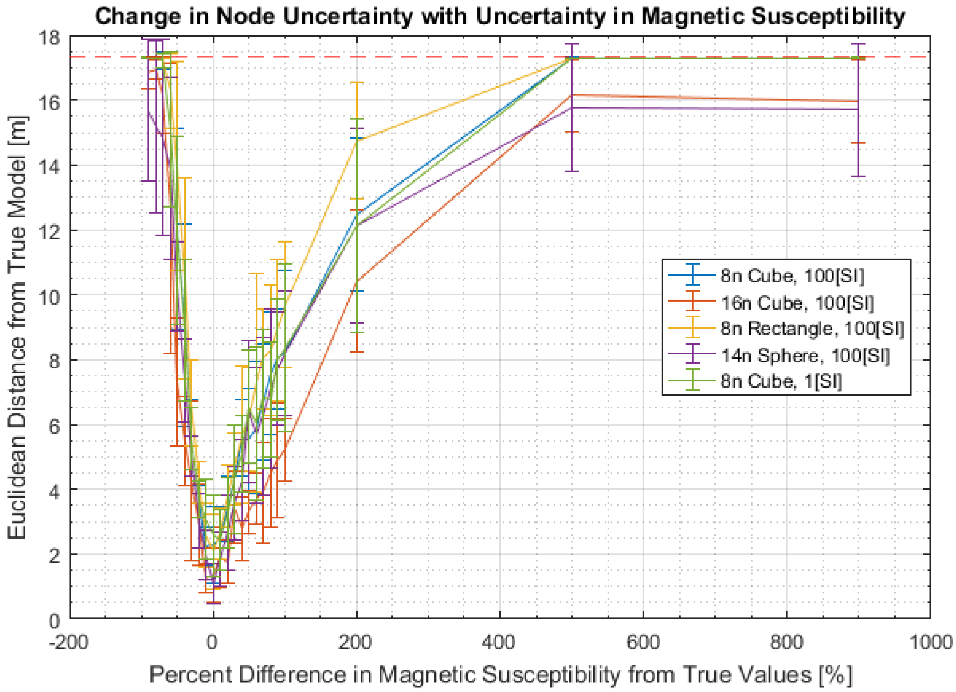

Figure 3.17: A display of the effects of the uncertainty in assumed magnetic susceptibility on the uncertainty of the inverted model's nodes for different models. The different models are: a cube made of eight nodes, a cube made of sixteen nodes, a vertical rectangular prism made of eight nodes, and a sphere of fourteen nodes, and a eight node cube with a lower internal magnetic susceptibility. The red dotted line shows the asymptote of the data, approximately equal to 17.32 m.

were a cube made of sixteen nodes (as seen in Fig. 3.18), a vertical rectangular prism made of eight nodes, and a sphere of fourteen nodes; all with true magnetic susceptibility values of 100 SI and a background of 0 SI. Additionally, another test was done with the eight-node cube with internal susceptibility of 1 SI. The results of the tests are shown in Fig. 3.17.

All geometries have similar behaviour, with the exception of the sixteen node cube and the sphere. Both of these approach a lower asymptote than the other models, due to the complexity of their nodes' layout.

All nodes, when inverted, are constrained. In the case of these tests they are constrained in Cartesian space by $\pm$ 10 m. This means that the furthest a node may exist from the starting model is $\sqrt{3 \times 10^2} \simeq 17.32$ m. For the eight node cube and rectangular prism, the nodes are at their maximum difference in Euclidean distance from their true location when the nodes are the furthest radially from their centre, which is the far corner of the constraint cube at a distance of 17.32m. Taking a step towards a slightly more complex model with the sixteen node cube, the eight nodes at its corners have a maximum distance equal to 17.32m, but the other eight nodes, along eight of its edges, are at maximum a distance of $\sqrt{2 \times 10^2 + 0^2} \simeq 14.14$ m (Figure 3.18).

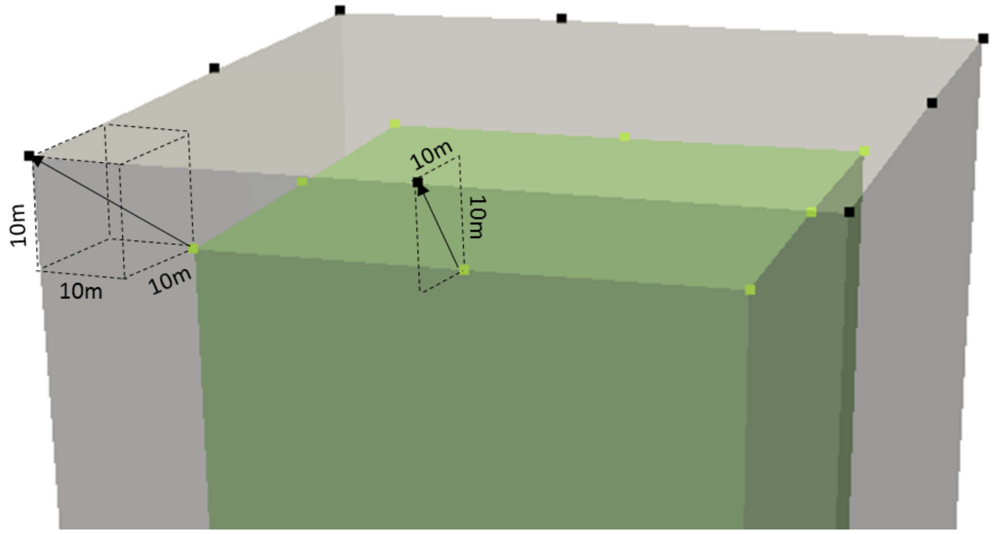

Figure 3.18: A comparison of the maximum distance between the nodes on the corners, versus the edge, of the inverted model and the true model. The true model is the green cube, and the gray cube the inverted model.

This results in an asymptote of $\frac{8\times17.32+8\times14.14}{16} \simeq 15.73$ m, as seen in Figure 3.17.

Due to this behaviour, the eight node cuboid measurements can be used to form an upper bound on the node positional uncertainty resulting from uncertainty in the physical property.

3.4.1 Uncertainty with Varying Constraints

The next step in the empirical testing of uncertainties was looking at the effects of changing the bounds on the nodes' position, which until this point were constant at 10 m in each Cartesian coordinate direction. It was found that for a model such as the eight node cube of dimensions $50\times50\times50$ m^3, an acceptably accurate inversion could not be produced when the nodes' bounds were 30 m or greater. Therefore, bounds below that at 5 m, 10 m, 15 m, and 20 m were used to demonstrate that given small physical property uncertainties ($\leq 40\%$), the bounds had no effect on the relationship between the node position uncertainty and the physical property uncertainty, Fig 3.19.

To create a function that can be used to approximate the uncertainty of the inverted model's nodes' position, a polynomial fit was applied to the data shown in Fig. 3.16. The function used to fit the data was

$$E(\sigma) = 1\times10^{-8}\sigma^5 - 1\times10^{-6}\sigma^4 - 5\times10^{-5}\sigma^3 + 5.1\times10^{-3}\sigma^2 + 4.5\times10^{-3}\sigma + 1.55, \quad (3.9)$$

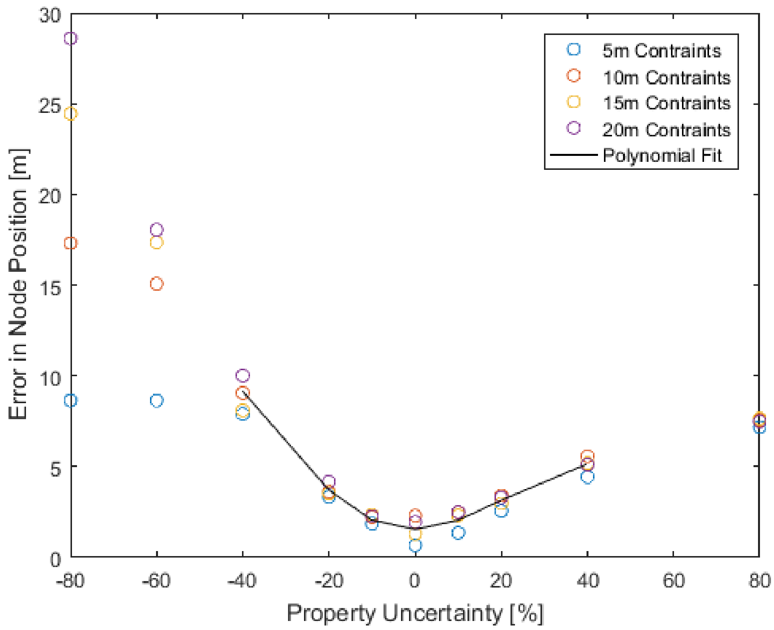

Figure 3.19: A plot displaying the error in node position vs. property uncertainty curves for inversion of the eight node cube performed with 5 m, 10 m, 15 m, and 20 m bounds. The solid black line is the polynomial fit applied to the mean of all the curves, between ±40% uncertainty.

as seen in Fig. 3.19, where σ is the magnetic susceptibility percent standard deviation.

3.5 Discussion

Before concluding, the assumptions and current limitations of the developed SGI algorithm are reviewed, as well as possible future extensions. First, while the provided examples have shown the effectiveness of the SGI algorithm to recover the ground truth with accurate prior information, more work is required to assess the effect of inaccurate prior information: for example, the physical properties assigned to each rock unit, and the topology allowed for by the initial model. Readers may wish to refer to the following works for more information regarding topological analysis: Caumon (2018) and references therein. Assuming physical properties and topology are prescribed accurately, the accuracy of the geometry of the initial model should not affect the final solution; this assumes the chosen global optimizer succeeds in finding an appropriate global minimum. However, the convergence of the global optimizer may still be affected, and there may be a chance that global minima exist (all with equal minimum objective value) which may complicate matters.

An assumption that we have made regarding physical properties is homogeneity. In contrast, the work of Fullagar et al. (2000), Auken and Christiansen (2004), De Pasquale et al. (2019a), De Pasquale et al. (2019b) and Zhang et al. (2015) all allow for varying levels of heterogeneity inside their models. Their methods can simultaneously invert for physical property distributions and surface geometry. Again, doing so increases the non-uniqueness of the inverse problem, and further work is required to assess when such methods can produce meaningful solutions. For any specific exploration question, it may be more appropriate to develop a workflow that combines voxel inversion methods, which recover physical property distributions, and surface-based inversion methods, which recover surface geometries, in ways to best leverage the advantages of each.

Another important assumption one should assess for any SGI is whether the problem is truly well-posed. We have assumed that an overdetermined problem, with more data measurements than model parameters, leads to a problem that is sufficiently well-posed that our SGI method can provide meaningful solutions. While we feel this is a reasonable assumption, it may not be true in general and requires further research. The extent to which these highly nonlinear problems are well-posed likely depends on the number of data, the tessellation of the surface-based models, the subdivision strategy, and the size and shape of the anomalous targets. These are difficult questions to address but should be in future work. General rules may be difficult to develop but some methodology to assess the stability of the problems should not be challenging to design.

We use stochastic sampling to calculate standard deviations on the vertex locations of the recovered surface-based models. The standard deviations can act as a proxy for confidence in the model features but we emphasize that this strategy may provide less useful estimates if we are sampling multi-modal distributions. More detailed or sophisticated statistical analyses may be helpful for providing more robust assessments of model confidence.

The ideal case for the SGI method was demonstrated in the first example, that of the single dipping prism. There, the initial model was designed with the same number of control nodes as the true model, allowing the possibility for a perfect inversion solution to be found. The fit was close, with a greater fit to the true model near surface, as expected from potential field modelling. Where the SGI model differs from the true model there is a corresponding increase in the uncertainty of the control nodes' positions, as visualized by the uncertainty spheres in Fig. 3.5.

The second example, the double prism, explored the ramifications of correctly or incorrectly assuming the topology of the true model in the initial surface model. Our SGI method at present can not change the topology of the inputted surfaces during the inversion process, so a likely uncertainty that will arise when dealing with real data sets is whether or not the correct topology was chosen. The double prism example was chosen mainly because it is unclear from its observed forward signal that there are definitively two separate anomalous bodies in the subsurface. To explore the effects of incorrectly assuming the topology of the surface model, a SGI was performed with the data from the double prism model using a single enclosed anomalous volume to represent both prisms. The results of which were compared to the control case where the correct double volume topology was used in the SGI, showing the use of an incorrect topology could still produce a model resembling the true two-anomaly model by thinning the segments between the anomalies.

In the last example, the synthetic SMS deposit, a more complicated system was modelled. The computational expense was reduced by removing fixed topographic nodes completely from the problem. To demonstrate the SGI's ability to provide smooth inversion models, if desired by prior information, a Cubic B-spline subdivision was implemented on the candidate models during the inversion. This allowed smoother features to be generated, while maintaining a low number of inversion parameters. This subdivision does increase the computational cost of the SGI, as the forward signal of each candidate model is calculated from the subdivided surface which contains an increased number of facets. With subdivision, smoother model features can be resolved, but without it there is a greater risk of sharp features appearing in the inversion model. Generally, if there is a lower confidence in one's initial surface model, i.e. smaller detailed features of the geophysical target are unknown, then it is more constructive to use subdivision and build smoother surface inversions.

Some questions remain relating to subdivision and parameter reduction. First, the amount of subdivision used in the examples has been fairly ad-hoc. For any given scenario, it is likely that the number of control nodes, and the amount of subdivision required, will be related to the specifics of that scenario, e.g. the geology involved and the exploration questions being asked. Hence, it is difficult for us to prescribe any general rules for best practices, and the choices must be determined on a case-by-case basis. There is plenty of flexibility to do so. Second, there are questions related to subdivision and how well-posed the inverse problem is (discussed above).

Third, if regularization were added to the problem, how it interacts with the subdivision choices is another avenue that could use more investigation.

The presented SGI method is designed to work with an input model built using explicit facetted surfaces because that is typically how geological models are provided. However, geological models may also be represented with parametric curves and surfaces (Roy et al., 2005), including implicit modelling methods such as Hillier et al. (2014), or they may be built using underlying control surfaces (e.g. Ruiu et al., 2016). One could think of developing an SGI approach that works directly with the parameters that control such surface model representations, as did Pereyra (1996), Rawlinson et al. (2001), and Rawlinson and Sambridge (2003). That requires one can either calculate the forward solution directly on the underlying model parameterization, which is not generally possible, or one can easily translate from the parameter space to an explicit surface on which the forward solution can be calculated. Pereyra (1996), Rawlinson et al. (2001) and Rawlinson and Sambridge (2003) managed the former using ray-tracing for their seismic travel-time tomography problems. Zhang et al. (2015) did the latter for their 2D problem involving a single interface surface. However, any model representation translation introduces additional computational overhead, similar to if an intermediate mesh were required to perform the forward calculation. From a practical perspective, if an explicit surface-based geological model is provided, one must be able to transform from that explicit surface representation to the implicit surface representation (or parametric curve or control surface parameters). That transform is generally not trivial and may represent an inverse problem itself. It is for that reason we have considered surface-subdivision, which can easily be applied directly to a coarse version of an explicit surface-based geological model.

For surface-subdivision, we used a Cubic B-Spline interpolation (see Peters and Reif, 2008) in the SMS example and to generate the images in Fig. 3.1. This approach leads to a subdivided interpolated surface that does not pass through the control nodes. An alternative is to use an interpolation that creates a surface that does pass through the control nodes, such as Dyn-Levin-Gregory interpolation (see Peters and Reif, 2008). Generally, Cubic B-Spline interpolation produces smoother surfaces, while Dyn-Levin-Gregory interpolation allows sharper (smaller curvature) features to remain after the subdivision. Hence, a priori information may suggest the use of one interpolation scheme over another. Other interpolation alternatives exist and may be more useful for particular scenarios, particularly if the input geological models are built using specific interpolation schemes, such as the 2D Gaussian process regression used in the work of Beardsmore et al. (2016) and Scalzo et al. (2019). Furthermore, as Rawlinson and Sambridge (2003) found for their SGI methods, the design of the control surface may have some effect on the convergence of the inversion, whether or not it can adequately recover the imaging target, and ultimately its effectiveness for answering any specific exploration questions regarding the target. Future work should investigate these aspects. A related question is whether, for specific SGI problems, some form of regularization might be more effective than use of surface-subdivision (e.g. Bijani et al., 2015). However, as mentioned previously, addition of regularization measures to the objective function complicates the inverse problem.

In the examples we only used geophysical data types that could be directly calculated on a surface-based model, without the requirement of an intermediate voxel discretization. This includes both gravity and magnetic data, but approaches may exist for other data types and should be investigated (e.g. Liu et al., 1999; Javaheri Koupaei, 2012). However, any data types that can be calculated using a voxel discretization could be implemented into our SGI provided a sufficient mesh generation algorithm is inserted: this would fit between the "Candidate model" and "Forward solver" components in Fig. 3.3 and would generate a mesh that is consistent with the candidate surface-based model. This could be a tetrahedral mesh, with tetrahedral faces lying exactly at the locations of the triangular facets in the input model. Alternatively, it could be a pixellated representation of the surface-based model built on a rectilinear mesh (regular, irregular, or octree). While the addition of a mesh generator into the SGI algorithm could significantly increase the solution time (a mesh must be generated for every candidate model), more critical is the issue of mesh quality. Many modelling methods, particularly for seismic and EM problems (see Lelièvre et al., 2011; Jahandari and Farquharson, 2014, 2017; Ansari and Farquharson, 2014; Ansari et al., 2017) require some measure of mesh quality, often related to sizes and aspect ratios of the mesh cells, to reduce the modelling errors. The required quality may not be achievable using automatic meshing options built inside an inversion code; a more hands-on, expert user-guided meshing may often be required, particularly when there are features of different spatial scales in the surface-based model. Nevertheless, future SGI research should attempt inversion of these more challenging geophysical data types.

In this work, the TTI methods of Möller (1997) were used, but we accept that more computationally efficient methods may exist for our SGI problems. Several authors have developed TTI algorithms (Guigue and Devillers, 2003; Tropp et al., 2006; Wei, 2014; Sabharwal and Leopold, 2015; Danaei et al., 2017), which have shown variable relative success on different types of problems.

To minimize the objective function we used a GA with choices for various operators based on Deb et al. (2002). More modern GA algorithms exist and there are many other flavours of global optimization, such as PSO, that could be applied to the problem. Future work could investigate the relative merits of various global optimizers for SGI problems. There are also some remaining questions regarding the existence of multiple minima in SGI problems: when they can be expected to exist, how bad the issue may be for particular scenarios, whether multiple global minima may exist, how they affect the behaviour of different global optimizers, and how they relate to noise in the measured data or any fundamental non-uniqueness in the inverse problem.

A major practical assumption that has yet to be discuss is the suitability of the input geological model for our SGI methods. It is required that surface-based models honour the requirements of valid PLCs (closed surfaces and specific rules regarding intersections). Ideally, geological models would be built to honour those requirements; after-all, those same requirements mirror what is geologically reasonable. However, this is not a common practice. Additionally, the quality of the tessellated surfaces in input geological models can be poor. This is often because such models are only used for visualization; even common quantitative methods used, to calculate rock unit volumes and perform geostatistical calculations, generally make translations from surface-based representations to regular rectilinear meshes. Regardless of the unstructured mesh generation algorithm used, poor quality tessellated surfaces lead to poor quality volumetric tetrahedral meshes. The issue of surface quality is not an immediate problem for modelling gravity or magnetic responses because the quality of the surface does not affect the accuracy of the modelling. However, if the quality of the input surfaces are improved then this can sometimes dramatically reduce the number of facets and the computation time of an SGI. When faced with these issues, we use the freely available software FacetModeller (Lelièvre et al., 2018) to perform the required manipulation of the input models. Admittedly, this manual procedure can be time consuming for complicated models and automated procedures would be preferred (e.g. Bonneau et al., 2018; Pellerin et al., 2014, 2017). We have made use of Autodesk Meshmixer (e.g. Autodesk, 2017), currently freely available, for improving the quality of surface-based models, although this still requires some manual input.

For resource exploration and other applications, one will probably be dealing with an input geological model with many more surface facets than in our SMS example. While the computational requirements of our SGI methods are significant, there are several considerations that may improve the situation in practice. Many global optimizers, including the GA we have used, are easily parallelizable. At each iteration of the GA, the calculation of the objective function and constraint violation for each individual candidate solution in the population can be performed independently. Moreover, each forward calculation may also be parallelizable, as is the case for the gravity and magnetic problems used in this paper: the response of each facet can be calculated independently. The intersection detection tests for a single candidate model can also be parallelized: the TTI test for each pair of facets in the model can be performed independently. While this is perhaps enough for those with access to large parallel computing platforms, other approaches may be helpful for reducing the computational requirements.

First, one can simply let the SGI work on specific parts of the model to which specific exploration questions relate. The other parts of the model then remain fixed, in a similar way to how the topography surface in the SMS example was fixed. If one removes the response of the fixed parts of the model from the geophysical data before inversion, then the fixed parts of the model do not need to be treated at all by the SGI: their response need not be calculated during the forward calculation. This would mean not only is the SGI working with a reduced set of control node parameters, and therefore the global optimization should require fewer iterations to find an appropriate solution, but also each forward modelling (for each candidate model) will be faster than if the entire volume of interest were used.

Second, one might consider a multi-stage procedure. In the first stage, a coarser surface-based model could be used, or some small subset of the observed data could be used, or both, provided the problem is still sufficiently well-posed. This provides a fast initial solution estimate that can be fed into the second stage, wherein the surface model is subdivided, or more observed data are used, or both. This iterative procedure can continue up to the desired model discretization, or number of observed data, with the hope that the overall computation time is less than simply running the final stage with the original initial model.

The SGI examples in this paper have been, for the most part, unconstrained. However, much prior information may be available to constrain an SGI, just as it is often available to constrain traditional voxel inversions. Bound constraints on model parameters are trivial to implement into GA and other global optimizers. If the SGI is run to allow the physical properties of each unit to change, petrophysical information can be incorporated into the SGI by placing bounds on the physical properties assigned to each rock unit. In a more rigorous stochastic sampling using MCMC, one could also incorporate petrophysical probability density information. Tie-points, locations where surfaces are known to pass through, can be incorporated trivially by including surface vertices at the tie-points which remain fixed during the inversion, or are bounded to move within some small region. Orientation information is perhaps more challenging to incorporate directly into the formulation described in our paper. Also, while our intersection detection methods can enforce some forms of topological rules, others may be more challenging to enforce, such as requiring that some units obey relative spatial positioning rules. However, one strength of SGI is that any mathematical regularization measure that can be translated into computer code can be used, with no requirement of differentiability. Hence, one can include regularization measures or topological constraint functions that are custom-built for particular imaging problems. Future work should investigate the incorporation of these and other forms of prior constraining information.

While the examples that we have presented have inverted single geophysical data types, extension of our SGI methods to joint inversion (simultaneous inversion of multiple geophysical data types) is trivial. For any joint inversion, one must develop some approach to encourage the compositional or structural similarity of the multiple physical property models considered. For voxel inversions, additional so-called coupling functionals can be incorporated into the objective function as additional terms or constraints: refer to Moorkamp et al. (2016) for a comprehensive discussion. However, for SGI, the structural coupling is built directly into the parameterization of the problem: the physical properties change across the interfaces in the surface-based model. Hence, inverting a single geophysical data type is practically no different from inverting multiple data types: all that is required is the additional petrophysical information for the relevant causative physical properties. Bijani et al. (2017) provides an example of an SGI joint inversion of gravity and seismic travel-time data.

3.6 Conclusion

This chapter presented a fundamentally different inversion method for recovering Earth models that better emphasize distinct rock units, and the contacts between them, than typical minimum-structure inversions. The advantage of the SGI approach is that the geological and geophysical models can be specified using the same parameterization: they are, in essence, the same Earth model.

A limitation of our SGI method is the requirement to define the subsurface into petrophysically homogeneous units. In many Earth systems this assumption is correct, but not all. Additionally, petrophysical data is needed to fix physical property values to each rock unit in the SGI model. Therefore, the SGI method is best fitted as a late stage exploration modelling tool which can build off preexisting Earth models.

Despite the computational challenges involved, methods for parallelization and parameter reduction can be applied to significantly limit computation times during SGI. This provides computationally feasible approaches for working with novel subsurface parameterizations that can produce Earth models more compatible with the way geologists typically think of the Earth's subsurface.

Chapter 4

Deposit Scale Hydrothermal Alteration Modelling; Trans-Atlantic Geotraverse Active Mound [1]

4.1 Introduction

Seafloor massive sulfide (SMS) deposits form at the seafloor at sites of high-temperature hydrothermal venting. These metal-rich deposits represent the modern equivalents of ancient volcanogenic massive sulfide (VMS) deposits, and serve as a potential future source for copper, gold, silver, zinc, and lead (Hannington et al., 2011). They form at or near the seafloor by the precipitation of sulfide minerals from metal-laden hydrothermal fluids, where the remote environment and hostile conditions make conventional deposit assessment methods such as drilling challenging and expensive.

The Trans-Atlantic Geotraverse (TAG) active mound is a hydrothermally active SMS deposit located on the hanging wall of a detachment fault at 26°08'N along the Mid-Atlantic Ridge (Fig.

[1] Galley, C.G., Lelièvre, P., Haroon, A., Graber, S., Jamieson, J.W., Szitkar, F., Yeo, I., Farquharson, C., Petersen, S. and Evans, R.L., 2021. Magnetic and Gravity Surface Geometry Inverse Modelling of the TAG Active Mound. Earth and Space Science Open Archive ESSOAr (accepted in the Journal of Geophysical Research: Solid Earth).

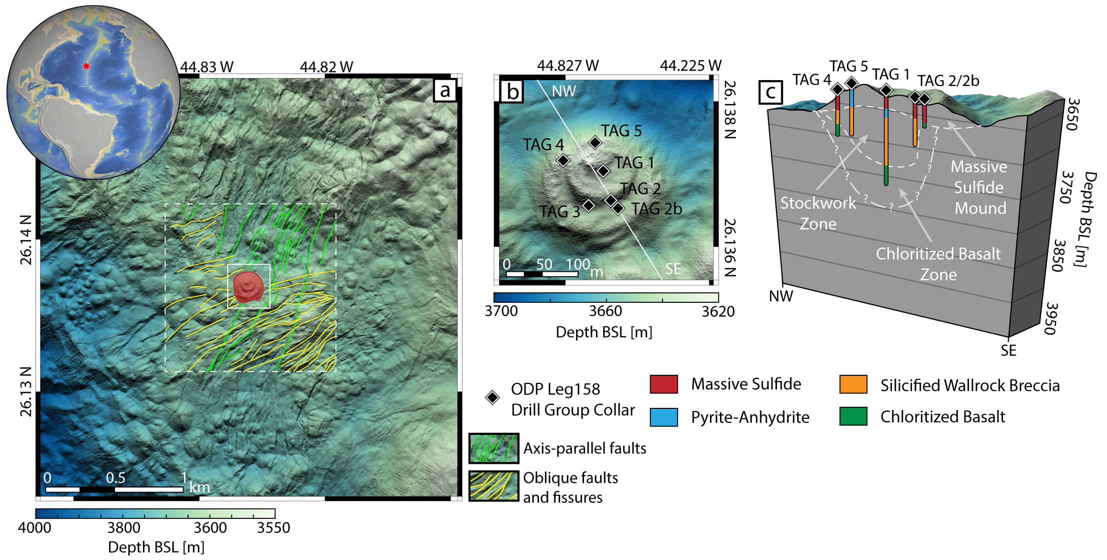

Figure 4.1: a) The bathymetry of the TAG mound. The regional inversion model's volume of interest is outlined with a dotted white line, the volume of interest for the deposit scale inversion is outlined by a solid white line, and the structural information is from Graber et al. (2020). b) Map of the TAG mound showing locations of the ODP Leg 158 boreholes and borehole lithology logs from Knott et al. (1998a) projected onto a NW/SE cross section. Bathymetric data with 2 m resolution was collected in 2016 using the GEOMAR AUV Abyss (Petersen, 2016).

4.1; Rona and Scott, 1993; Tivey et al., 2003). The TAG mound is composed primarily of massive sulfide and anhydrite (Petersen et al., 2000). Drilling of the active mound was conducted in 1994 as part of the Ocean Drilling Program (ODP) Leg 158, from which a mineralogical reconstruction of the active mound's massive sulfide and sulfate interior, silicified wallrock breccia, and chloritized basalt unit was created (Knott et al., 1998a; Smith and Humphris, 1998). The deposit's outer most subseafloor alteration unit, the chloritized basalt, was intersected by three of the Leg 158 boreholes (TAG 1, 2b, and 4), but those boreholes did not penetrate deep enough to intersect the contact between the chloritized basalt and unaltered basalt. This chloritization of the seafloor is an alteration process that occurs as a result of the rising hydrothermal fluids mixing with the more magnesium rich local seawater at $> 200^{\circ}$C (Galley and Koski, 1999; Humphris et al., 1998; Seyfried and Bischoff, 1981). Information regarding the depth and scale of the local seawater circulation into the TAG hydrothermal system could be derived from the geometry and size of the chloritized basalt unit.

The rising hydrothermal fluids and their associated seafloor alteration have multiple effects on the physical properties of the crust. The hydrothermal fluids increase the rate of alteration of the titanomagnetite within the basalt to the less magnetic titanomaghemite, as well as increasing the rate of titanium dissolution from the titanomagnetites, making SMS deposits low magnetic anomalies both at the seafloor and deep into the crust (see Section 1.2.2). On the deposit scale all lithologic zones (i.e. massive sulfide mound and the stockwork zone; Fig. 4.1c) within the chloritized basalt unit contain the lowest magnetic properties (Wang et al., 2020), with a secondary low extending down the length of the hydrothermal fluid upflow zone (Galley et al., 2020). Despite the TAG mound being a homogeneous magnetic low, its massive sulfide mound unit can be distinguished from the other units by its anomalously high density (Evans, 1996; Ludwig et al., 1998), caused by its primary composition of massive sulfide (with a density of approximately 3.65 g/cm^3 compared to 2.4 g/cm^3 for basalt; Evans 1996).

Investigations of the subseafloor structure of SMS deposits have been mainly driven by drilling. The sparse drilling at the TAG active mound has provided key information on the geometry (Humphris et al., 1998) and genesis of SMS and VMS deposits (You and Bickle, 1998), and has led to the TAG active mound model being widely used as a representative for a generic SMS deposit (Galley et al., 2007). However, the geological interpretation of the TAG active mound was primarily two-dimensional (2D), with only one borehole (TAG 1) extending deep (approximately 120 m) into the deposit's core (Knott et al., 1998a). The overall drilling was therefore not deep enough to determine the thickness of the chloritized basalt unit that underlies the silicified wallrock breccia zone, as the drillholes did not intersect the interface between chloritized and unaltered basalt. Additionally, to estimate the mound's sulfide mineral tonnage, symmetry was assumed orthogonal to the 2D geologic interpretation (Hannington et al., 1998). This chapter expands on previous knowledge of the geometry of subseafloor SMS hydrothermal alteration units by inverting for a 3D geophysical model of the chloritized basalt unit, as well as a 3D model of the deposit.

The two most commonly used methods for modelling magnetic data from SMS deposits are those of Parker and Huestis (1974) and Honsho et al. (2013), which both solve for a magnetization distribution. The distribution varies laterally, with no vertical changes and a fixed thickness to the magnetized crustal layer, typically 500 m (Szitkar and Dyment, 2015), but the thickness has also been defined by the Curie isotherm depth (Bouligand et al., 2020). Minimum-structure inverse modelling can be an effective alternative method to model the variations in physical properties around and within SMS deposits (Kowalczyk, 2011; Caratori Tontini et al., 2012; Galley et al., 2020). This modelling method uses a three-dimensional discretization of the crust, known as a mesh, and solves for the target physical property values inside each of the mesh's cells.

Minimum-structure inverse modelling is robust, requiring little prior knowledge of the subsurface to construct a feasible geophysical model (Constable et al., 1987a). Here, the minimum-structure inverse modelling uses the method as described in Section 1.5, which discretizes the crust using a tetrahedral mesh as to closely fit the variable bathymetry and solves for the effective magnetic susceptibility in each tetrahedral cell.

Minimum-structure inverse models are smooth by design and as such can have difficulty determining the locations of discrete or almost discrete boundaries between petrophysically contrasting lithological units. To further improve upon a subsurface physical property model, a surface geometry inversion (SGI) method can be used to solve for a wireframe model of an SMS deposit (see Chapter 3). Our SGI method creates a wireframe surface model of rock unit contacts by inverting for the 3D position of the vertices that define the surface mesh. This is accomplished using first a Genetic Algorithm (GA) to find the model that best fits the data, followed by a Markov chain Monte-Carlo (MCMC) to calculate the model's uncertainty. Modelling SMS deposits as wireframe models creates geophysical models that are formatted similar to geological interpretations and allow for the volumes of alteration units to be easily calculated.

Previous geophysical models of the TAG active mound have included inverting magnetic data to study the lateral variations in magnetization at the deposit (Szitkar and Dyment, 2015; Tivey et al., 1993), as well as inverting controlled-source electromagnetic (CSEM) data to develop 2D conductivity cross-sections through the TAG mound (Gehrmann et al., 2019). The magnetization models have led to the lateral extents of the near-surface hydrothermal alteration being mapped, allowing the deposit to be identified as a low magnetization anomaly that extends into the seafloor; however the models did not identify the vertical variations in the deposit's alteration. Gehrmann et al. (2019)'s CSEM inversions included two ≈ 100 m thick cross-sectional models that passed orthogonally through the TAG active mound, allowing the high conductivity regions associated with massive sulfide mineralization to be identified. The relatively shallow depth of penetration of these CSEM models allows them to map the conductivity anomalies in the upper alteration units of the mound, but the smooth nature of the minimum-structure inversion models limits the model resolution and creates difficulties when trying to identify the thickness of the zone of mineralization.

With the incorporation of the Leg 158 drilling information, AUV magnetic data collected during the 2016 RV Meteor M127 cruise (Petersen, 2016) and seafloor gravity data collected in the Shinkai 6500 submersible (Evans, 1993), minimum-structure and SGI models are used to develop a new three-dimensional geological model of the TAG active mound system. This model relies on two steps: 1) modelling of the effective magnetic susceptibility distribution around and within the TAG active mound using minimum-structure inverse modelling; 2) modelling the discrete contact boundaries between the deposit and surrounding basalt host rock using magnetic and gravity SGI. This chapter's modelling has developed, to the best of our knowledge, the first 3D model of the TAG mound derived from geophysical data, an improved sulfide tonnage estimate evaluation for the deposit, and a better understanding of the deposit-scale hydrothermal fluid circulation.

4.2 Inversion Methods

Two modelling methods were used in this study, the minimum-structure inverse modelling method and the SGI method. Both solve for the shape of an anomalous geophysical anomaly in the crust but do so in two fundamentally different ways.

4.2.1 Minimum-structure inverse modelling

The minimum-structure inversion method is arguably the most common inverse modelling method used in geophysical studies (Farquharson and Lelièvre, 2017). The method solves for a smooth distribution of the target physical property in the subsurface, generating a blurred but robust Earth system model. A cell-based mesh is used during minimum-structure inversions, which discretizes the subsurface into a large number of pixels that each contain a homogeneous physical property value. In our modelling we use a tetrahedral discretization for all the inversions' meshes, as these unstructured meshes allow for very accurate representation of variable topography on the surface of the mesh as well as being able to efficiently incorporate zones of high and low cell compactness (Lelièvre et al., 2012). To construct our meshes we use the program *Triangle* (Shewchuk, 1996) to develop a 2D Delaunay triangular surface to represent the bathymetric surface. The program *Tetgen* (Si, 2015) is then used to fill the 3D volume below the bathymetric surface with tetrahedra.

The minimum-structure inversion approach used here considers an objective function containing an L2 norm data misfit and model measure, as well as a sensitivity weighting (see Section

1.5).

4.2.2 Surface Geometry Inverse Modelling

The second inversion method used in this chapter was the SGI method (see Chapter 3). Rather than solving for the physical properties in a number of cells, the SGI method holds the physical property values in a number of geometric bodies constant and alters the shape of the body or bodies until it sufficiently fits the observed geophysical data. Each of these anomalous bodies are parameterized by a triangular surface mesh, defining the discrete contact between differing geologic units. As such, the inversion method is parameterized by the 3D Cartesian coordinates of each vertex that defines the wireframe surface mesh. This parameterization often leaves the inverse problem over-determined, reducing the non-uniqueness of the problem compared to the under-determined minimum-structure method. Okabe (1979)'s forward algorithm was also used by this inversion program.

The topology of the SGI's wireframe surface mesh is not able to vary throughout the inversion, and as such its initial design holds some weight on how close of a data fit will be possible. To construct the initial wireframe surface meshes the program *FacetModeller* was used (Lelièvre et al., 2018), which allowed the user to place the defining vertices in 3D space and govern their connectivity through manual placement of the surface's triangular facets. As such, it is simple to incorporate any prior geologic information in the surface mesh, i.e. location of rock unit contacts derived from borehole samples.

A GA was used to minimize the inversion's objective function, which is simply the data misfit, as the method's spatial parameterization has the possibility to add local minima to the solution space. After a best fit model is found from the GA a MCMC sampling is used to derive a model uncertainty and a mean inversion model.

An assumption that has been made in the developed SGI method's design is that the physical properties of each rock unit in the model remained fixed during the inversion. It is trivial to allow those physical properties to change as well as the surface geometry parameters (control node coordinates) by adding the physical properties of each homogeneous model region to the model parameter vector. Doing so will increase the non-uniqueness of the inverse problem such that a meaningful inversion result couldn't be found. Rather than solving for physical property values during the inversion modelling, a suite of inversion models could be produced with different prescribed physical property values, and these models could then be assessed relative to a priori information, such as drilling information, to determine the ideal physical property values needed to produce the best model.

4.3 Data

The bathymetric and magnetic data used in this study were collected during the 2016 R/V Meteor M127 cruise (Petersen, 2016). The gravity data were collected during the 1994 R/V Yokosuka MODE'94 cruise.

The M127's GEOMAR AUV Abyss AUV collected both bathymetric and magnetic data simultaneously. Near the TAG mound the AUV was flown at an altitude of 80 m, a speed of 3 knots, and a line spacing of 80-100 m.

4.3.1 Bathymetric Data

The bathymetric data were collected during the 2016 R/V Meteor M127 cruise using GEOMAR AUV Abyss, equipped with a RESON Seabat 7125 multibeam echosounder. The echosounder used a frequency of 200 kHz. The surveys were flown at a speed of 3 knots and line spacing of 80-100 m, resulting in a 2 m resolution bathymetric data set (Petersen, 2016). The bathymetric data was merged with MB Systems based on the location of prominent seafloor features, including the re-entry cone placed on the TAG mound during the 1994 ODP drilling that was visible in the high-resolution data. Erroneous soundings were removed using QPS Qimera. From the original dataset a 3 by 3 km^2 region centered on the TAG active mound was used in this study (Fig. 4.1a).

4.3.2 Magnetic Data

During the M127 cruise Abyss was equipped with an Applied Physics System APS 1540 Digital 3-Axis Miniature Fluxgate Magnetometer, which collected measurements at a 10 Hz sampling rate. The magnetic data set was cropped to only include measurements within the 1.2$\times$1.2 km^2 region centered on the TAG active mound (Fig. 4.2a). The magnetic data set was processed to remove the induced and permanent magnetization effects from the AUV by conducting a figure-eight calibration dive with the AUV/magnetometer and using that data set to solve for

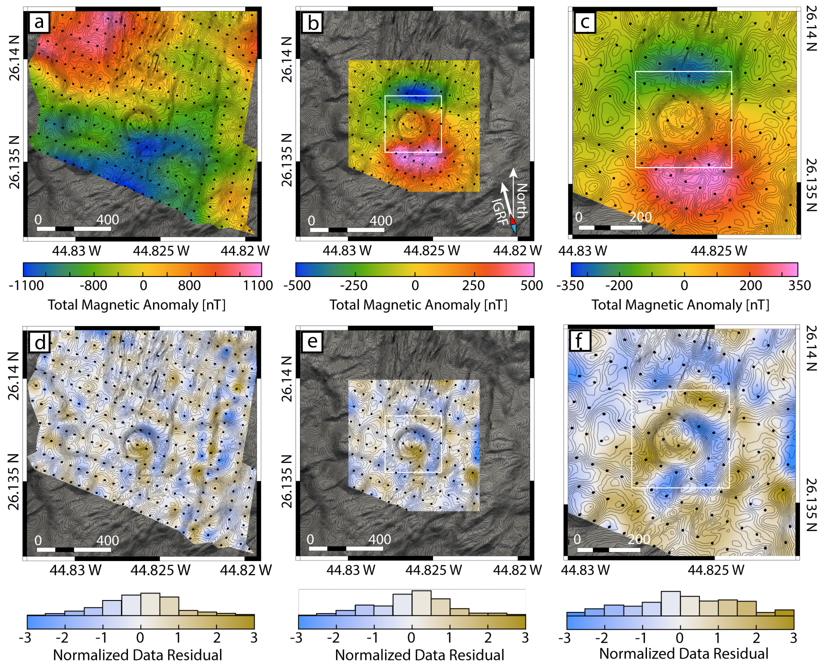

Figure 4.2: Processed data used in the magnetic inverse modelling of the TAG mound. a) The total magnetic anomaly data measured during the RV Meteor M127 cruise, used in the regional minimum-structure inverse modelling; b) the regional-removed magnetic anomaly data used in the deposit-scale minimum-structure inverse modelling; c) the regional-removed and filtered magnetic anomaly data using in the SGI; the normalized residual data from the deposit-scale minimum-structure inversion; and d-f) the respective normalized data residual from the inverted data a-c, with accompanying histograms of the normalized data residual values at each observation point. In b, c, e, and f the white outline represents the extent of the deposit-scale mesh. In all images the locations of the observation points are shown as black dots and 5 m bathymetric contour lines are shown in black.

the AUV's magnetic properties with a least-squares method (Honsho et al., 2013). The magnetic data was also low-pass filtered to 0.25 Hz to remove very short wavelength features associated with noise and the AUV propeller. The data set was then down-sampled to a point every 50 m along the survey lines to make the inverse modelling more efficient. The 50 m down-sampling was done while not producing any aliasing artifacts. The data were collected at an average altitude of 84 m.

The magnetic data's noise is an unknown in this study. The magnetometer has very low system noise (quantified at 0.5 nT), but the uncertainty in the observation points' lateral positions creates a larger, secondary noise. In comparison, the vertical position of the AUV, determined from altimeter and depth readings collected while surveying, is more precise. The AUV's lateral position is tracked from an initial calibrated position using an inertial navigation system. Ideally, this would be able to accurately locate the position of the AUV throughout its surveying, but any seafloor currents will gradually shift it away from its inferred position. An 8% relative noise

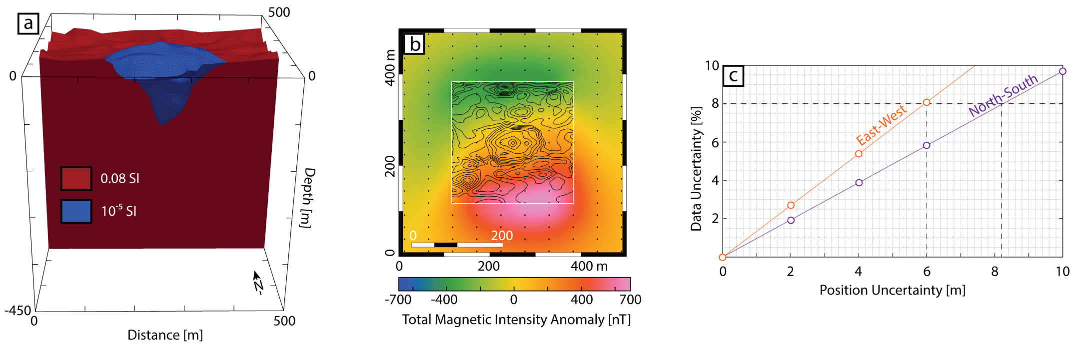

Figure 4.3: The synthetic model testing used to calculate the data uncertainty produced from an uncertainty in the observation point positioning. a) The synthetic SMS model with a 200 by 150 by 150 m 10^{-5} SI anomaly in a 0.08 SI background with topography. b) The 80 m altitude total magnetic intensity anomaly data with the outline of the synthetic model in white and the topography as black 10 m contours. c) A graph showing the linear relationship between the uncertainty in an observation point's position and the data's percent uncertainty. The two plots in c) represent uncertainty in the East-West directions versus the North-South directions.

was determined for the data, derived by adjusting how closely the study's minimum-structure inversion models could fit the data without producing artifacts. This noise would be equivalent to a 6-8 m uncertainty in the AUV's lateral position, likely caused by a current adding a constant velocity to the AUV's flight compounding the uncertainty in its position as measured with accelerometers (Fig. 4.3).

The percent uncertainty in Fig. 4.3 was calculated as a function of a normalized data misfit,

$$\chi_m^2 = \frac{1}{N}\sum_{i=1}^{N}\left(d_i(x,y,z) - d_i(x+a, y+b, z)\right)^2 \tag{4.1}$$

where the difference in the data responses comes from a lateral translation in the observation points by a in the x-direction and b in the y-direction.

For an inversion with an unknown uncertainty in the lateral position of the observation points, this uncertainty can be approximated taking the chi-squared form of the normalized data misfit,

$$\chi^2 = \frac{1}{N}\sum_{i=1}^{N}\frac{(d_{i,pred} - d_{i,obs})^2}{\sigma_i^2} \tag{4.2}$$

setting the data uncertainty, σ, to 1 in the program, resulting in

$$\chi^2 = \frac{1}{N}\sum_{i=1}^{N}(d_{i,pred} - d_{i,obs})^2 \tag{4.3}$$

and steadily increasing the fit of the data, χ^2, until data over-fitting artifacts in the resulting inversion model disappear. Setting the assumed uncertainty to 1 allows for the data's uncertainty to be approximated, since in the ideal case that the data's "true" noise is known and accurately included into Eq. 4.2 then the expected fit will be $\chi^2 = 1$. If the proper data misfit is found with Eq. 4.3, then it can be rearranged to

$$1 = \frac{1}{N}\sum_{i=1}^{N}\frac{(d_{i,pred} - d_{i,obs})^2}{\chi^2}, \tag{4.4}$$

meaning that if the data uncertainty is Gaussian and constant for each measurement then χ^2 will approximately equate to σ^2.

The resulting χ^2 value found through the inversion modelling can then be compared to the calculated χ^2_m values from a synthetic deposit of equivalent geometry to approximate the average lateral difference in the observation locations as determined from survey post-processing compared to their unknown "true" position above the seafloor,

$$\begin{aligned}\sigma^2 = \chi^2 &= \frac{1}{N}\sum_{i=1}^{N}(d_{i,pred} - d_{i,obs})^2 \\ &= \frac{1}{N}\sum_{i=1}^{N}(d_i(x,y,z) - d_i(x+a, y+b, z))^2 .\end{aligned} \tag{4.5}$$

The synthetic SMS deposit designed to be similar to the TAG mound, as shown in Fig. 4.3a, was created to calculate the data uncertainty as a function of lateral position uncertainty in the measured real magnetic data. The synthetic model consists of an approximately 150 by 200 by 150 m^3 10^{-5} SI mound and stockwork hosted in a 0.08 SI background. The background has the dimensions of a 500 by 500 by 450 m^3 block, representing a segment of the seafloor after a regional-removal has been performed (Li and Oldenburg, 1998b). The "true" data set $\mathbf{d}(\mathbf{x}, \mathbf{y}, \mathbf{z})$ was calculated as the forward signal of the synthetic model, with no noise, and the laterally uncertain data set was kept at the same altitude as the "true" data, but would have its lateral position shifted either in the East-West or North-South direction before calculating its forward signal. The asymmetry in the position uncertainty in the East-West versus North-South directions is attributed to the asymmetry in the total magnetic intensity of the anomaly induced from a non-vertical field. The same geomagnetic field strength, inclination and declination from the TAG active mound observed at the time of the magnetic survey was used in the synthetic modelling. As the results (Fig. 4.3c) show, there is a linear relationship between the uncertainty in the observation point's lateral position, $d_i(x, y, z) - d_i(x+a, y+b, z)$, and the data's uncertainty, σ.

4.3.3 Gravity Data

The data set from the gravity survey collected over the TAG active mound was composed of 11 stations roughly aligned along a North-South line crossing the mound (Fig. 4.4a,b), collected during the MODE'94 cruise. The measurements were collected manually from the Shinkai 6500 submersible on the seafloor with a Scintrex CG-3 autograv gravimeter (Evans, 1996). The data was first levelled using the northern-most station as a reference point, then processed to develop the free-water anomaly (see Section 1.4) The forward signal of a background model built with 2 m resolution bathymetric data of the seafloor about the mound, with density 2.4 g/cm^3 (Evans, 1996), was then removed to produce the Bouguer anomaly data. The 2 m resolution bathymetric data did not extend sufficiently far away from the observation points, so the linear trend left in the Bouguer anomaly data was calculated with a least-squares method and removed. The gravity data's noise was derived from the system noise of the gravimeter, as well as the compounding uncertainties associated with the data processing (Fig. 4.4).

4.4 Modelling Methodology

4.4.1 Magnetic Inverse Modelling

Two minimum-structure inversion models were constructed to produce first-pass three-dimensional magnetic susceptibility distributions that fit the observed data (Fig. 4.2a). Firstly, a regional minimum-structure model was produced (Fig. 4.5a), from which we could determine the volume of seafloor that completely encompasses the magnetic low representing the hydrothermal alteration associated with the deposit. The magnetic inversion methods we used assume that the induced magnetic fields in the subsurface are parallel to the geomagnetic reference field, allowing the method to solve for the scalar effective magnetic susceptibility. To rule out the presence of remanent magnetization that might perturb the magnetization vectors in the crust away from the Earth's inducing field a total magnetization vector inversion (TMVI) model was constructed to access the variance in the inclination and declination of the magnetization vectors in the mesh's cells.

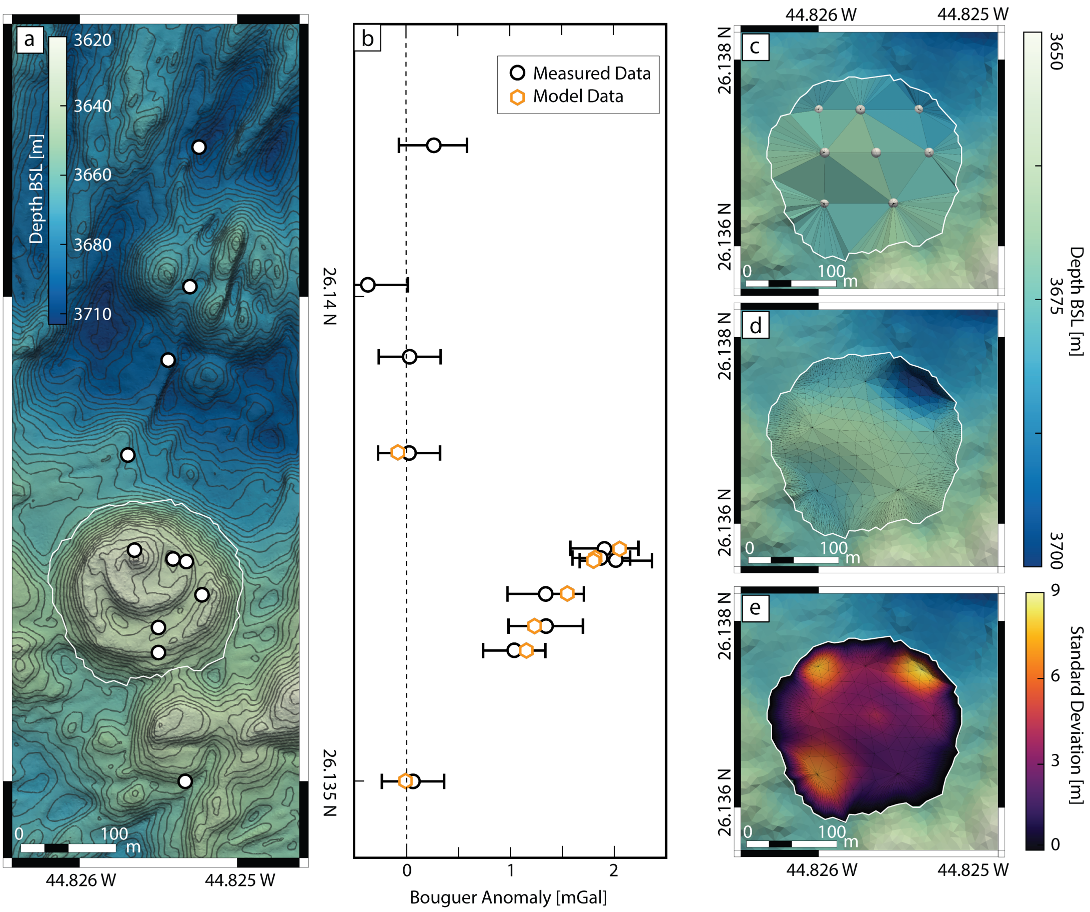

Figure 4.4: The gravity data collected over the TAG active mound as well as its SGI model. a) The locations of the gravity measurement stations are shown on the bathymetric map; b) a plot displaying the measured Bouguer anomaly data (black circles) compared to the data resulting from the SGI (orange hexagons); c) the initial model for the massive sulfide layer shown relative to the surrounding bathymetry; d) the SGI result relative to the surrounding bathymetry; and e) the SGI model coloured based off the standard deviation of the vertical position of the surface model. The black contour lines in a) mark 5 m intervals in depth and the error bars in b) signify the magnitude of the data's standard deviation.

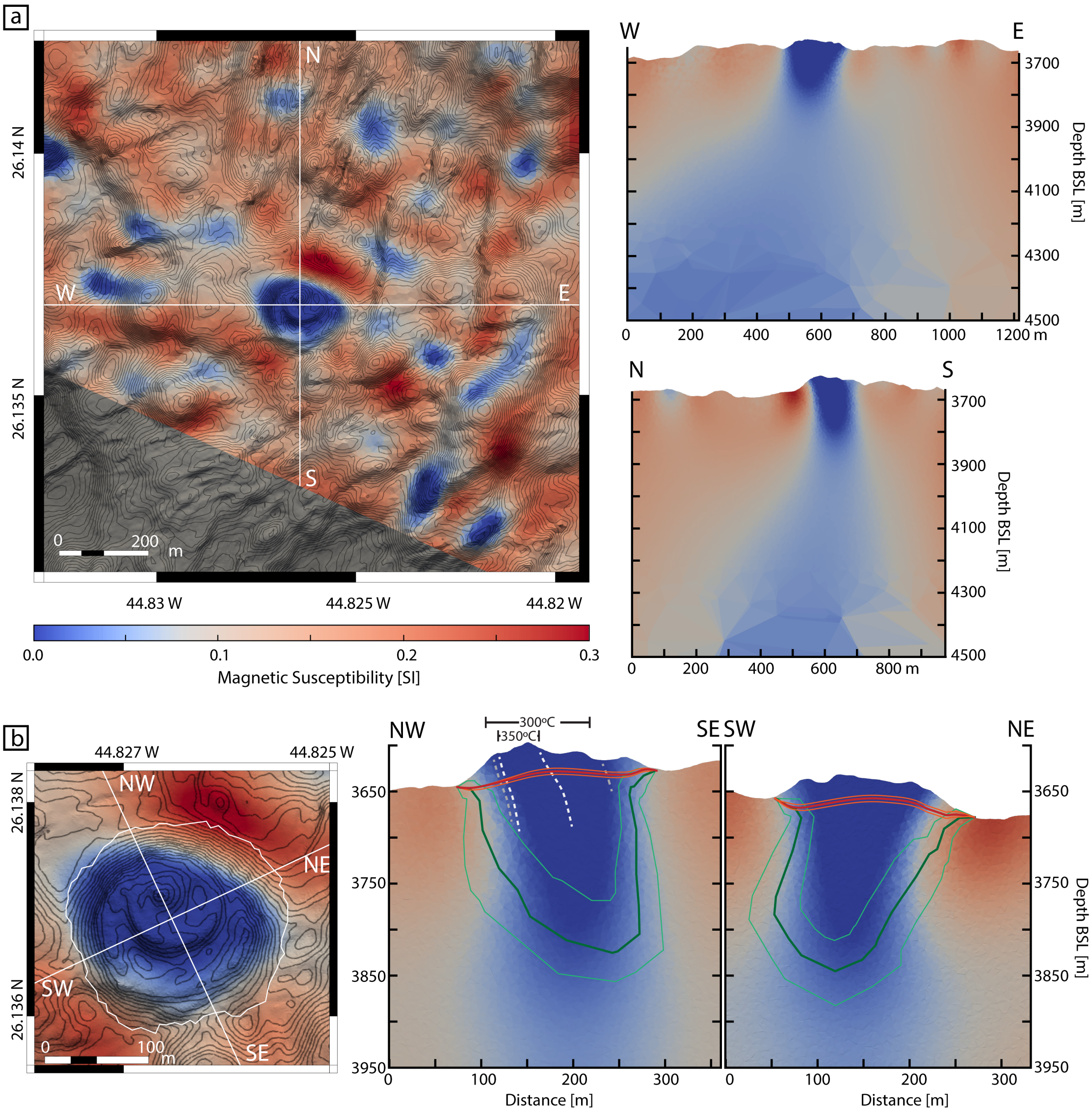

Figure 4.5: The minimum-structure susceptibility inversion results from the regional and deposit-scale models. a) The regional model shown in plan view and West-East and North-South cross sections; b) the deposit scale minimum-structure model. The mean surface for the chloritized basalt SGI is shown in dark green, and the base of the massive sulfide SGI layer in red. The one standard deviation shifted models are shown in light green for the chloritized basalt model, and orange for the massive sulfide model. Bathymetric contour lines (5 m interval) are shown in black. In the deposit-scale cross sections isotherms are overlain to compare with the geometry of the magnetic low anomaly (Grant et al., 2018).

The TMVI method used was that of Lelièvre and Oldenburg (2009), but adapted to be compatible with tetrahedral meshes. Of the two inversion options available to the method (i.e. inverting with Cartesian or spherical coordinate systems) spherical coordinates were used as to more easily constrain the inclination and declination of the model's magnetization vectors. The TMVI's initial model was a homogeneous model of 0.1 SI with magnetizations in the direction of the Earth's inducing field, with the inversion constraints being [0.0, 1.0] SI for the effective magnetic susceptibility, [10, 42]° for the inclination, and [-15, 0.0]° for the declination. The TMVI used the same tetrahedral mesh as was used for the scalar effective magnetic susceptibility.

To properly weight the three properties being inverted (i.e. effective magnetic susceptibility, inclination, and declination) a parameter γ is introduced to the model objective function,

$$\phi_m = \|\boldsymbol{W}_r \left(r - r_{ref}\right)\|^2 + \gamma\|\boldsymbol{W}_\varphi \left(\varphi - \varphi_{ref}\right)\|^2 + \gamma\|\boldsymbol{W}_\theta \left(\theta - \theta_{ref}\right)\|^2 \tag{4.6}$$

where $\boldsymbol{W}_r$, $\boldsymbol{W}_\varphi$, and $\boldsymbol{W}_\theta$ are the smoothness terms for the magnitude, inclination, and declination of the magnetization vector, respectively. r_{ref}, φ_{ref}, and θ_{ref} correspond to the reference model parameters, which were zero during our TMVIs, and the weighting parameter γ was assigned a value of 10^{-3} for the inversion. The weighting parameter was chosen to bring the values of the effective magnetic susceptibility and angles to the same order of magnitude as to balance their smoothing.

The TMVI model is displayed in Fig. 4.6, showing the difference in magnitude of the magnetization component parallel to the IGRF compared to the orthogonal component.

Further information is gained by analyzing the histograms of the inversion variables of the TMVI model's volume of interest (excluding the padding cells), as seen in Fig. 4.7. Fig. 4.7a shows that the prominent magnetization direction has an inclination of 42° but with another peak at 39°, and an inclination of -15° . This is compared to the IGRF vector whose inclination is 42° and declination is -15° . By studying the spatial distribution of the two magnetization components in Fig. 4.6 it appears that the magnitude of any remanent magnetization orthogonal to the IGRF's direction is much smaller than the parallel component, and that the zones of high orthogonal magnetization are very shallow and do not follow any known variations in geologic units in the crust. Therefore, it is most likely that the variations from the vector direction of the IGRF is a result of the program overfitting the data using more variables than are necessary

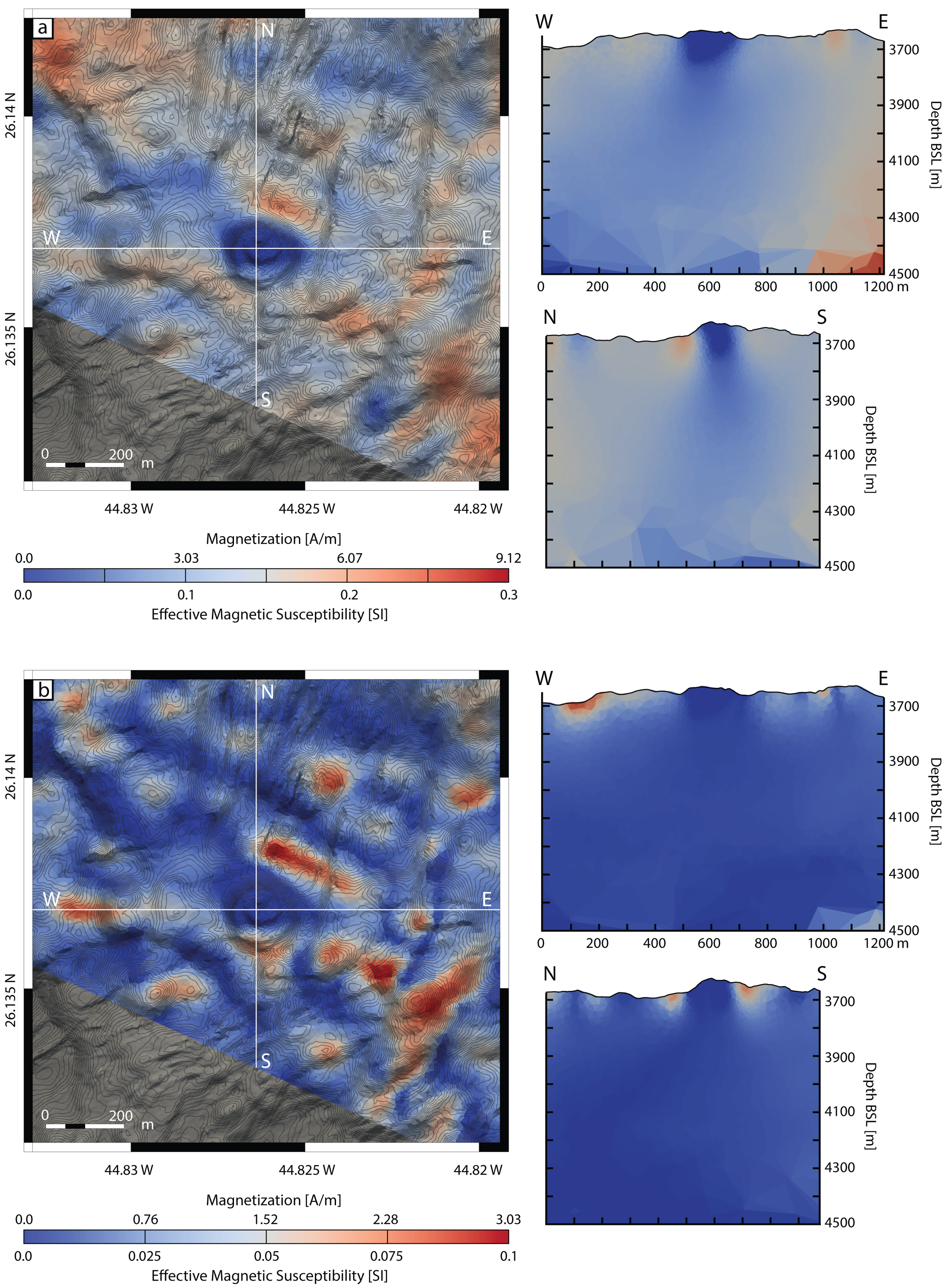

Figure 4.6: The results of the total magnetization vector inversion with the model displayed as a) the component of the magnetization parallel to the IGRF and b) the component perpendicular to the IGRF direction. Each component is displayed in plan view with two North-South and East-West cross-sections. Note the different colourbar scales.

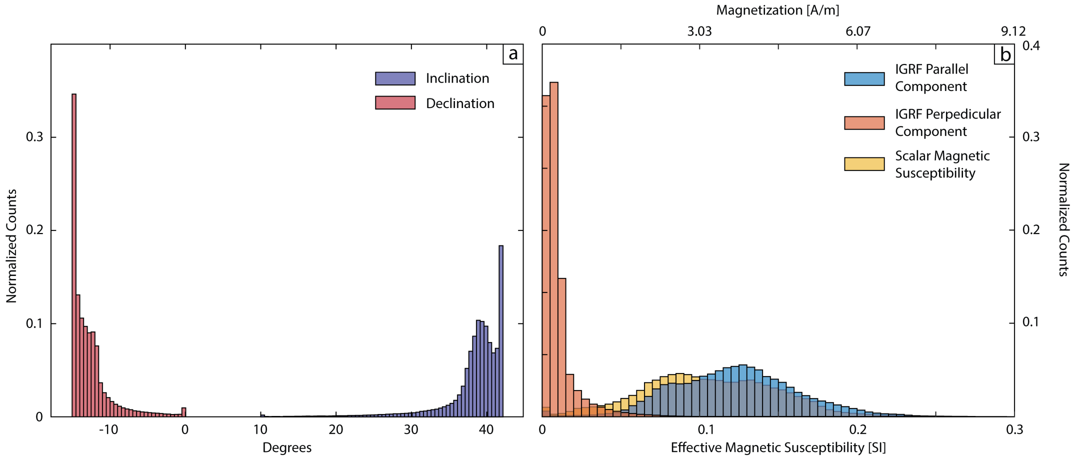

Figure 4.7: Two histograms showing the distributions of the total magnetization vector inversion model's variables within the model's volume of interest. a) shows the distributions of the model's cells' inclination and declination, with the declination's peak at -15° and the inclination's at 42° with a minor peak at 39°. b) shows the distributions of the magnetization components both parallel and perpendicular to the IGRF's direction, along with the distribution of the magnetization from the scalar effective magnetic susceptibility inversion.

(counter to Occam's Razor).

To perform small-scale modelling of the TAG mound, a regional data removal was done to isolate a 300 by 300 by 300 m^3 volume enclosing the mound (Li and Oldenburg, 1998b, Fig. 4.8). The regionally removed dataset was produced by creating a second regional inversion model that overfitted the magnetic data assuming a 0.3% noise. Over-fitting the data during the regional-removal process is key to ensuring that the remaining magnetic signal comes solely from the isolated volume. After isolating the volume of seafloor directly around the TAG active mound, the forward signal from the remainder of the model could be calculated and subtracted from the observed magnetic data to isolate the magnetic signature of the deposit (Fig. 4.2b; Li and Oldenburg 1998b). With the derived regional removed data, a second inversion model could be produced with a much greater cell compactness (608,134 cells within a 300 by 300 by 330 m^3 volume, versus 443,749 cells within a 3 by 3 by 1.8 km^3 volume) and higher bathymetric surface resolution (an average triangular facet area of 2.7 m^2 versus 50 m^2), creating a more accurate minimum-structure inversion model of the TAG active mound (Fig. 4.5b). The deposit-scale inversion was produced assuming the derived 8% noise in the data. Comparing the magnetic features between the regional and deposit-scale inversion models affirms that the regional removal did not subtract any data features that correspond to magnetic features in the isolated volume (Fig. 4.5). The regional inversion took 25 iterations and 4.1 hours to complete, and the deposit-scale inversion took 24 iterations and 45 minutes. Each inversion was run in parallel on 48 threads on a 2.20 GHz Intel Xeon E5-2650 Processor.

Next, an additional processing procedure was applied to further refine the magnetic data near the TAG active mound in preparation for the SGI. Ideally, when constructing surface models of the subsurface one would want a homogeneous background with the single anomalous body contained within it. However, the crust directly adjacent to the TAG active mound is inhomogeneous, containing zones of anomalously high magnetic susceptibility near the seafloor (Fig. 4.4b). To remove the components of the magnetic data that correspond to the anomalously high regions, a five step workflow was developed (Fig. 4.9): 1) invert the data derived from the regional removal; 2) isolate the cells that contain magnetic susceptibilities above the observed background value in the regional inversion model (in this case 0.08 SI; Fig. 4.4b), subtract the background value from the magnetic susceptibilities in the isolated cells to get anomalous susceptibilities relative to the background (0.08 SI); 3) calculate the forward signal from the isolated cells derived from step 2; 4) subtract the isolated cells' forward signal from the regional-removed data; and 5) invert the resulting data set to create a magnetic susceptibility model effectively free of anomalously high magnetic susceptibility regions.

The background value of 0.08 SI was chosen from the distribution of magnetic susceptibilities in the regional-removed model. As seen in Fig. 4.10, there are 2 major peaks in the histograms, one at about 0.0 SI representing the anomalously low magnetic susceptibility of the TAG active mound, and the second representing the background. The curve representing the model's background magnetic susceptibility in the regional-removed model is wide, with an approximate center at 0.08 SI. After further processing the data by removing the signal components related to the high magnetic susceptibility region (Fig. 4.9), the filtered model distribution develops a more prominent mean at the 0.07-0.075 SI bin (Fig. 4.10). Fitting a normal distribution to the background susceptibility values in the filtered model results in an approximate distribution with mean 0.07 SI and 0.01 SI standard deviation.

An SGI can now be performed on the resulting filtered data (Fig. 4.2c) to model the TAG active mound as an anomalous low inside an approximately homogeneous background. The first step in the SGI is to design an initial model for the inversion. Spatial bounds are then applied to the model vertices to develop an initialization volume. The initialization volume is defined as the volume of space that the solution model is assumed to exists in, and acts as the search

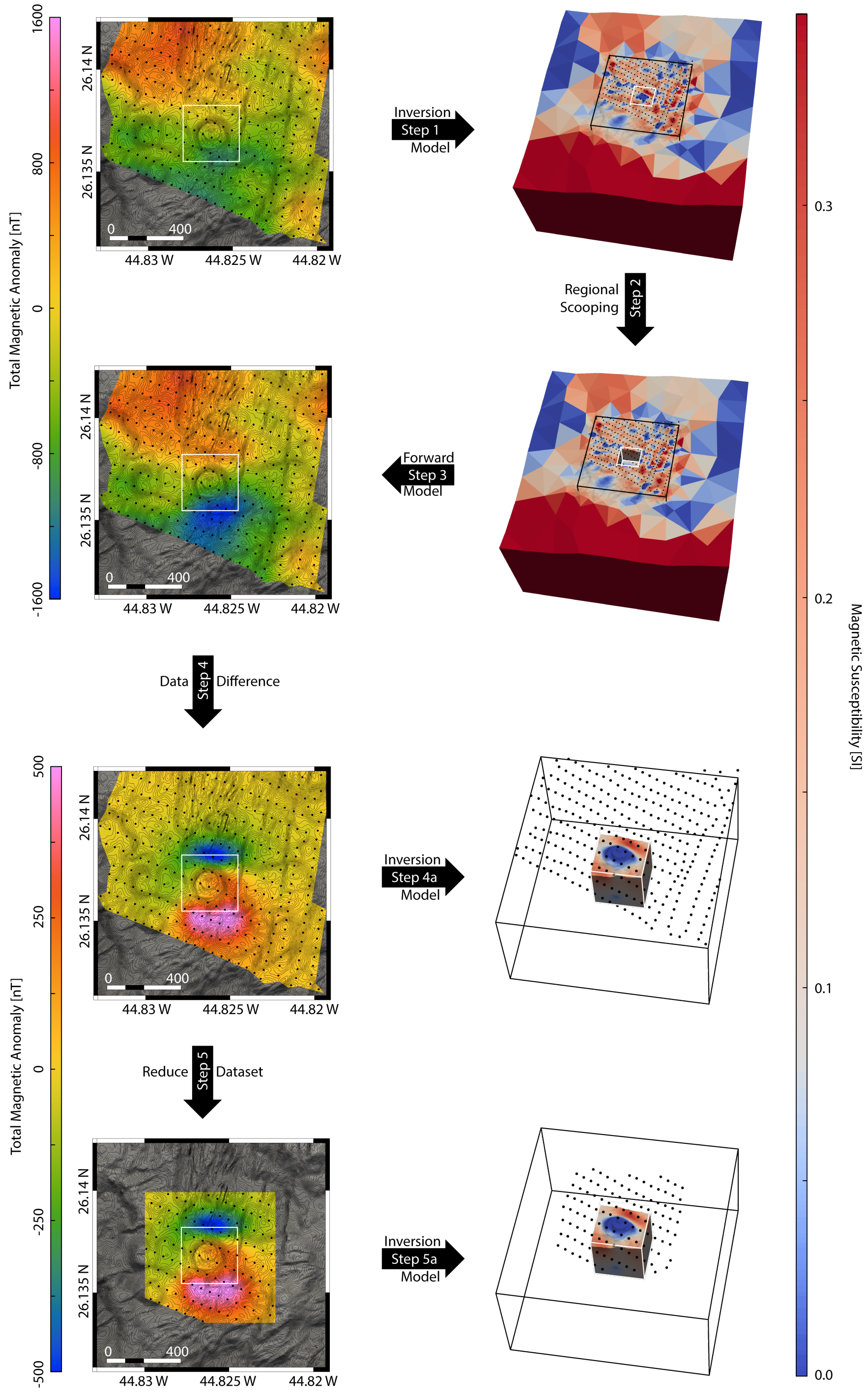

Figure 4.8: The workflow for the regional-removal process applied to the AUV magnetic data collected over the TAG mound. Step 1: invert the measured magnetic data, overfitting the data; step 2: determine the volume of seafloor that fully encompasses the TAG mound's magnetic anomaly, and remove that from the model; step 3: calculate the forward signal of the model missing the removed inner volume; step 4: calculate the different between the measured data and the calculated forward signal; step 5: down-sample the regionally-removed data set.

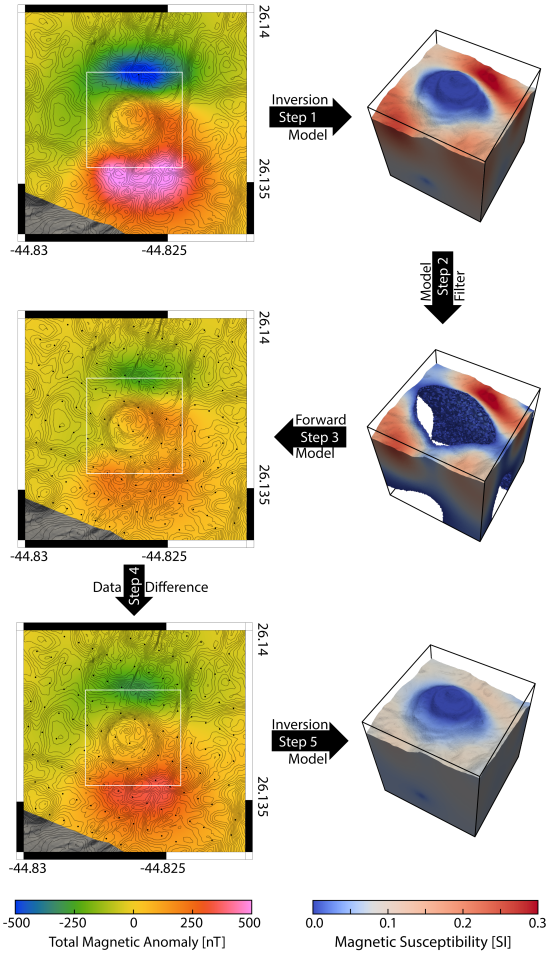

Figure 4.9: The workflow to develop a data set that is free from undesirable anomalously high magnetically susceptible regions of a voxel inversion model.

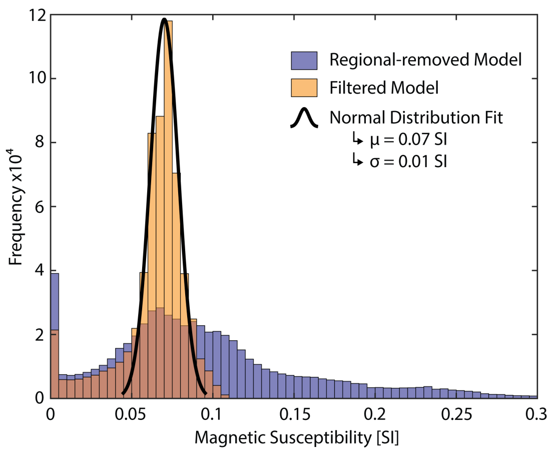

Figure 4.10: Two histograms representing the distribution of magnetic susceptibility values in the cells of the region removed and 0.08 SI filtered models.

volume during the inversion process. For the TAG active mound, the drillcore provides enough information to develop an initial model for both the deposit's massive sulfide layer base, and the outer extent of the chloritized basalt.

The initial model for the chloritized basalt (Fig. 4.11a, b) was defined as the inferred inner surface of this alteration type (see Fig. 4.1c for the drilling information), acting as a minimum volume that the SGI would then expand. The surface model was composed of 14 vertices, each of which could move in all three dimensions, resulting in 42 inversion parameters for the SGI. We held the model's physical properties constant throughout the inversion, using a value of 10^{-5} SI for the TAG active mound (Zhao et al., 1998), and a value of 0.08 SI for the background, as derived from the voxel inversion modelling. To bound the vertices in 3D, relative to their initial position (see Fig. 4.10a, b), constraints were assigned: $\pm$ 30 m for the upper seven vertices in the horizontal (East-West and North-South) plane, and vertical constraint of +0 m/-20 m; $\pm$ 100 m horizontally for the lower seven vertices, and +20 m/-300 m vertically.

As the physical properties in the SGI model are constant throughout the modelling, some uncertainty assessment is required to justify the choice of the anomalous and background susceptibilities. The assessment was performed by creating a suite of SGI models with varying magnetic susceptibility values, comparing the different models to the active mound's drillcore, then choosing the most geologically accurate model. Of the two magnetic susceptibility values in the SGI model the only one that needed to be assessed was the background value, as it is two orders of magnitude greater than the anomalous susceptibility. The SGI forward solver calculates a model's TMI anomaly based on the difference in susceptibilities across each of the surface model's facets (Okabe, 1979). Therefore, a model with a background susceptibility of 0.08 SI and an anomalous 0.00001 SI will have a 0.07999 SI outward difference across the model's facets. There could then be a variance of two orders of magnitude for the anomalous magnetic susceptibility and the contrast will be at most 0.079 SI. Comparatively, a much smaller uncertainty in the background's susceptibility will result in a much larger facet contrast, and therefore have a stronger effect on the geometry of the SGI model. Therefore, to study the effects of assuming different fixed magnetic susceptibility values only the background's value was adjusted. The range of background magnetic susceptibilities were chosen from the fitted normal distribution of Fig. 4.10, which had a mean of 0.07 SI and a standard deviation of 0.01 SI, created a range of [0.06, 0.08] SI. SGI models created with background susceptibilities of less than or equal to 0.075

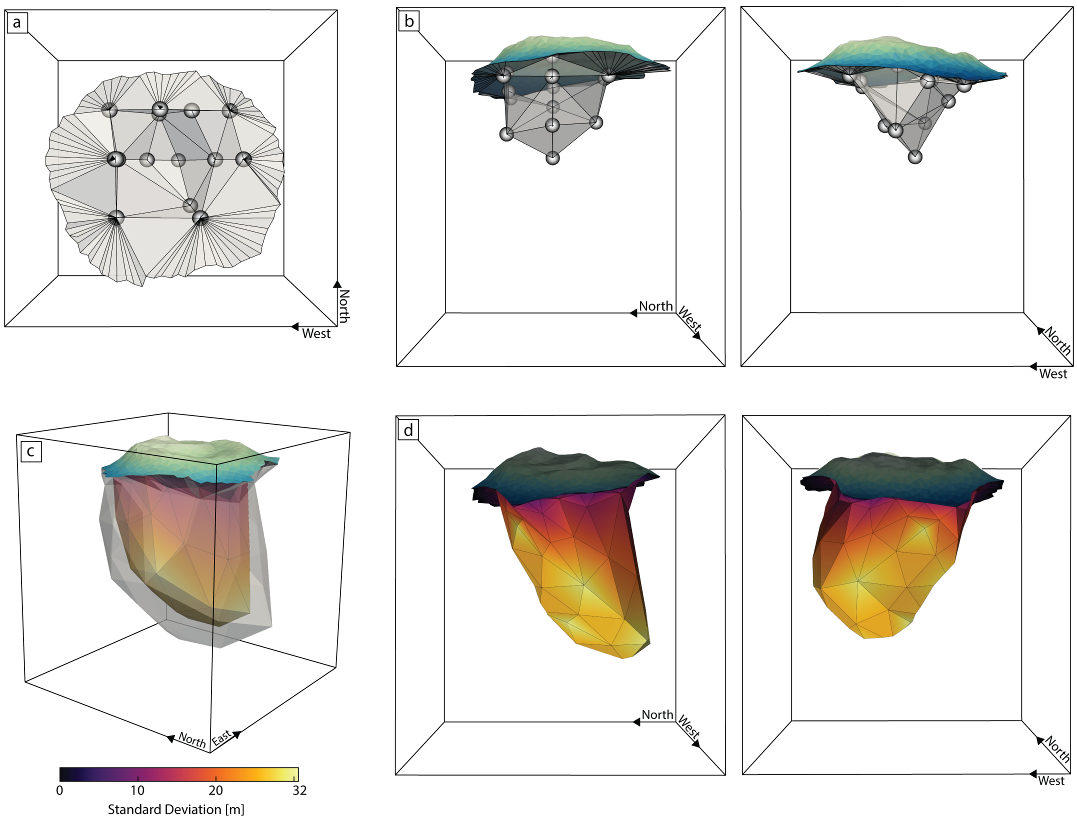

Figure 4.11: a) The plan view of the initial magnetic model with the bathymetry surface of TAG removed, and b) the same model including the bathymetric surface side on. The vertices of the initial model are grey spheres, and the top of the TAG active mound is coloured based on its bathymetry. c) The TAG active mound's sub-seafloor hydrothermal alteration SGI model result, with the mean model coloured based off its vertices' standard deviations, and the translucent grey surface is the mean model expanded by one standard deviation. d) Two half-slices of the magnetic SGI model, coloured by the model's vertices' standard deviations.

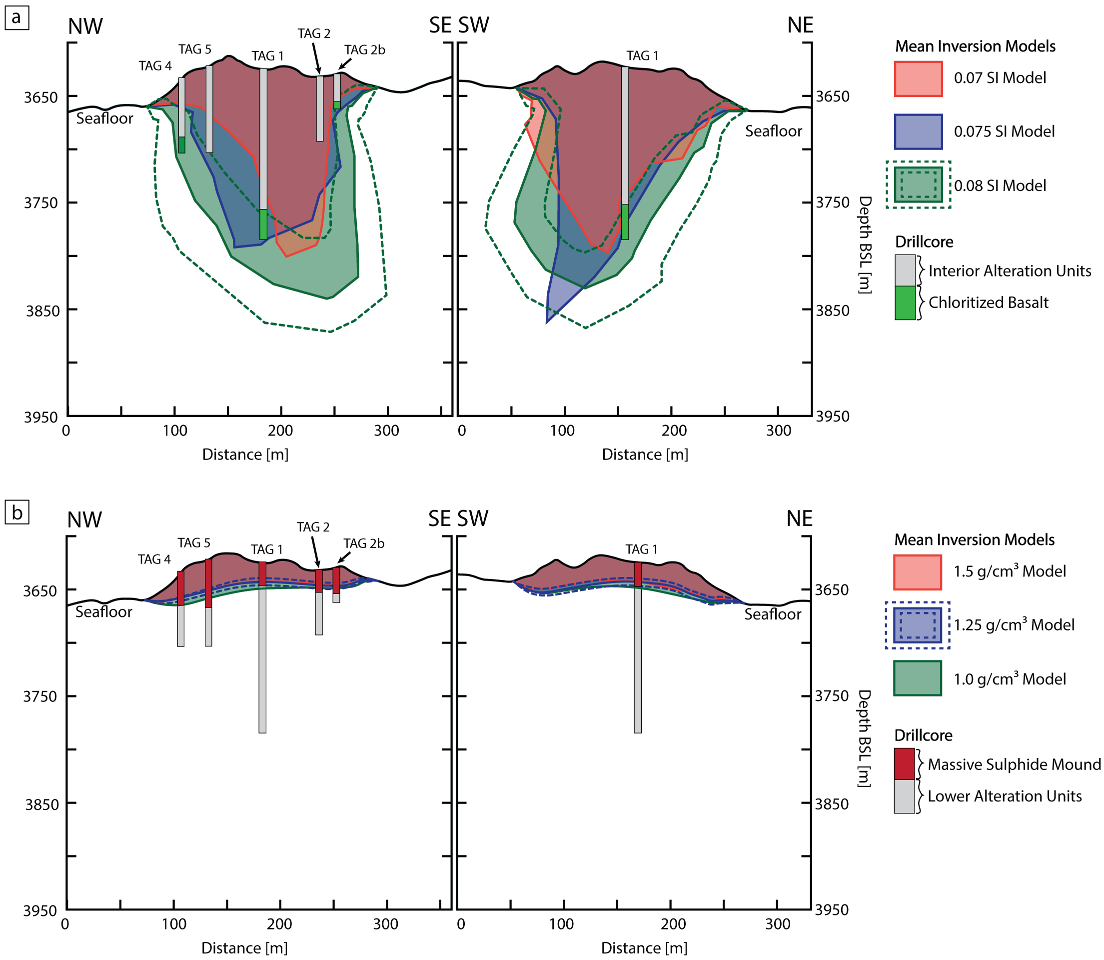

Figure 4.12: A comparison of the geometry of a) the magnetic SGI model inverted with three different background magnetic susceptibility values: 0.07, 0.075, and 0.08 SI, and b) the gravity model with anomalous mound densities of 1.0, 1.25, and 1.5 g/cm^3. The anomalous density being the contrast between the massive sulfide mound's density and the background basalt's density. Each of the 3D models are shown as two cross-sections, the left cross-section running parallel to the drillcores, and the right-hand cross-section perpendicular to it, following the same orientations as in Fig. 4.4b. In a and b the dotted lines represent a one standard deviation uncertainty on the position of the model's vertices.

SI produced a chloritized basalt model that was too small and did not agree with the bounds on the alteration units as defined from the drillcore. Models inverted with background values of 0.07, 0.075, and 0.08 SI can be seen in Fig. 4.12a, demonstrating the change in model geometry that results from using different magnetic susceptibility values. Within the 0.07 ± 0.01 SI range the background value of 0.08 SI produced the best model, agreeing most with the drillcore.

The SGI for the chloritized basalt model took 90 seconds to complete the GA optimization, and 5.5 hours to complete the MCMC sampling (see Fig. 4.13 for the convergence curves). Both programs were run on 48 threads on a 2.20 GHz Intel Xeon E5-2650 Processor, with the GA running in parallel and the MCMC in serial. The result of the magnetic SGI is shown in Fig.

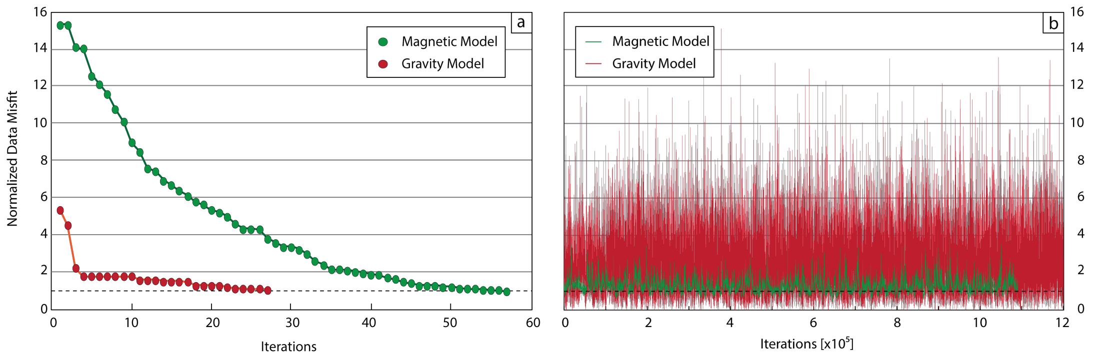

Figure 4.13: The convergence curves for the magnetic and gravity SGIs. a) The normalized data misfit curves from the GA optimization, and b) the curves from the MCMC optimization. The black dotted line in each plot shows the 1.0 target misfit for the inversion and sampling.

4.5b compared to the magnetic voxel inversion model, and again in Fig. 4.11c, d.

4.4.2 Gravity Inverse Modelling

As the gravity data only consisted of 11 stations, all roughly along a north-south line, a minimum-structure inversion of the data would be poorly constrained and produce an ambiguous subsurface model. Therefore, only SGI models were created from the gravity data. Of the eleven stations, only the eight closest to the TAG mound were used to develop the SGI model as the other three had low signal sensitivity to the density of the TAG mound.

The initial model for the base of the massive sulfide layer was derived from the available drillcore data (Fig. 4.4c). The vertices for the gravity SGI were constrained with +10 m/-50 m bounds relative to the starting model solely in the vertical direction, as the model for the massive sulfide was already well constrained from the drilling, and due to the low number of gravity data points. As in the modelling by Evans (1996), density values of 3.65 g/cm^3 and 2.4 g/cm^3 were used for the massive sulfide lens and underlying crust, respectively. As discussed in Graber et al. (2020), a range of densities have been used to represent the TAG active mound's massive sulfide, from 3.5 g/cm^3 to 3.8 g/cm^3. Therefore, a reasonable uncertainty on our choice of 3.65 g/cm^3 would be $\pm$ 0.15 g/cm^3. The 2.4 g/cm^3 density for the background basalt was chosen as it provided the best fit to the data while performing the Bouguer anomaly regional signal removal. Densities of 2.3 g/cm^3 and 2.5 g/cm^3 provided adequate fits as well, which would result in an effective background uncertainty of $\pm$ 0.1 g/cm^3. As the SGI forward solver calculated the gravitational signal of each facet in the surface model based off the difference in densities across the facets, the uncertainty of the difference in density between the massive sulfide mound and background basalt will be the sum of the individual uncertainties, i.e. $\pm$ 0.25 g/cm^3.

Therefore, the eight vertices used to define the massive sulfide layer model resulted in eight inversion variables. The subsequent SGI took 40 seconds to complete the GA, and 45 minutes to complete the MCMC sampling.

The gravity SGI resulted in an approximation of the lower surface of the massive sulfide mound, separating the lens from the altered seafloor crust. The volume of rock contained between the gravity model and the TAG active mound's bathymetric surface then approximates the volume of massive sulfide contained in the lens. The massive sulfide lens model has an approximate volume of 594,000 $\pm$ 120,000 m^3, which would indicate 2.17 $\pm$ 0.44 Mt of rock assuming the 3.65 g/cm^3 density used during the modelling, as used in Evans (1996). Figure 8b shows the SGI results using three density contrasts within the range of $\pm$ 0.25 g/cm^3 about the chosen $3.65 - 2.4 = 1.25$ g/cm^3 contrast. This comparison indicates the uncertainty on the geometry of the massive sulfide lens resulting from an uncertainty in the chosen density values.

4.5 Discussion

The two SGI models produced in this study provide new information on two important aspects of the TAG active mound: 1) the inversion of the gravity data provides a 3D model for the thickness of the massive sulfide layer of the deposit; and 2) the inversion of the magnetic data creates an enclosing surface representing the outer extent of the chlorite-rich hydrothermal alteration of basalt beneath the deposit. The outer extent of the chloritized basalt will therefore indicate the depth and location of mixing between hydrothermal fluid and seawater at temperatures greater than 200^{o}C. An updated geologic interpretation, in 3D, was made by combining the SGI surfaces with inferred interface information from the drillcore (Fig. 4.14).

Although the ODP Leg 158 drillholes were used to design the initial model for the SGIs, their information did not bias results or influence the inversions once they started. The initial models provided a geometry and topology that should be somewhat close to the actual form of the active mound's rock units, but once the inversions began the models' vertices moved within their positional constraints without influence from the initial model. The drillcore information was used to decide what background magnetic susceptibility to use, as multiple susceptibility values were used to construct a suite of SGI models but only the 0.08 SI background model was

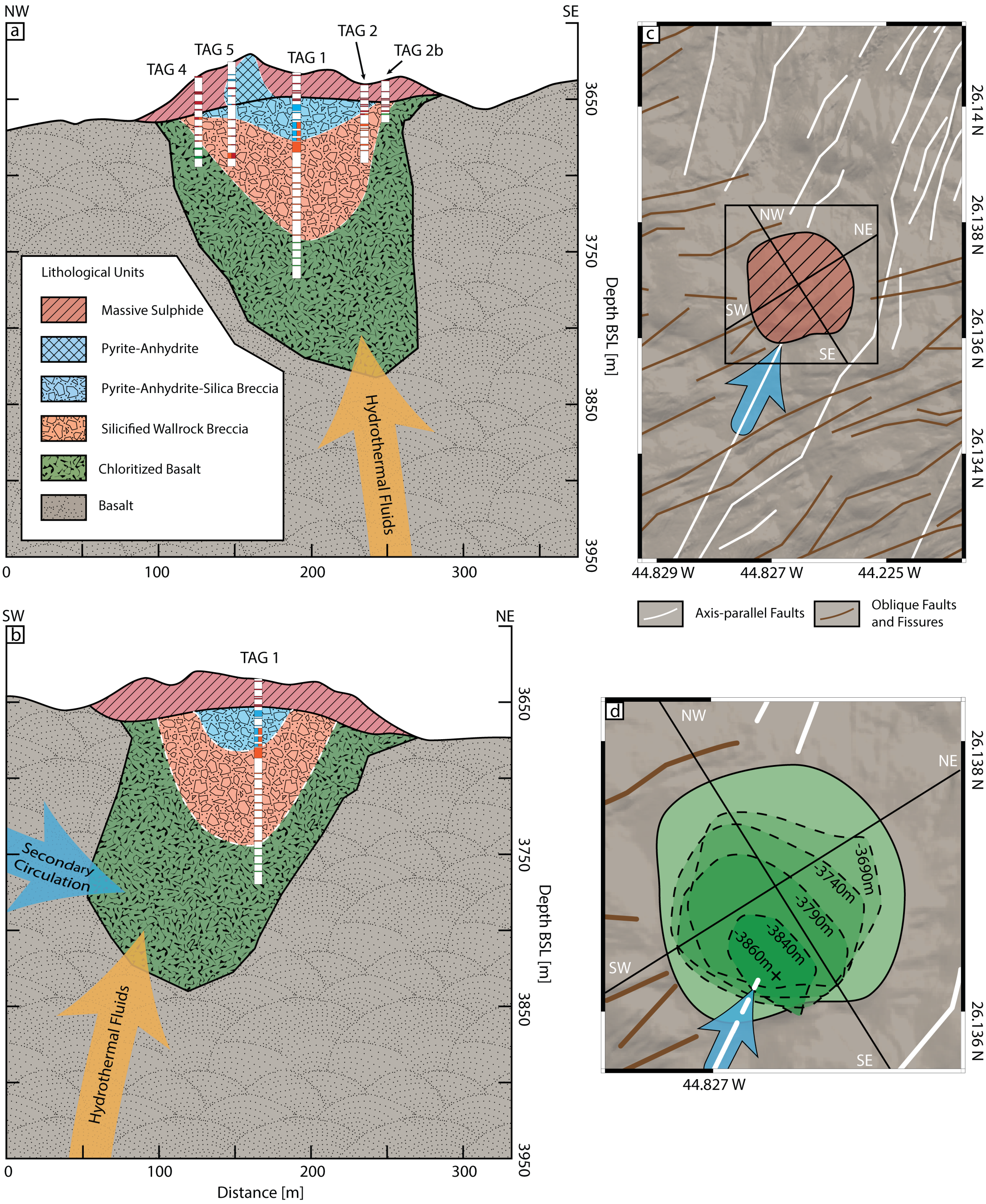

Figure 4.14: Two geological cross sections of the TAG active mound derived through gravity and magnetic geophysical inversion modelling and drillcore information. The cross-section a) is oriented parallel to the drillcores and b) orthogonal to them. Dotted white lines indicate inferred surfaces derived from the rock samples retrieved through drilling, and the solid black lines represent the surfaces created through SGI modelling. In both cross-sections the white space along the drillcores represents locations with zero recovery. c) Shows a plan view of the deposit with the interpreted vector for seawater recharge. d) A zoomed-in plan view of the deposit showing the isolines of the chloritized basalt surface's depth, with its maximum depth depicted with an "x".

both statistically appropriate as a background value as well as agreed with the drillcore. There were no chloritized basalt-basalt intersections in the drillcore to compare the magnetic SGI to, but the gravity SGI surface correlates closely with the bottom-most collected massive sulfide samples (Fig. 4.14).

The chloritized basalt model, which stretches down to $\approx$ 150 m below the seafloor, indicates that there is infiltration of local seawater (i.e. secondary circulation; Fig. 4.14) approaching the base of the mound from the South-West in line with the axis-parallel faulting passing through the mound (Fig. 4.1a). Pontbriand and Sohn (2014) determined a similar location of the secondary circulation through mapping the location of micro seismic events attributed to the precipitation of anhydrite at the locations of local seawater infiltration near the TAG mound. Their results showed a zone of high seismic event density to the immediate South-West of the mound, from the near surface to a depth of 125 m below the seafloor. This suggests that although the rising hydrothermal fluids are assumed to be approaching from the North-West on the regional scale (normal to the spreading axis; Szitkar and Dyment 2015), the locally infiltrating seawater and near-surface component of the upflow zone approaches the active mound along the axis-parallel faulting. The axis-parallel faulting is present to both the North and South of the TAG mound, but the southern faults are seen to be heavily cross-cut by axis-oblique faults and fissures (Fig. 4.1a).

Comparing the geometry of the modelled chloritized basalt unit to ancient VMS systems, primarily Cyprus-type deposits that have relatively undeformed alteration facies, the chlorite alteration units can have a range of thicknesses. The thicknesses of the units at the Mathiati deposit are 10-50 m, and 100-200 m thick at the Skouriotissa deposit (Hannington et al., 1998). These thicknesses are proportional to the size of the deposits, as a larger ore lens relates to a larger stockwork system, but they do compare to the 10-75 m thick modelled chloritized basalt unit for the TAG active mound.

Using the massive sulfide lens SGI model, the volume of rock contained between it and the overlying bathymetric surface was calculated to be 595,000 $m^3 \pm 20\%$. The derived tonnage of 2.17 $\pm$ 0.44 Mt of rock is in agreement with Graber et al. (2020)'s 2.27 Mt approximation, which was measured by placing an interpolated surface through the TAG mound to separate the unit of massive sulfide from the altered crust (Jamieson et al., 2014a) and assuming a 3.5 g/cm^3 density. If 3.65 g/cm^3 was assumed for the density in Graber et al. (2020)'s the result would have been a tonnage of 2.37 Mt, still in agreement with 2.17 $\pm$ 0.44 Mt. As seen in Figure 4.4d, the base of the massive sulfide lens matches closely with the form of the surrounding bathymetric surface, most notably observed by the raised region in the center of the mound aligning with the raised pillow mound terrain noted in Graber et al. (2020). The other study that approximated the massive sulfide tonnage in the TAG active mound was Hannington et al. (1998), that used a blocky model of cylindrical units. Their calculated tonnage was 2.7 Mt for the massive sulfide lens, higher than the value derived from this study's model and that of Graber et al. (2020). This is most likely caused by the relatively large size of the units in the blocky model adding extra volume as the five cylinders at the top of the model could not accurately fit the active mound's topography. Additionally, Hannington et al. (1998) used a 3.8 g/cm^3 density in their calculations; if 3.65 g/cm^3 was used as in this study their tonnage would be 2.6 Mt. It is ideal that the SGI derived tonnage agrees with those of previous studies, as it demonstrates that an accurate tonnage can be calculated through the inversion of geophysical data that can be collected at a fraction of the cost needed to drill the deposit and develop a geologic model.

In the analysis of the geometry of the massive sulfide mound's inversion model, the downward concavity of the mound's base implies that the replacement alteration of the seafloor below the mound did not significantly increase its density. The alteration below the mound is composed of basalt brecciated with veins of silicate, sulfide, and sulfate minerals. The density for these lower alteration units and the background basalt used in this study was 2.4 $\pm$ 0.1 g/cm^3. Since the density of the replacement alteration units appears similar to the unaltered basalt, it would imply that there is not a significant amount of higher density massive sulfide present in that region. However, this would contradict the samples collected from ODP Leg 158 which recorded an average of 34 % composition of pyrite in the pyrite-anhydrite-silica breccia and the silicified wallrock breccia units (Ludwig et al., 1998). A possible explanation for the density of altered seafloor is that the drillcore recovery efficiency, which was 12% in Leg 158 (Humphris and Tivey, 2000), is biased towards intervals that contain abundant higher density sulfide minerals. The higher density intervals would not crumble so easily during the drilling and would remain intact during retrieval. There might therefore be a lower amount of pyrite present in the seafloor below the massive sulfide lens than the Leg 158 drilling suggests. Of the samples recovered during the Leg 158 drilling, their mean percent composition was 34 % sulfide, 4.5 % anhydrite, 58 % quartz, and 3 % clay (Ludwig et al., 1998). Treating the composition of the recovered 12 % of the core as representative of 12 % of the stockwork zone, a geologic model of the remaining 88 % was constructed to determine its composition. The model is made up of percentages of pyrite (5 g/cm^3; Sharma 1997), quartz (2.65 g/cm^3; Sharma 1997), anhydrite/basalt (2.9 g/cm^3; Sharma 1997) and pore fluid (0.9 g/cm^3; Bischoff and Pitzer 1985), while constrained by the modeled bulk density of the stockwork zone (2.4 g/cm^3) and that the percentages of the minerals and porosity sum to 100 %,

$$2.4g/cm^3 = \%_{pyrite}\cdot(5g/cm^3)+\%_{quartz}\cdot(2.65g/cm^3)+\%_{basalt}\cdot(2.9g/cm^3)+\%_{porosity}\cdot(0.9g/cm^3) \tag{4.7}$$

$$100\% = \%_{pyrite} + \%_{quartz} + \%_{basalt} + \%_{porosity}. \tag{4.8}$$

As seen in Fig. 4.15, the indicated upper bound of pyrite possible in the stockwork zone would be 30 % (at a porosity of 63 %), with the lower bound being the 4.1 % already observed in the drillcore. It is unlikely that the stockwork zone's alteration would greatly increase its porosity, with some studies indicating that the alteration instead decreases porosity with the precipitation of sulfides, sulfates, and silicates (Wilkens et al., 1991; Zhu et al., 2007). Therefore, the percent volume of pyrite in the stockwork zone might be better constrained by considering porosities equal to or less than the background basalt's 26 %. This would indicate that at most 7.9 % of the stockwork zone would be composed of pyrite, occurring when there is zero basalt or anhydrite remaining and the alteration zone is solely sulfides and silicates.

This chapter's magnetic modelling assumed that all significant magnetization in the crust around the TAG active mound was parallel to the Earth's inducing field, although some previous studies have suggested that remanence oblique to the Earth's field might be present. Szitkar and Dyment (2015) found through magnetic forward modelling that the crustal magnetization under the TAG mound was rotated from the International Geomagnetic Reference Field's (IGRF) 42° inclination and -15° declination to a 10° inclination and 0° declination. This 53° rotation of the crust's magnetization about an axis parallel to the Mid-Ocean Ridge axis was concluded to be caused by the detachment fault tectonics in the region. To consider the presence of remanent magnetization oblique to the Earth's inducing field vector a TMVI model was created to study any significant deviations of the model's magnetization vectors (Fig. 4.6). The results indicated

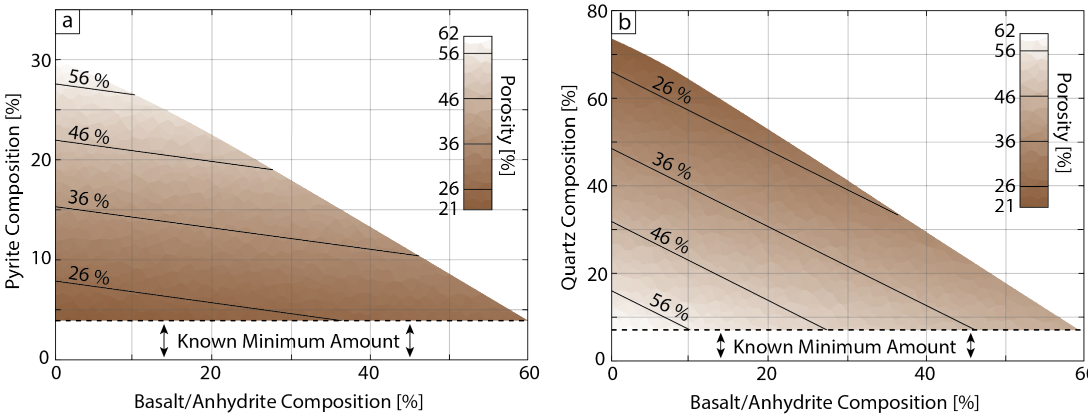

Figure 4.15: A geologic model of the percent composition of pyrite, quartz, basalt/anhydrite, and pore fluid that makes up the TAG active mound's stockwork zone. a) A plot showing the percent composition of pyrite versus the composition of basalt/anhydrite, with each black line representing a constant porosity, at intervals of 10 % from the background value of 26 %. b) The same style of plot for quartz versus basalt/anhydrite.

that the models showed a strong preference to have their magnetization in-line with the IGRF vector, with small groupings of cells containing oblique magnetizations, with respect to the IGRF, being associated with overfitting of the data. The effective magnetic susceptibility TMVI model contains less heterogeneities in the crust surrounding the TAG active mound, as given more degrees of freedom (i.e. effective magnetic susceptibility, inclination and declination, versus simply effective magnetic susceptibility as in the scalar magnetic inversion model) the TMVI program used near-surface variations from the IGRF direction to better fit the data rather than varying purely the effective magnetic susceptibility.

The SGI models were derived by individually inverting the magnetic and gravity data. The SGI program has the capability to jointly invert both data sets, but it was not necessary for this study. Jointly inverting the magnetic and gravity data would have been beneficial if the base of the massive sulfide and the outer extent of the chloritized basalt were connected and shared vertices. At the TAG active mound these two surfaces do not appear to be connected, with the base of the massive sulfide lens contained within the chloritized basalt volume. Therefore, a joint inversion should not produce a noticeably different result and would only complicate and slow the inversion by introducing more surfaces to possibly intersect one another during the GA optimization and MCMC sampling.

A limitation of the gravity and magnetic modelling of SMS deposits is the inability of these data to resolve the size and geometry of the silicified wallrock stockwork breccia zone below the massive sulfide lens. This zone may contain a significant portion of the deposit's precious and base metals and determining its volume would be of economic importance. Future work should combine the gravity and magnetic modelling with CSEM surveying (e.g. Gehrmann et al. 2019; Haroon et al. 2018) and seismic modelling (e.g. Murton et al. 2019) to resolve the stockwork zone.

4.6 Conclusion

With the use of surface geometry inversion, sparse drilling and minimum-structure inversion results were further refined to develop a more comprehensive 3D wireframe geologic model of the TAG active mound. Such wireframe models are composed of surfaces representing the discrete contacts between different rock units, which, in the case of the TAG active mound, were the interface between the massive sulfide lens and the underlying altered basalt, and the interface between the chloritized basalt and the unaltered/minimally altered background basalt. Our gravity inversion model presented a 2.17 $\pm$ 0.44 Mt massive sulfide estimate for anhydrite contained in the deposit's mound, and the magnetic inversion modelled the maximum depth where infiltrating seawater mixes with the rising hydrothermal fluids. The model is however limited in its inability to resolve the geometry of the deposit's silicified wallrock breccia zone, but through the future integration of other geophysical surveying methods this could be rectified.

Chapter 5

Conclusion

5.1 Research Summary

Geophysical inverse modelling is a key tool in the exploration for and analysis of the seafloor's polymetalic mineral deposits, specifically seafloor massive sulfide (SMS) deposits. To combat the challenges in developing geologic interpretations of the deposits from sparse seafloor drilling, the surface geometry inversion method was developed to create three-dimensional wireframe models of a deposit's massive sulfide lens and chloritized basalt breccia. On the regional scale, magnetic minimum-structure inverse modelling was demonstrated to be an effective tool to map the high-temperature fluid pathways that supply metals the the SMS deposits, and in doing so resolved the first empirical model of a hydrothermal fluid's upflow zone.

5.1.1 Mapping Hydrothermal Upflow Zones through Magnetic Inverse Modelling; East Manus Basin

This chapter outlined the magnetic minimum-structure inverse modelling that was performed on multiple data sets over the Tumai and Bugave Ridge in the East Manus Basin. Along the Tumai Ridge lies numerous actively venting or inactive hydrothermal venting sites, including the Solwara 1 SMS deposit which was the first NI43-101 compliant SMS deposit (Lipton, 2012). Utilizing the fact that high-temperature hydrothermal fluids lower the magnetic properties of the crust it interacts with, three-dimensional magnetic models were developed of the seafloor crust about the Tumai and Bugave Ridges to map the pathways the hydrothermal fluids take en route from their magmatic heat source to the seafloor. The largest of the developed inverse models mapped the entire upflow zone of the hydrothermal cell beneath the Tumai Ridge, through which the volume of crust exposed to the leaching fluids was measured and the sub-seafloor connectivity of hydrothermal venting communities was established. Understanding the geometery of hydrothermal upflow zones has important implications to not just the academic study of these systems, but also to their potential assessments as mineral resources. Not all SMS deposits have visible seafloor relief features, as they can be buried by sedimentary layers. The magnetic modelling of the upflow zones then allows for the exploration of these difficult to identify sites.

5.1.2 Surface Geometry Inverse Modelling

The third chapter outlined the developed surface geometry inverse (SGI) modelling method, as well as demonstrated its capabilities through a series of synthetic modelling examples. The SGI method is not fundamentally new to the earth science community, but the presented method made a number of advancements and optimizations. These include being able to work directly with three-dimensional explicit surfaces from an input geological model of arbitrary complexity, incorporating intersection detection methods to avoid unacceptable topological scenarios, employing global optimization strategies and stochastic sampling to solve the inverse problem and aid model assessment, and using surface subdivision to reduce the number of model parameters and act as a form of regularization without adding the complications of tradeoff parameters in the objective function. A suite of synthetic examples were modelling in this chapter to demonstrate the capabilities of the SGI method.

5.1.3 Local Hydrothermal Alteration Modelling; Trans-Atlantic Geotraverse Active Mound

The last research chapter demonstrated the effectiveness of the developed SGI method on modelling the geometry of SMS deposits through inversion of both magnetic and gravity data collected over the TAG active mound. The magnetic inversion model was able to solve for the position of the surface separating the chloritized basalt from the basaltic host rock, providing insight on the scale of the secondary mixing between the hydrothermal fluids and seawater. The gravity inversion model provided thickness estimates of the deposit's massive sulfide lens, the portion of the deposit that contains the highest grades of precious and base metals in the deposit. This chapter's modelling demonstrated that sparse drilling, a small, single survey line of gravity measurements and a magnetic AUV survey provided enough information to create a detailed 3D model of an SMS deposit. This leads to a more efficient, remote sensing-heavy methodology of assessing the size and value of an SMS deposit, which will be valuable in this up and coming industry.

5.2 Future Outlook

This thesis set up modelling methodologies for both the regional and deposit scale modelling of SMS deposits and their host systems, allowing similar modelling to be performed on any other magnetic and/or gravity data sets collected for SMS exploration.

Although this thesis has shown the use of magnetic and gravity modelling can provide new insight into the geometry of hydrothermal convection systems and SMS deposits, much more knowledge could be gained by studying a greater variety of data types. Crustal scale magnetotelluric, gravity, and seismic studies could greatly complement the magnetic models by providing more information of the geometry of the magmatic heat source and the structure of the crust that hosts the hydrothermal system. On the deposit scale the magnetic and gravity modelling combined could resolve the thickness of the massive sulfide lens and the outer shell of the chloritized basalt, but these models could not resolve the geometry of the stockwork stringer zone within the deposit. This zone also contains high grades of precious and base metals, so determining its shape and volume would enhance our resource estimates of the deposits. To measure the size of the stockwork zone high resolution electromagnetic (EM) models of SMS deposits could be made. At present the code associated with EM SGI modelling is under development by other researchers (Lu et al., 2020).

As discussed in the chapters focusing on the development and application of the SGI method, the method has shown to be very effective, but still has some significant constraints. Primarily, the fact that physical properties must remain fixed during the inversion modelling, and therefore the decision of what they should be can carry significant weight. Much more research can be done looking into some way to limit the need for a priori constraints while still ensuring that the inverse problem remains unique. This could be carried out by allowing the physical properties within the wireframe model's segments to vary during the inversion, or perhaps somewhat combining the voxel and SGI methods so that within the SGI model's discrete zones there can be a somewhat smooth distribution of a physical property.

The use of our global optimization methods could also be improved, or at least more experimentation could be performed. In particular, the use of a MCMC sampler provides important information on model uncertainties, but significantly increased the run times for the SGI modelling. Determining a better way of sampling the solution space about the global minimum found with the GA method would be greatly beneficial, and make the modelling method more attractive to industry.

This thesis has focused on the modelling of seafloor mineral deposits, although just as voxel-based inverse modelling has been extensively applied to terrestrial mineral exploration so too can SGI. Any system that can be described as being a collection of petrophysically discrete units is a good candidate for the SGI method, giving this method far reaching applications. In fact, more data is available for terrestrial deposits, such as VMS deposits, which would make their modelling with both the voxel-based and SGI methods much more easily applicable and more widely impactful.

Bibliography

Ade-Hall, J., Palmer, H., and Hubbard, T. (1971). The magnetic and opaque petrological response of basalts to regional hydrothermal alteration. *Geophysical Journal of the Royal Astronomical Society*, 24(2):137–174.

Al-Chalabi, M. (1972). Interpretation of gravity anomalies by non-linear optimization. *Geophysical Prospecting*, 20:1–16, doi:10.1111/j.1365–2478.1972.tb00616.x.

Ames, D. E., Franklin, J. M., and Hannington, M. D. (1993). Mineralogy and geochemistry of active and inactive chimneys and massive sulfides, middle valley, northern juan de fuca ridge: an evolving hydrothermal system. *Canadian Mineralogist*, 31(4):997–1024.

Anderson, R., Zoback, M., Hickman, S., and Newmark, R. (1985). Permeability versus depth in the upper oceanic crust: In situ measurements in DSDP hole 504B, eastern equatorial Pacific. *Journal of Geophysical Research: Solid Earth*, 90:3659–3669.

Anquez, P., Pellerin, J., Irakarama, M., Cupillard, P., Lévy, B., and Caumon, G. (2019). Automatic correction and simplification of geological maps and cross-sections for numerical simulations. *Comptes Rendus Geoscience*, 351:48–58, doi:10.1016/j.crte.2018.12.001.

Ansari, S., Farquharson, C., and MacLachlan, S. (2017). A gauged finite-element potential formulation for accurate inductive and galvanic modelling of 3-d electromagnetic problems. *Geophysical Journal International*, 210:105–129.

Ansari, S. and Farquharson, C. G. (2014). 3D finite-element forward modeling of electromagnetic data using vector and scalar potentials and unstructured grids. *Geophysics*, 79:E149–E165, doi:10.1190/geo2013–0172.1.

Auken, E. and Christiansen, A. V. (2004). Layered and laterally constrained 2D inversion of resistivity data. *Geophysics*, 69:752–761, doi:10.1190/1.1759461.

Auster, H., Glassmeier, K., Magnes, W., Aydogar, O., Baumjohann, W., Constantinescu, D., Fischer, D., Fornacon, K., Georgescu, E., Harvey, P., et al. (2008). The themis fluxgate magnetometer. *Space Science Reviews*, 141(1-4):235–264.

Autodesk (2017). Autodesk Meshmixer, http://www.meshmixer.com, last accessed November 2017.

Auzende, J. M., Ishibashi, J. I., Beaudoin, Y., Charlou, J. L., Delteil, J., Donval, J. P., Fouquet, Y., Ildefonse, B., Kimura, H., Nishio, Y., Radford-Knoery, J., and Ruøllan, E. (2000). Extensive magmatic and hydrothermal activity documented in Manus Basin. *Eos*, 81(39):1–3.

Auzende, J.-M. and Urabe, T. (1996). Cruise explores hydrothermal vents of the Manus Basin. *Eos, Transactions America Geophysical Union*, 77(26).

Beardsmore, G., Durrant-Whyte, H., McCalman, L., O'Callaghan, S., and Reid, A. (2016). A bayesian inference tool for geophysical joint inversions. *ASEG Extended Abstracts*, 2016:1–10.

Beaudoin, Y. and Scott, S. D. (2009). Pb in the PACMANUS sea-floor hydrothermal system, Eastern Manus Basin: numerical modelling of magmatic versus leached origin. *Economic Geology*, 104(3):749–758.

Bijani, R., Lelièvre, P. G., Ponte-Neto, C. F., and Farquharson, C. G. (2017). Physical property-, lithology- and surface-based joint inversion using Pareto multi-objective global optimization. *Geophysical Journal International*, 209:730–748.

Bijani, R., Ponte-Neto, C. F., Carlos, D. U., and Silva Dias, F. J. (2015). Three-dimensional gravity inversion using graph theory to delineate the skeleton of homogeneous sources. *Geophysics*, 80:G53–G66.

Bina, M. M. and Prévot, M. (1989). Thermomagnetic investigations of titanomagnetite in submarine basalts: evidence for differential maghemitization. *Physics of the Earth and Planetary Interiors*, 54(1):169 – 179.

Binns, R. and Scott, S. D. (1993). Actively forming polymetallic sulfide deposits associated with felsic volcanic rocks in the eastern manus back-arc basin, papua new guinea. *Economic Geology*, 88(8):2226–2236.

Binns, R. A., Scott, S. D., Gemmell, J. B., and Crook, K. A. W. C. (1997). The Susu Knolls hydrothermal field, Eastern Manus Basin, Papua New Guinea. *Eos, Transactions America Geophysical Union*, 78:F772.

Bischoff, J. L. and Pitzer, K. S. (1985). Phase relations and adiabats in boiling seafloor geothermal systems. *Earth and Planetary Science Letters*, 75(4):327–338.

Bonneau, F., Botella, A., Mazuyer, A., Anquez, P., Chauvin, B., and Caumon, G. (2018). Ringmesh: an open source platform for shared earth modeling. In *80th EAGE Conference and Exhibition 2018*, pages 1–5. European Association of Geoscientists & Engineers.

Bosch, D., Jamais, M., Boudier, F., Nicolas, A., Dautria, J. M., and Agrinier, P. (2004). Deep and high-temperature hydrothermal circulation in the Oman ophiolite - Petrological and isotopic evidence. *Journal of Petrology*, 45(6):1181–1208.

Bouligand, C., Tivey, M. A., Finn, C. A., Morgan, L. A., Shanks III, W. P., and Sohn, R. A. (2020). Geological and thermal control of the hydrothermal system in northern yellowstone lake: Inferences from high-resolution magnetic surveys. *Journal of Geophysical Research: Solid Earth*, 125(9):e2020JB019743.

Bronner, A., Sauter, D., Munschy, M., Carlut, J., Searle, R., Cannat, M., and Manatschal, G. (2014). Magnetic signature of large exhumed mantle domains of the Southwest Indian Ridge – Results from a deep-tow geophysical survey over 0 to 11 Ma old seafloor. *Solid Earth*, 5(1):339–354.

Buck, W. R., Lavier, L. L., and Poliakov, A. N. (2005). Modes of faulting at mid-ocean ridges. *Nature*, 434(7034):719–723.

Byerly, G. R., Melson, W. G., and Vogt, P. R. (1976). Rhyodacites, andesites, ferro-basalts and ocean tholeiites from the galapagos spreading center. *Earth and Planetary Science Letters*, 30(2):215–221.

Cai, H. and Zhdanov, M. S. (2015). Modeling and inversion of magnetic anomalies caused by sediment–basement interface using three-dimensional Cauchy-type integrals. *IEEE Geoscience and Remote Sensing Letters*, 12:477–481, doi:10.1109/LGRS.2014.2347275.

Caratori Tontini, F., De Ronde, C. E., Yoerger, D., Kinsey, J., and Tivey, M. (2012). 3-D focused inversion of near-seafloor magnetic data with application to the Brothers volcano hydrothermal system, Southern Pacific Ocean, New Zealand. *Journal of Geophysical Research: Solid Earth*, 117(10):1–12.

Carter-McAuslan, A., Lelièvre, P. G., and Farquharson, C. G. (2015). A study of fuzzy c-means coupling for joint inversion, using seismic tomography and gravity data test scenarios. *Geophysics*, 80:W1–W15.

Cathles, L. M. (2011). What processes at mid-ocean ridges tell us about volcanogenic massive sulfide deposits. *Mineralium Deposita*, 46(5):639–657.

Caumon, G. (2018). Geological objects and physical parameter fields in the subsurface: a review. In *Handbook of Mathematical Geosciences*, pages 567–588. Springer.

Caumon, G., Collon-Drouaillet, P., Le Carlier de Veslud, C., Viseur, S., and Sausse, J. (2009). Surface-based 3D modeling of geological structures. *Mathematical Geosciences*, 41:927–945.

Caumon, G., Gray, G., Antoine, C., and Titeux, M. (2013). 3D implicit stratigraphic model building from remote sensing data on tetrahedral meshes: theory and application to a regional model of La Popa Basin, NE Mexico. *IEEE Transactions on Geoscience and Remote Sensing*, 51:1613–1621, doi:10.1109/tgrs.2012.2207727.

Charlou, J., Bougault, H., Fouquet, Y., Donval, J., Douville, E., Radford-Knoery, J., Aballéa, M., Needham, H., Jean-Baptiste, P., Rona, P., et al. (1996). Methane degassing, hydrothermal activity and serpentinization between the fifteen-twenty fracture zone area and the azores triple junction area (mid-atlantic ridge). In *Fara meeting–Mid-Atlantic Ridge Symposium, Reyjavick, Iceland*, pages 771–772.

Charlou, J. L., Donval, J. P., Konn, C., OndréAs, H., Fouquet, Y., Jean-Baptiste, P., and Fourré, E. (2010). High production and fluxes of h2 and ch4 and evidence of abiotic hydrocarbon synthesis by serpentinization in ultramafic-hosted hydrothermal systems on the mid-atlantic ridge. *Diversity of hydrothermal systems on slow spreading ocean ridges*, 188:265–296.

Charlou, J. L., Donval, J. P., Konn, C., Ondréas, H., Fouquet, Y., Jean-Baptiste, P., and Fourré, E. (2013). High Production and Fluxes of H2 and CH4 and Evidence of Abiotic Hydrocarbon

Synthesis by Serpentinization in Ultramafic-Hosted Hydrothermal Systems on the Mid-Atlantic Ridge. *Diversity of Hydrothermal Systems on Slow Spreading Ocean Ridges*, pages 265–296.

Chen, J., Hoversten, G. M., Key, K., Nordquist, G., and Cumming, W. (2012). Stochastic inversion of magnetotelluric data using a sharp boundary parameterization and application to a geothermal site. *Geophysics*, 77:E265–E279.

Chester, R. and Jickells, T. (2012). The transport of material to the oceans: the fluvial pathway. *Marine Geochemistry*, pages 11–51.

Chib, S. and Greenberg, E. (1995). Understanding the metropolis-hastings algorithm. *The American Statistician*, 49:327–335, doi:10.2307/2684568.

Collinson, D. (1965). Depositional remanent magnetization in sediments. *Journal of Geophysical Research*, 70(18):4663–4668.

Constable, S. C., Parker, R. L., and Constable, C. G. (1987a). Models From Electromagnetic Sounding Data. *Geophysics*, 52(3):289–300.

Constable, S. C., Parker, R. L., and Constable, C. G. (1987b). Occam's inversion: A practical algorithm for generating smooth models from electromagnetic sounding data. *Geophysics*, 52(3):289–300.

Danaei, B., Karbasizadeh, N., and Masouleh, M. T. (2017). A general approach on collision-free workspace determination via triangle-to-triangle intersection test. *Robotics and Computer-Integrated Manufacturing*, 44:230–241.

Datta, D., Sen, M. K., Liu, F., and Morton, S. (2019). Full-waveform inversion of salt models using shape optimization and simulated annealing. *Geophysics*, 84:R793–R804.

De Pasquale, G., Linde, N., Doetsch, J., and Holbrook, W. S. (2019a). Probabilistic inference of subsurface heterogeneity and interface geometry using geophysical data. *Geophysical Journal International*, 217:816–831.

De Pasquale, G., Linde, N., and Greenwood, A. (2019b). Joint probabilistic inversion of DC resistivity and seismic refraction data applied to bedrock/regolith interface delineation. *Journal of Applied Geophysics*, page 103839.

de Ronde, C. E., Baker, E. T., Massoth, G. J., Lupton, J. E., Wright, I. C., Feely, R. A., and Greene, R. R. (2001). Intra-oceanic subduction-related hydrothermal venting, kermadec volcanic arc, new zealand. *Earth and Planetary Science Letters*, 193(3-4):359–369.

Deb, K., Pratap, A., Agarwal, S., and Meyarivan, T. (2002). A fast and elitist multiobjective genetic algorithm: NSGA-II. *IEEE Transactions on Evolutionary Computation*, 6:182–197, doi:10.1109/4235.996017.

deGroot-Hedlin, C. and Constable, S. (2004). Inversion of magnetotelluric data for 2D structure with sharp resistivity contrasts. *Geophysics*, 69:78–86, doi:10.1190/1.1649377.

Dentith, M. and Mudge, S. T. (2014). *Geophysics for the mineral exploration geoscientist*. Cambridge University Press.

Douville, E., Charlou, J., Donval, J., Knoery, J., Fouquet, Y., Bienvenu, P., Appriou, P., et al. (1997). Trace elements in fluids from the new rainbow hydrothermal field (36 14 n, mar): a comparison with other mid-atlantic ridge fluids. *Eos Trans. AGU*, 78:832.

Dunlop, D. (1990). Developments in rock magnetism. *Reports on Progress in Physics*, 53(6):707.

Dunlop, D. J. and Özdemir, Ö. (2001a). Beyond néel's theories: thermal demagnetization of narrow-band partial thermoremanent magnetizations. *Physics of the Earth and Planetary Interiors*, 126(1-2):43–57.

Dunlop, D. J. and Özdemir, Ö. (2001b). *Rock magnetism: fundamentals and frontiers*, volume 3. Cambridge university press.

Dyriw, N. and Parianos, J. (2018). Understanding the ore mineralisation of the deep sea : New insights from Solwara 1 Cu-Au Ore deposit and the East Manus Basin , PNG. *2018 International Marine Minerals: A new resource of the 21st century, Geological Society of London*.

Dyriw, N. J., Bryan, S. E., Richards, S. W., Parianos, J. M., Arculus, R. J., and Gust, D. A. (2021). Morphotectonic analysis of the east manus basin, papua new guinea. *Frontiers in Earth Science*, page 698.

Evans, A. M. (1993). *Ore geology and industrial minerals: an introduction, 3rd Ed.* Wiley-Blackwell.

Evans, R. L. (1996). A seafloor gravity profile across the TAG hydrothermal mound. *Geophysical Research Letters*, 23(23):3447–3450.

Farquharson, C. and Lelièvre, P. (2017). Modelling and inversion for mineral exploration geophysics: a review of recent progress, the current state-of-the-art, and future directions. In *Proceedings of Exploration 17: Sixth Decennial International Conference on Mineral Exploration*. DMEC.

Farquharson, C. G. and Oldenburg, D. W. (1998). Non-linear inversions using general measures of data misfit and model structure. *Geophysical Journal International*, 134:213–227, doi:10.1046/j.1365–246x.1998.00555.x.

Farquharson, C. G. and Oldenburg, D. W. (2004). A comparison of automatic techniques for estimating the regularization parameter in non-linear inverse problems. *Geophysical Journal International*, 156:411–425, doi:10.1111/j.1365–246X.2004.02190.x.

Foks, L. and Li, Y. (2014). Base of salt inversion using triangular facets. In *SEG Technical Program Expanded Abstracts 2014*, pages 1291–1296, doi:10.1190/segam2014–1598.1, Denver, CO.

Font, E., Trindade, R. I. F. d., and Nédélec, A. (2005). Detrital remanent magnetization in haematite-bearing neoproterozoic puga cap dolostone, amazon craton: a rock magnetic and sem study. *Geophysical Journal International*, 163(2):491–500.

Fontaine, F. J., Olive, J.-A., Cannat, M., Escartin, J., and Perol, T. (2011). Hydrothermally-induced melt lens cooling and segmentation along the axis of fast-and intermediate-spreading centers. *Geophysical Research Letters*, 38(14).

Fontaine, F. J. and Wilcock, W. S. (2007). Two-dimensional numerical models of open-top hydrothermal convection at high Rayleigh and Nusselt numbers: Implications for mid-ocean ridge hydrothermal circulation. *Geochemistry, Geophysics, Geosystems*, 8(7):1–17.

Forsyth, D. and Uyeda, S. (1975). On the relative importance of the driving forces of plate motion. *Geophysical Journal International*, 43(1):163–200.

Foss, C., Reed, G., Keeping, T., Wise, T., and Dutch, R. (2016). Looking into a 'blue hole' - resolving magnetization and structure from the complex negative Coompana

Anomaly, South Australia. In *ASEG-PESA-AIG 25th Expanded Abstracts 2016*, page doi: 10.1071/ASEG2016ab270, Adelaide, Australia.

Fouquet, Y., von Stackelberg, U., Charlou, J. L., Erzinger, J., Herzig, P. M., Muehe, R., and Wiedicke, M. (1993). Metallogenesis in back-arc environments; the lau basin example. *Economic Geology*, 88(8):2154–2181.

Francheteau, J., Needham, H. D., Choukroune, P., Juteau, T., Séguret, M., Ballard, R. D., Fox, P. J., Normark, W., Carranza, A., Cordoba, D., Guerrero, J., Rangin, C., Bougault, H., Cambon, P., and Hekinian, R. (1979). Massive deep-sea sulphide ore deposits discovered on the East Pacific Rise. *Nature*, 277(5697):523–528.

Fullagar, P. K., Hughes, N. A., and Paine, J. (2000). Drilling-constrained 3D gravity inversion. *Exploration Geophysics*, 31:17–23, doi:10.1071/EG00017.

Gallant, R. and Von Damm, K. (2006). Geochemical controls on hydrothermal fluids from the kairei and edmond vent fields, 23–25 s, central indian ridge. *Geochemistry, Geophysics, Geosystems*, 7(6).

Galley, A. G. (1993). Characteristics of semi-conformable alteration zones associated with volcanogenic massive sulphide districts. *Journal of Geochemical Exploration*, 48(2):175–200.

Galley, A. G., Hannington, M. D., and Jonasson, I. (2007). Volcanogenic massive sulphide deposits. *Geological Association of Canada, Mineral Deposits Division*, pages 141–161.

Galley, A. G. and Koski, R. (1999). Setting and characteristics of ophiolite-hosted volcanogenic massive sulfide deposits. *Reviews in economic geology*, 8:221–246.

Galley, C. G., Jamieson, J. W., Lelièvre, P. G., Farquharson, C. G., and Parianos, J. M. (2020). Magnetic imaging of subseafloor hydrothermal fluid circulation pathways. *Science Advances*, 6(44):eabc6844.

Galley, C. G., Lelièvre, P. G., Farquharson, C. G., and Jamieson, J. W. (2019). Modelling the subseafloor structure of seafloor massive sulphide deposits using surface geometry magnetic inversion. In *International Workshop on Gravity, Electrical & Magnetic Methods and Their Applications, Xi'an, China, May 19–22, 2019*, pages 185–188. Society of Exploration Geophysicists and Chinese Geophysical Society.

Gehrmann, R. A., North, L. J., Graber, S., Szitkar, F., Petersen, S., Minshull, T. A., and Murton, B. J. (2019). Marine Mineral Exploration With Controlled Source Electromagnetics at the TAG Hydrothermal Field, 26°N Mid-Atlantic Ridge. *Geophysical Research Letters*, pages 5808–5816.

Giannakis, I., Tsourlos, P., Papazachos, C., Vargemezis, G., Giannopoulos, A., Papadopoulos, N., Tosti, F., and Alani, A. (2019). A hybrid optimization scheme for self-potential measurements due to multiple sheet-like bodies in arbitrary 2d resistivity distributions. *Geophysical Prospecting*, 67:1948–1964.

Girdler, R. and Peter, G. (1960). An example of the importance of natural remanent magnetization in the interpretation of magnetic anomalies. *Geophysical Prospecting*, 8(3):474–483.

Glickson, D. A., Kelley, D. S., and Delaney, J. R. (2007). Geology and hydrothermal evolution of the mothra hydrothermal field, endeavour segment, juan de fuca ridge. *Geochemistry, Geophysics, Geosystems*, 8(6).

Graber, S., Petersen, S., Yeo, I., Szitkar, F., Klischies, M., Jamieson, J., Hannington, M., Rothenbeck, M., Wenzlaff, E., Augustin, N., et al. (2020). Structural control, evolution, and accumulation rates of massive sulfides in the tag hydrothermal field. *Geochemistry, Geophysics, Geosystems*, page e2020GC009185.

Grant, H. L., Hannington, M. D., Petersen, S., Frische, M., and Fuchs, S. H. (2018). Constraints on the behavior of trace elements in the actively-forming tag deposit, mid-atlantic ridge, based on la-icp-ms analyses of pyrite. *Chemical Geology*, 498:45–71.

Green, D. and Ringwood, A. (1963). Mineral assemblages in a model mantle composition. *Journal of Geophysical Research*, 68(3):937–945.

Griffiths, D. J. (2005). Introduction to electrodynamics.

Guigue, P. and Devillers, O. (2003). Fast and robust triangle-triangle overlap test using orientation predicates. *Journal of Graphics Tools*, 8:25–32.

Hannington, M., Jamieson, J., Monecke, T., Petersen, S., and Beaulieu, S. (2011). The abundance of seafloor massive sulfide deposits. *Geology*, 39(12):1155–1158.

Hannington, M. D., de Ronde, C. D., and Petersen, S. (2005a). Sea-floor tectonics and submarine hydrothermal systems. Society of Economic Geologists.

Hannington, M. D., de Ronde, C. E. J., and Petersen, S. (2005b). Sea-floor tectonics and submarine hydrothermal systems. *Economic Geology 100th Anniversary Volume*, pages 111–141.

Hannington, M. D., Galley, A. G., Herzig, P., and Petersen, S. (1998). Comparison of the tag mound and stockwork complex with cyprus-type massive sulfide deposits. In *Proceedings of the Ocean Drilling Program: Scientific Results*, volume 158, pages 389–415.

Hannington, M. D., Jamieson, J., Monecke, T., and Petersen, S. (2010). Modern sea-floor massive sulfides and base metal resources: toward an estimate of global sea-floor massive sulfide potential. Society of Economic Geologists.

Hannington, M. D., Jonasson, I. R., Herzig, P. M., and Petersen, S. (1995). Physical and chemical processes of seafloor mineralization at mid-ocean ridges. *Seafloor hydrothermal systems: Physical, chemical, biological, and geological interactions*, pages 115–157.

Hansen, P. C. and O'Leary, D. P. (1993). The use of the L-curve in the regularization of discrete ill-posed problems. *SIAM journal on scientific computing*, 14:1487–1503.

Hansen, R., Racic, L., and Grauch, V. (2005). Magnetic methods in near-surface geophysics. In *Near-surface geophysics*, pages 151–176. Society of Exploration Geophysicists.

Haroon, A., Hölz, S., Gehrmann, R. A., Attias, E., Jegen, M., Minshull, T. A., and Murton, B. J. (2018). Marine dipole-dipole controlled source electromagnetic and coincident-loop transient electromagnetic experiments to detect seafloor massive sulphides: Effects of three-dimensional bathymetry. *Geophysical Journal International*, 215(3):2156–2171.

Hasenclever, J., Theissen-Krah, S., Rüpke, L. H., Morgan, J. P., Iyer, K., Petersen, S., and Devey, C. W. (2014). Hybrid shallow on-axis and deep off-axis hydrothermal circulation at fast-spreading ridges. *Nature*, 508(7497):508–512.

Herzig, P. M. and Hannington, M. D. (1995). Polymetallic massive sulfides at the modern seafloor a review. *Ore Geology Reviews*, 10(2):95 – 115.

Hidalgo-Gato, M. C. and Barbosa, V. C. (2019). Fast 3D magnetic inversion of a surface relief in the space domain. *Geophysics*, 84:J57–J67.

Hillier, M. J., Schetselaar, E. M., de Kemp, E. A., and Perron, G. (2014). Three-dimensional modelling of geological surfaces using generalized interpolation with radial basis functions. *Mathematical Geosciences*, 46:931–953, doi:10.1007/s11004–014–9540–3.

Hobro, J. W. D. and Rickett, J. E. (2014). Explicit high-contrast surface refinement using full waveform inversion. In *EAGE 76th Expanded Abstracts 2014*, pages 10.3997/2214–4609.20140705, Amsterdam, Netherlands.

Honsho, C., Ura, T., and Kim, K. (2013). Deep-sea magnetic vector anomalies over the Hakurei hydrothermal field and the Bayonnaise knoll caldera, Izu-Ogasawara arc, Japan. *Journal of Geophysical Research: Solid Earth*, 118(10):5147–5164.

Hrouda, F. and Kapička, A. (1986). The effect of quartz on the magnetic anisotropy of quartzite. *Studia Geophysica et Geodaetica*, 30(1):39–45.

Humphris, S. E., Alt, J. C., Teagle, D. A., and Honnorez, J. J. (1998). Geochemical changes during hydrothermal alteration of basement in the stockwork beneath the active TAG hydrothermal mound. *Proceedings of the Ocean Drilling Program: Scientific Results*, 158:255–276.

Humphris, S. E., Herzig, P., Miller, D., Alt, J., Becker, K., Brown, D., Brügmann, G., Chiba, H., Fouquet, Y., Gemmell, J., Guerin, G., MD, H., Holm, N., Honnorez, J., Iturrino, G., Knott, R., Ludwig, R., Nakamura, K., Petersen, S., Reysenbach, A., Rona, P., Smith, S., Sturz, A., Tivey, M., and Zhao, X. (1995). The internal structure of an active sea-floor massive sulphide deposit. *Nature*, 377:713.

Humphris, S. E. and Tivey, M. K. (2000). A synthesis of geological and geochemical investigations of the tag hydrothermal field: Insights into fluid-flow and mixing processes in a hydrothermal system. *Special Papers-Geological Society of America*, pages 213–236.

Hüneke, H. and Mulder, T. (2011). Deep-sea sediments. *Developments in sedimentology.*

Huston, D. L., Pehrsson, S., Eglington, B. M., and Zaw, K. (2010). The geology and metallogeny of volcanic-hosted massive sulfide deposits: Variations through geologic time and with tectonic setting. *Economic Geology*, 105(3):571–591.

Irving, E. (1970). The Mid-Atlantic Ridge at 45° N. XIV. Oxidation and magnetic properties of basalt; review and discussion. *Canadian Journal of Earth Sciences*, 7(6):1528–1538.

Isezaki, N. (1986). A new shipboard three-component magnetometer. *Geophysics*, 51(10):1992–1998.

Jacobs, A. M., Harding, A. J., and Kent, G. M. (2007). Axial crustal structure of the Lau back-arc basin from velocity modeling of multichannel seismic data. *Earth and Planetary Science Letters*, 259(3-4):239–255.

Jahandari, H. and Farquharson, C. (2014). A finite-volume solution to the geophysical electromagnetic forward problem using unstructured grids. *Geophysics*, 79:E287–E302, doi:10.1190/geo2013–0312.1.

Jahandari, H. and Farquharson, C. G. (2013). Forward modeling of gravity data using finite-volume and finite-element methods on unstructured grids. *Geophysics*, 78:G69–G80, doi:10.1190/GEO2012–0246.1.

Jahandari, H. and Farquharson, C. G. (2017). 3-D minimum-structure inversion of magnetotelluric data using the finite-element method and tetrahedral grids. *Geophysical Journal International*, 211:1211–1227, doi:10.1093/gji/ggx358.

Jamieson, J. W., Clague, D. A., and Hannington, M. D. (2014a). Hydrothermal sulfide accumulation along the Endeavour Segment, Juan de Fuca Ridge. *Earth and Planetary Science Letters*, 395:136–148.

Jamieson, J. W., Hannington, M. D., Petersen, S., and Tivey, M. K. (2014b). Encyclopedia of Marine Geosciences. *Encyclopedia of Marine Geosciences*, pages 1–9.

Janecky, D. and Seyfried, W. (1984). Formation of massive sulfide deposits on oceanic ridge crests: Incremental reaction models for mixing between hydrothermal solutions and seawater. *Geochimica et Cosmochimica Acta*, 48(12):2723 – 2738.

Javaheri Koupaei, A. H. (2012). Numerical modelling and inversion of borehole induced polarization data. Master's thesis, Memorial University of Newfoundland, St. John's, Newfoundland, Canada.

Johnson, H. P. and Hall, J. M. (1978). A detailed rock magnetic and opaque mineralogy study of the basalts from the nazca plate. *Geophysical Journal International*, 52(1):45–64.

Johnson, H. P. and Pariso, J. E. (1987). The effects of hydrothermal alteration on the magnetic properties of oceanic crust: results from drill holes cy-2 and cy-2a, cyprus crustal study project. In *Cyprus Crustal Study Project: Initial Reports, Holes CY2 and 2a*, volume 85, pages 283–293. Geological Survey of Canada Paper.

Johnson, H. P., Tivey, M. A., Bjorklund, T. A., and Salmi, M. S. (2010). Hydrothermal circulation within the endeavour segment, juan de fuca ridge. *Geochemistry, Geophysics, Geosystems*, 11(5):1–13.

Kelley, D. S., Karson, J. A., Blackman, D. K., FruÈh-Green, G. L., Butterfield, D. A., Lilley, M. D., Olson, E. J., Schrenk, M. O., Roe, K. K., Lebon, G. T., et al. (2001). An off-axis hydrothermal vent field near the mid-atlantic ridge at 30 n. *Nature*, 412(6843):145–149.

Kikawa, E. and Pariso, J. E. (1991). 16. magnetic properties of gabbros from hole 735b, southwest indian ridge1. In *Proceedings of the Ocean Drilling Program: Scientific results*, page 285. The Program.

Klein, F., Bach, W., Humphris, S. E., Kahl, W. A., Jöns, N., Moskowitz, B., and Berquó, T. S. (2014). Magnetite in seafloor serpentinite-Some like it hot. *Geology*, 42(2):135–138.

Knott, R., Fouquet, Y., Honnorez, J., Petersen, S., and Bohn, M. (1998a). Petrology of hydrothermal mineralization: a vertical section through the tag mound. In *Proceedings of the Ocean Drilling Program: Scientific Results*, volume 158, pages 5–26.

Knott, R., Fouquet, Y., Honnorez, J., Petersen, S., Bohn, M., and Herzig, P. (1998b). Petrology of hydrothermal mineralization: a vertical section through the tag mound. In *Proc Ocean Drill Program Sci Results*, pages 5–26. National Science Foundation.

Kobayashi, K. (1959). Chemical remanent magnetization of ferromagnetic minerals and its application to rock magnetism. *Journal of geomagnetism and geoelectricity*, 10(3):99–117.

Koops, J. P. (2011). Travel-time seismic inversion for a numerically-defined shape. Master's thesis, Memorial University of Newfoundland.

Kowalczyk, P. (2008). Geophysical prelude to first exploitation of submarine massive sulphides. *First Break*, 26(11).

Kowalczyk, P. (2011). Geophysical exploration for submarine massive sulfide deposits. *OCEANS'11 - MTS/IEEE Kona, Program Book*.

Krahenbuhl, R. A. and Li, Y. (2009). Hybrid optimization for lithologic inversion and time-lapse monitoring using a binary formulation. *Geophysics*, 74:I55–I65.

Kwisanga, C. (2016). *SQUID geomagnetic signal analysis and modelling of Schumann Resonances in the earth-ionosphere cavity*. PhD thesis, Stellenbosch: Stellenbosch University.

Lajaunie, C., Courrioux, G., and Manuel, L. (1997). Foliation fields and 3D cartography in geology: principles of a method based on potential interpolation. *Mathematical Geology*, 29:571–584.

Last, B. J. and Kubik, K. (1983). Compact gravity inversion. *Geophysics*, 48:713–721, doi:10.1190/1.1441501.

Le Bas, M. and Streckeisen, A. L. (1991). The iugs systematics of igneous rocks. *Journal of the Geological Society*, 148(5):825–833.

Lelièvre, P., Carter-McAuslan, A., Farquharson, C., and Hurich, C. (2012). Unified geophysical and geological 3d earth models. *The Leading Edge*, 31(3):322–328.

Lelièvre, P. G., Carter-McAuslan, A. E., Dunham, M. W., Jones, D. J., Nalepa, M., Squires, C. L., Tycholiz, C. J., Vallée, M. A., and Farquharson, C. G. (2018). FacetModeller: Software for manual creation, manipulation and analysis of 3D surface-based models. *SoftwareX*, 7:41–46, doi:10.1016/j.softx.2018.02.002.

Lelièvre, P. G., Carter-McAuslan, A. E., Dunham, M. W., Jones, D. J., Nalepa, M., Squires, C. L., Tycholiz, C. J., Vallée, M. A., and Farquharson, C. G. (2018). FacetModeller: Software for manual creation, manipulation and analysis of 3D surface-based models. *SoftwareX*, 7:41–46.

Lelièvre, P. G. and Farquharson, C. G. (2013). Gradient and smoothness regularization operators for geophysical inversion on unstructured meshes. *Geophysical Journal International*, 195(1):330–341.

Lelièvre, P. G. and Farquharson, C. G. (2013). Gradient and smoothness regularization operators for geophysical inversion on unstructured meshes. *Geophysical Journal International*, 195:330–341, doi:10.1093/gji/ggt255.

Lelièvre, P. G., Farquharson, C. G., and Bijani, R. (2015). 3D potential field inversion for wireframe surface geometry. In *SEG Technical Program Expanded Abstracts 2015*, pages 1563–1567, doi:10.1190/segam2015–5873054.1.

Lelièvre, P. G., Farquharson, C. G., and Butler, K. E. (2016). Inversion for wireframe surface geometry applied to the Cocagne Subbasin, New Brunswick, Canada. In *SEG Technical Program Expanded Abstracts 2016*, pages 1617–1621, doi:10.1190/segam2016–13516511.1, Dallas.

Lelièvre, P. G., Farquharson, C. G., and Hurich, C. A. (2011). Inversion of first-arrival seismic traveltimes without rays, implemented on unstructured grids. *Geophysical Journal International*, 185:749–763.

Lelièvre, P. G. and Oldenburg, D. W. (2009). A 3D total magnetization inversion applicable when significant, complicated remanence is present. *Geophysics*, 74(3).

Letouzey, J. and Kimura, M. (1985). Okinawa trough genesis: structure and evolution of a backarc basin developed in a continent. *Marine and Petroleum Geology*, 2(2):111–130.

Levi, S. and Riddihough, R. (1986). Why are marine magnetic anomalies suppressed over sedimented spreading centers? *Geology*, 14(8):651–654.

Li, M., Abubakar, A., Habashy, T. M., and Zhang, Y. (2010). Inversion of controlled-source electromagnetic data using a model-based approach. *Geophysical Prospecting*, 58:455–467.

Li, W., Lu, W., Qian, J., and Li, Y. (2017). A multiple level-set method for 3D inversion of magnetic data. *Geophysics*, 82:J61–J81, doi:10.1190/GEO2016–0530.1.

Li, Y. and Oldenburg, D. W. (1996). 3D inversion of magnetic data. *Geophysics*, 61:394–408.

Li, Y. and Oldenburg, D. W. (1998a). 3-d inversion of gravity data. *Geophysics*, 63:109–119.

Li, Y. and Oldenburg, D. W. (1998b). Separation of regional and residual magnetic field data. *Geophysics*, 63(2):431–439.

Li, Y. and Oldenburg, D. W. (2000). Joint inversion of surface and three-component borehole magnetic data. *Geophysics*, 65:540–552.

Lines, L. and Treitel, S. (1984). A review of least-squares inversion and its application to geophysical problems. *Geophysical prospecting*, 32(2):159–186.

Lipton, I. (2012). *Mineral Resource Estimate, Solwara Project, Bismarck Sea, PNG.* Number March in 1. Canadian NI43-101 technical report for Nautilus Minerals Inc., golder res edition.

Liu, E. H., Lamontagne, Y., Oristaglio, M., and Spies, B. (1999). Electromagnetic modeling with surface integral equations. *Three-dimensional electromagnetics: SEG*, pages 76–89.

Liu, Q., Roberts, A. P., Rohling, E. J., Zhu, R., and Sun, Y. (2008). Post-depositional remanent magnetization lock-in and the location of the matuyama–brunhes geomagnetic reversal boundary in marine and chinese loess sequences. *Earth and Planetary Science Letters*, 275(1-2):102–110.

Lu, X., Lelièvre, P., and Farquharson, C. G. (2020). Surface geometry inversion of time-domain em data. In *SEG Technical Program Expanded Abstracts 2020*, pages 1399–1403. Society of Exploration Geophysicists.

Ludwig, R. J., Iturrino, G. J., and Rona, P. A. (1998). 23. seismic velocity-porosity relationship of sulfide, sulfate, and basalt samples from the tag hydrothermal mound. *Proceedings of the Ocean Drilling Program, Scientific Results; Texas A & M University: College Station, TX, USA*, 158:313–328.

Luyendyk, A. (1997). Processing of airborne magnetic data. *AGSO Journal of Australian Geology and Geophysics*, 17:31–38.

Maffione, M., Morris, A., Plümper, O., and van Hinsbergen, D. J. (2014). Magnetic properties of variably serpentinized peridotites and their implication for the evolution of oceanic core complexes. *Geochemistry, Geophysics, Geosystems*, 15(4):923–944.

Mallesh, K., Chakravarthi, V., and Ramamma, B. (2019). 3D gravity analysis in the spatial domain: model simulation by multiple polygonal cross-sections coupled with exponential density contrast. *Pure and Applied Geophysics*, 176:2497–2511, doi:10.1007/s00024–019–02103–9.

Marshall, M. and Cox, A. (1972). Magnetic changes in pillow basalt due to sea floor weathering. *Journal of Geophysical Research*, 77(32):6459–6469.

Martinez, F. and Taylor, B. (1996). Backarc spreading, rifting, and microplate rotation, between transform faults in the Manus Basin. *Marine Geophysical Research*, 18(2-4):203–224.

McMillan, M. S., Schwarzbach, C., Oldenburg, D. W., and Haber, E. (2014). Recovering a thin dipping conductor with 3D electromagnetic inversion over the Caber deposit. In *SEG Technical Program Expanded Abstracts 2014*, pages 1720–1724, doi:10.1190/segam2014–0536.1, Denver, CO.

Michelini, A. (1993). Velocity model inversion using parametric curves. *Geophysical Journal International*, 115:337–343, doi:10.1111/j.1365–246X.1993.tb01190.x.

Michelini, A. (1995). An adaptive-grid formalism for traveltime tomography. *Geophysical Journal International*, 121:489–510, doi:10.1111/j.1365–246X.1995.tb05728.x.

Miller, G. L., Talmor, D., Teng, S., Walkington, N., and Wang, H. (1996). Control volume meshes using sphere packing: Generation, refinement and coarsening. *Proceedings of the 5th International Meshing Roundtable, Sandia National Laboratories*, pages 47–61.

Möller, T. (1997). A fast triangle-triangle intersection test. *Journal of Graphics Tools*, 2:25–30.

Moorkamp, M., Lelièvre, P. G., Linde, N., and Khan, A., editors (2016). *Integrated Imaging of the Earth: Theory and Applications*. Geophysical Monograph Series, American Geophysical Union. John Wiley & Sons, Inc., Hoboken, New Jersey, doi:10.1002/9781118929063.

Moss, R., Scott, S. D., and Binns, A. R. (2001). Gold content of eastern Manus basin volcanic rocks: Implications for enrichment in associated hydrothermal precipitates. *Economic Geology*, 96(1):91–107.

Müller, H., von Dobeneck, T., Hilgenfeldt, C., SanFilipo, B., Rey, D., and Rubio, B. (2012). Mapping the magnetic susceptibility and electric conductivity of marine surficial sediments by benthic em profiling. *Geophysics*, 77(1):E43–E56.

Murton, B. J., Lehrmann, B., Dutrieux, A. M., Martins, S., de la Iglesia, A. G., Stobbs, I. J., Barriga, F. J., Bialas, J., Dannowski, A., Vardy, M. E., North, L. J., Yeo, I. A., Lusty, P. A., and Petersen, S. (2019). Geological fate of seafloor massive sulphides at the TAG hydrothermal field (Mid-Atlantic Ridge). *Ore Geology Reviews*, 107(October 2018):903–925.

Narasimha Rao, B., Ramakrishna, P., and Markandeyulu, A. (1995). GMINV: a computer program for gravity or magnetic data inversion. *Computers and Geosciences*, 21:301–319, doi:10.1016/0098–3004(94)00074–5.

Nehlig, P. and Juteau, T. (1988). Flow porosities, permeabilities and preliminary data on fluid inclusions and fossil thermal gradients in the crustal sequence of the Sumail ophiolite (Oman). *Tectonophysics*, 151(1-4):199–221.

Nishiyama, R., Ariga, A., Ariga, T., Käser, S., Lechmann, A., Mair, D., Scampoli, P., Vladymyrov, M., Ereditato, and Schlunegger, F. (2017). First measurement of ice bedrock interface of alpine glaciers by cosmic muon radiography. *Geophysical Research Letters*, 44:6244–6251, doi:10.1002/2017GL073599.

Ohmoto, H. (1996). Formation of volcanogenic massive sulfide deposits: the kuroko perspective. *Ore Geology Reviews*, 10(3-6):135–177.

Okabe, M. (1979). Analytic expressions for gravity anomalies due to homogeneous polyhedral bodies and translations into magnetic anomalies. *Geophysics*, 44:730–741.

Oldenburg, D. W. and Pratt, D. A. (2007). Geophysical inversion for mineral exploration: a decade of progress in theory and practice. In Milkereit, B., editor, *Proceedings of Exploration 07: Fifth Decennial International Conference on Mineral Exploration*, pages 61–95.

Oliveira, V. C., Barbosa, V. C. F., and Silva, J. B. C. (2011). Source geometry estimation using the mass excess criterion to constrain 3-D radial inversion of gravity data. *Geophysical Journal International*, 187:754–772, doi:10.1111/j.1365–246X.2011.05172.x.

Oliveira, Jr., V. C. and Barbosa, V. C. F. (2013). 3-D radial gravity gradient inversion. *Geophysical Journal International*, 195:883–902, doi:10.1093/gji/ggt307.

O'Reilly, W. and Banerjee, S. K. (1967). The mechanism of oxidation in titanomagnetites: a magnetic study. *Mineralogical Magazine and Journal of the Mineralogical Society*, 36(277):29–37.

Orlický, O. (2010). Magnetism and magnetic properties of Ti-rich titanomagnetite and its tendency for alteration in favour of titanomaghemite. *Contributions to Geophysics and Geodesy*, 40(1):65–86.

Oshida, A., Tamaki, K., and Kimura, M. (1992). Origin of the magnetic anomalies in the southern okinawa trough. *Journal of geomagnetism and geoelectricity*, 44(5):345–359.

Ozima, M. and Larson, E. (1970). Low-and high-temperature oxidation of titanomagnetite in relation to irreversible changes in the magnetic properties of submarine basalts. *Journal of Geophysical Research*, 75(5):1003–1017.

Paasche, H. (2016). Post-inversion integration of disparate tomographic models by model structure analyses. *Integrated imaging of the earth: theory and applications. Wiley*, pages 69–91.

Paasche, H. and Tronicke, J. (2014). Nonlinear joint inversion of tomographic data using swarm intelligence. *Geophysics*, 79:R133–R149, doi:10.1190/GEO2013–0423.1.

Pallero, J. L. G., Fernández-Martínez, J. L., Bonvalot, S., and Fudym, O. (2015). Gravity inversion and uncertainty assessment of basement relief via Particle Swarm Optimization. *Journal of Applied Geophysics*, 116:180–191, doi:10.1016/j.jappgeo.2015.03.008.

Park, A. F. (1990). *Mid-ocean ridge and ocean-floor petrology*, pages 367–373. Springer US, Boston, MA.

Parker, R. and Huestis, S. (1974). The inversion of magnetic anomalies in the presence of topography. *Journal of Geophysical Research*, 79(11):1587–1593.

Pellerin, J., Botella, A., Bonneau, F., Mazuyer, A., Chauvin, B., Lévy, B., and Caumon, G. (2017). RINGMesh: A programming library for developing mesh-based geomodeling applications. *Computers and Geosciences*, 104:93–100.

Pellerin, J., Lévy, B., Caumon, G., and Botella, A. (2014). Automatic surface remeshing of 3D structural models at specified resolution: A method based on voronoi diagrams. *Computers and Geosciences*, 62:103–116.

Peng, M., Tan, H., and Moorkamp, M. (2019). Structure-coupled 3D imaging of magnetotelluric and wide-angle seismic reflection/refraction data with interfaces. *Journal of Geophysical Research: Solid Earth*, 124:10309–10330.

Pereyra, V. (1996). Modeling, ray tracing, and block nonlinear travel-time inversion in 3D. *Pure and Applied Geophysics*, 148:345–386, doi:10.1007/BF00874572.

Peters, J. and Reif, U. (2008). *Subdivision Surfaces*, volume 3 of *Geometry and Computing*. Springer-Verlag Berlin Heidelberg.

Petersen, N., Eisenach, P., and Bleil, U. (1979). Low temperature alteration of the magnetic minerals in ocean floor basalts. *Deep drilling results in the Atlantic ocean: Ocean crust*, 2:169–209.

Petersen, S. (2016). Rv meteor fahrtbericht/cruise report m127 metal fluxes and resource potential at the slow-spreading tag midocean ridge segment (26° n, mar)–blue mining@ sea, bridgetown (barbados)–ponta delgada (portugal), 25.05.-28.06. 2016 (extended version). *Cruise Report*.

Petersen, S., Herzig, P., and Hannington, M. D. (2000). Third dimension of a presently forming vms deposit: Tag hydrothermal mound, mid-atlantic ridge, 26 n. *Mineralium Deposita*, 35(2-3):233–259.

Petersen, S., Krätschell, A., Augustin, N., Jamieson, J., Hein, J. R., and Hannington, M. D. (2016). News from the seabed–geological characteristics and resource potential of deep-sea mineral resources. *Marine Policy*, 70:175–187.

Piercey, S. J. (2011). The setting, style, and role of magmatism in the formation of volcanogenic massive sulfide deposits. *Mineralium Deposita*, 46(5):449–471.

Pilkington, M. (2006). Joint inversion of gravity and magnetic data for two-layer models. *Geophysics*, 71:L35–L42, doi:10.1190/1.2194514.

Pontbriand, C. and Sohn, R. (2014). Microearthquake evidence for reaction-driven cracking within the Trans-Atlantic Geotraverse active hydrothermal deposit. *AGU: Journal of Geophysical Research, Solid Earth*, 120:1195–1209.

Portniaguine, O. and Zhdanov, M. S. (1999). Focusing geophysical inversion images. *Geophysics*, 64:874–887, doi:10.1190/1.1444596.

Purdy, G., Kong, L., Christeson, G., and Solomon, S. (1992). Relationship between spreading rate and the seismic structure of mid-ocean ridges. *Nature*, 355(February):815–817.

Rawlinson, N., Houseman, G. A., and Collins, C. D. N. (2001). Inversion of seismic refraction and wide-angle reflection traveltimes for three-dimensional layered crustal structure. *Geophysical Journal International*, 145:381–400, doi:10.1046/j.1365–246X.2001.01383.x.

Rawlinson, N. and Sambridge, M. (2003). Irregular interface parametrization in 3-D wide-angle seismic traveltime tomography. *Geophysical Journal International*, 155:79–92, doi:10.1046/j.1365–246X.2003.01983.x.

Readman, P. and O'Reilly, W. (1972). Magnetic properties of oxidized (cation-deficient) titanomagnetites (fe, ti, _?? _) 43o4. *Journal of geomagnetism and geoelectricity*, 24(1):69–90.

Renaudeau, J., Malvesin, E., Maerten, F., and Caumon, G. (2019). Implicit structural modeling by minimization of the bending energy with moving least squares functions. *Mathematical Geosciences*, 51:693–724, doi:10.1007/s11004–019–09789–6.

René, R. (1986). Gravity inversion using open, reject, and "shape-of-anomaly" fill criteria. *Geophysics*, 51:988–994.

Richardson, R. M. and MacInnes, S. C. (1989). The inversion of gravity data into three-dimensional polyhedral models. *Journal of Geophysical Research: Solid Earth*, 94:7555–7562, doi:10.1029/JB094iB06p07555.

Ridge, P. M.-o. (2001). Mid-ocean ridge tectonics, volcanism and geomorphology. *Geology*, 26(455):458.

Rona, P. A., Davis, E. E., and Ludwig, R. J. (1998). Thermal properties of tag hydrothermal precipitates, mid-atlantic ridge, and comparison with middle valley, juan de fuca ridge. In *PROCEEDINGS-OCEAN DRILLING PROGRAM SCIENTIFIC RESULTS*, pages 329–336. NATIONAL SCIENCE FOUNDATION.

Rona, P. A., Harbison, R. N., Bassinger, B. G., Scott, R. B., and Nalwalk, A. J. (1976). Tectonic fabric and hydrothermal activity of mid-atlantic ridge crest (lat 26 n). *Geological Society of America Bulletin*, 87(5):661–674.

Rona, P. A. and Scott, S. D. (1993). A special issue on sea-floor hydrothermal mineralization; new perspectives; preface. *Economic Geology*, 88(8):1935–1976.

Roy, L., Sen, M. K., McIntosh, K., Stoffa, P. L., and Nakamura, Y. (2005). Joint inversion of first arrival seismic travel-time and gravity data. *Journal of Geophysical Engineering*, 2:277–289.

Ruiu, J., Caumon, G., and Viseur, S. (2016). Modeling channel forms and related sedimentary objects using a boundary representation based on Non-uniform Rational B-Splines. *Mathematical Geosciences*, 48:259–284: doi:10.1007/s11004–015–9629–3.

Sabharwal, C. and Leopold, J. (2015). A triangle-triangle intersection algorithm. In *7th International Conference on Wireless & Mobile Networks*, volume 5.

Sasagawa, G. S., Crawford, W., Eiken, O., Nooner, S., Stenvold, T., and Zumberge, M. A. (2003). A new sea-floor gravimeter. *Geophysics*, 68(2):544–553.

Scalzo, R., Kohn, D., Olierook, H., Houseman, G., Chandra, R., Girolami, M., and Cripps, S. (2019). Efficiency and robustness in monte carlo sampling for 3D geophysical inversions with obsidian v0. 1.2: setting up for success. *Geoscientific Model Development*, 12:2941–2960.

Schmidt, V., Günther, D., and Hirt, A. M. (2006). Magnetic anisotropy of calcite at room-temperature. *Tectonophysics*, 418(1-2):63–73.

Schnaidt, S., Conway, D., Krieger, L., and Heinson, G. (2018). Pareto-optimal multi-objective inversion of geophysical data. *Pure and Applied Geophysics*, 175:2221–2236.

Seama, N., Nogi, Y., and Isezaki, N. (1993). A new method for precise determination of the position and strike of magnetic boundaries using vector data of the geomagnetic anomaly field. *Geophysical Journal International*, 113(1):155–164.

Seewald, J. S., Reeves, E. P., Bach, W., Saccocia, P. J., Craddock, P. R., Walsh, E., Shanks, W. C., Sylva, S. P., Pichler, T., and Rosner, M. (2019). Geochemistry of hot-springs at the SuSu Knolls hydrothermal field, Eastern Manus Basin: Advanced argillic alteration and vent fluid acidity. *Geochimica et Cosmochimica Acta*, 255:25–48.

Sempere, J.-C., Meshkov, A., Thommeret, M., and Macdonald, K. (1988). Magnetic properties of some young basalts from the east pacific rise. *Marine geophysical researches*, 9(2):131–146.

Seyfried, W. and Bischoff, J. L. (1981). Experimental seawater-basalt interaction at 300 c, 500 bars, chemical exchange, secondary mineral formation and implications for the transport of heavy metals. *Geochimica et Cosmochimica Acta*, 45(2):135–147.

Sharma, P. V. (1997). *Environmental and engineering geophysics*. Cambridge university press.

Shau, Y.-H., Torii, M., Horng, C.-S., Liang, W.-T., et al. (2004). Magnetic properties of mid-oceanridge basalts from ocean drilling program leg 187. In *Proc. ODP, Sci. Results*, volume 187. ODP.

Shewchuk, J. R. (1996). Triangle: Engineering a 2D quality mesh generator and delaunay triangulator. *Lecture Notes in Computer Science (including subseries Lecture Notes in Artificial Intelligence and Lecture Notes in Bioinformatics)*, 1148(February 1970):203–222.

Shewchuk, J. R. (2003). Triangle: a two-dimensional quality mesh generator and delaunay triangulator, http://www.cs.cmu.edu/~quake/triangle.html, last accessed November 2017.

Shinohara, M., Yamada, T., Ishihara, T., Araya, A., Kanazawa, T., Fujimoto, H., Uehira, K., Tsukioka, S., Omika, S., and Iizasa, K. (2015). Development of an underwater gravity measurement system using autonomous underwater vehicle for exploration of seafloor deposits. In *OCEANS 2015-Genova*, pages 1–7. IEEE.

Si, H. (2015). TetGen, a delaunay-based quality tetrahedral mesh generator. *ACM Transactions on Mathematical Software*, 41(2).

Si, H. (2017). TetGen: a quality tetrahedral mesh generator and a 3D delaunay triangulator, http://wias-berlin.de/software/tetgen/, last accessed November 2017.

Siegburg, M., Klügel, A., Rocholl, A., and Bach, W. (2018). Magma plumbing and hybrid magma formation at an active back-arc basin volcano: North Su, eastern Manus basin. *Journal of Volcanology and Geothermal Research*, 362:1–16.

Sinton, J. M. and Detrick, R. S. (1992). Mid-ocean ridge magma chambers. *Journal of Geophysical Research*, 97(B1):197–216.

Smith, S. E. and Humphris, S. E. (1998). 17. geochemistry of basaltic rocks from the tag hydrothermal mound (26 08′ n), mid-atlantic ridge1. In *Proceedings of the ocean drilling program, scientific results*, volume 158, pages 213–229.

Smith, T., Hoversten, M., Gasperikova, E., and Morrison, F. (1999). Sharp boundary inversion of 2D magnetotelluric data. *Geophysical Prospecting*, 47:469–486, doi:10.1046/j.1365–2478.1999.00145.x.

Song, L., Pasion, L. R., Billings, S. D., and Oldenburg, D. W. (2011). Nonlinear inversion for multiple objects in transient electromagnetic induction sensing of unexploded ordnance: Technique and applications. *IEEE Transactions on Geoscience and Remote Sensing*, 49:4007–4020, doi:10.1109/TGRS.2011.2132138.

Spagnoli, G., Hannington, M., Bairlein, K., Hördt, A., Jegen, M., Petersen, S., and Laurila, T. (2016). Electrical properties of seafloor massive sulfides. *Geo-Marine Letters*, 36(3):235–245.

Stacey, F. (2012). *The physical principles of rock magnetism*. Number 5 in 1. Elsevier.

Sun, J. and Li, Y. (2015). Multidomain petrophysically constrained inversion and geology differentiation using guided fuzzy c-means clustering. *GEOPHYSICS*, 80:ID1–ID18.

Szitkar, F. and Dyment, J. (2015). Near-seafloor magnetics reveal tectonic rotation and deep structure at the TAG (Trans-Atlantic Geotraverse) hydrothermal site (Mid-Atlantic Ridge, 26°N). *Geology*, 43(1):87–90.

Szitkar, F., Dyment, J., Choi, Y., and Fouquet, Y. (2014a). What causes low magnetization at basalt-hosted hydrothermal sites? Insights from inactive site Krasnov (MAR 16°38′N). *Geochemistry, Geophysics, Geosystems*, 15(4):1441–1451.

Szitkar, F., Dyment, J., Fouquet, Y., Honsho, C., and Horen, H. (2014b). The magnetic signature of ultramafic-hosted hydrothermal sites. *Geology*, 42(8):715–718.

Szitkar, F. and Murton, B. J. (2018). Near-seafloor magnetic signatures unveil serpentinization dynamics at ultramafic-hosted hydrothermal sites. *Geology*, 46(12):1055–1058.

Tanner, J. G. (1967). An automated method of gravity interpretation. *Geophysical Journal of the Royal Astronomical Society*, 13:339–347, doi:10.1111/j.1365–246X.1967.tb02164.x.

Taylor, B. (1979). Bismarck sea: Evolution of a back-arc basin. *Geology*, 7(4):171–174.

Team, F. S. et al. (1993). Rock and water sampling of the mid-atlantic ridge from 32-41$^{\mathrm{o}}$n: objectives and a new vent site. *EOS Transactions American Geophysical Union*, 74:380.

Telford, W. M., Telford, W., Geldart, L., Sheriff, R. E., and Sheriff, R. E. (1990). *Applied geophysics*. Cambridge university press.

Thal, J., Tivey, M., Yoerger, D. R., and Bach, W. (2016). Subaqueous cryptodome eruption, hydrothermal activity and related seafloor morphologies on the andesitic North Su volcano. *Journal of Volcanology and Geothermal Research*, 323:80–96.

Theissen-Krah, S., Rüpke, L. H., and Hasenclever, J. (2016). Modes of crustal accretion and their implications for hydrothermal circulation. *Geophysical Research Letters*, 43(3):1124–1131.

Tikhonov, A. N. and Arsenin, V. Y. (1977). Solutions of ill-posed problems. *New York*, 1:30.

Titus, W. J., Titus, S. J., and Davis, J. R. (2017). A Bayesian approach to modeling 2D gravity data using polygons. *Geophysics*, 82:G1–G21, doi:10.1190/GEO2016–0153.1.

Tivey, M. A., Bach, W., Seewald, J. S., Tivey, M. K., and Vanko, D. (2006). Hydrothermal Systems in the Eastern Manus Basin: Fluid Chemistry and Magnetic Structure as Guides to Subseafloor Processes. *R/V Melville Cruise Report*.

Tivey, M. A. and Johnson, P. H. (2002). Crustal magnetization reveals subsurface structure of Juan de Fuca Ridge hydrothermal vent fields. *Geology*, 30(11):979–982.

Tivey, M. A., Rona, P. A., and Schouten, H. (1993). Reduced crustal magnetization beneath the active sulfide mound, tag hydrothermal field, mid-atlantic ridge at 26 n. *Earth and planetary science letters*, 115(1-4):101–115.

Tivey, M. A., Schouten, H., and Kleinrock, M. C. (2003). A near-bottom magnetic survey of the Mid-Atlantic Ridge axis at 26°N: Implications for the tectonic evolution of the TAG segment. *Journal of Geophysical Research: Solid Earth*, 108(B5):1–13.

Tlas, M. and Asfahani, J. (2015). The simplex algorithm for best-estimate of magnetic parameters related to simple geometric-shaped structures. *Mathematical Geosciences*, 47:301–316, doi:10.1007/s11004–014–9549–7.

Tregoning, P. (2002). Plate kinematics in the western pacific derived from geodetic observations. *Journal of Geophysical Research: Solid Earth*, 107(B1):ECV–7.

Tridon, M., Cayol, V., Froger, J., Augier, A., and Bachèlery, P. (2016). Inversion of coeval shear and normal stress of Piton de la Fournaise flank displacement. *Journal of Geophysical Research: Solid Earth*, 121:7846–7866, doi:10.1002/2016JB013330.

Tropp, O., Tal, A., and Shimshoni, I. (2006). A fast triangle to triangle intersection test for collision detection. *Computer Animation and Virtual Worlds*, 17:527–535.

Uieda, L. and Barbosa, V. C. F. (2012). Robust 3D gravity gradient inversion by planting anomalous densities. *Geophysics*, 77:G55–G66, doi:10.1190/geo2011–0388.1.

Uyeda, S., Fuller, M., Belshe, J., and Girdler, R. (1963). Anisotropy of magnetic susceptibility of rocks and minerals. *Journal of Geophysical Research*, 68(1):279–291.

Vening Meinesz, F. (1929). Theory and practice of pendulum observations at sea. *W altman, Delft*.

Vine, F. J. and Matthews, D. H. (1963). Magnetic anomalies over oceanic ridges. *Nature*, 199(4897):947–949.

Von Damm, K., Oosting, S., Kozlowski, R., Buttermore, L., Colodner, D., Edmonds, H., Edmond, J., and Grebmeier, J. (1995). Evolution of east pacific rise hydrothermal vent fluids following a volcanic eruption. *Nature*, 375(6526):47–50.

Wang, D. and der Voo, R. V. (2004). The hysteresis properties of multidomain magnetite and titanomagnetite/titanomaghemite in mid-ocean ridge basalts. *Earth and Planetary Science Letters*, 220(1):175–184.

Wang, S., Chang, L., Wu, T., and Tao, C. (2020). Progressive Dissolution of Titanomagnetite in HighTemperature Hydrothermal Vents Dramatically Reduces Magnetization of Basaltic Ocean Crust. *Geophysical Research Letters*, 47(8):1–11.

Watkins, N. and Paster, T. (1971). The magnetic properties of igneous rocks from the ocean floor. *Phil. Trans. R. Soc. Lond. A*, 268(1192):507–550.

Wei, L.-y. (2014). A faster triangle-to-triangle intersection test algorithm. *Computer Animation and Virtual Worlds*, 25:553–559.

White, W., Klein, E., Holland, H., and Turekian, K. (2014). 4.13-composition of the oceanic crust. *Treatise on geochemistry*, 4:457–496.

Wilkens, R. H., Fryer, G. J., and Karsten, J. (1991). Evolution of porosity and seismic structure of upper oceanic crust: Importance of aspect ratios. *Journal of Geophysical Research: Solid Earth*, 96(B11):17981–17995.

Worm, H.-U. and Banerjee, S. K. (1984). Aqueous low-temperature oxidation of titanomagnetite. *Geophysical Research Letters*, 11(3):169–172.

Wright, S. and Nocedal, J. (1999). Numerical optimization. *Springer Science*, 35(67-68):7.

Yang, K. and Scott, S. D. (1996). Possible contribution of a metal-rich magmatic fluid to a sea-floor hydrothermal system. *Nature*, 383(6599):420–423.

Yang, K. and Scott, S. D. (2002). Magmatic degassing of volatiles and ore metals into a hydrothermal system on the modern sea floor of the eastern manus back-arc basin, western pacific. *Economic Geology*, 97(5):1079–1100.

Yeats, C. J., Parr, J. M., Binns, R. A., Gemmell, J. B., and Scott, S. D. (2014). The SuSu Knolls hydrothermal field, eastern Manus basin, Papua New Guinea: An active submarine high-sulfidation copper-gold system. *Economic Geology*, 109(8):2207–2226.

You, C. F. and Bickle, M. J. (1998). Evolution of an active sea-floor massive sulphide deposit. *Nature*, 394(6694):668–671.

Zhang, H., Yan, Q., Li, C., Zhu, Z., Zhao, R., and Shi, X. (2019a). Geochemistry of diverse lava types from the lau basin (south west pacific): Implications for complex back-arc mantle dynamics. *Geological Journal*, 54(6):3643–3659.

Zhang, J., Yang, Q., Li, J., Meng, X., and Liang, X. (2015). Representation of a velocity model with implicitly embedded interface information. *Computers and Geosciences*, 82:183–190, doi:10.1016/j.cageo.2015.06.012.

Zhang, Y., Mooney, W. D., Chen, C., and Du, J. (2019b). Interface inversion of gravitational data using spherical triangular tessellation: an application for the estimation of the Moon's crustal thickness. *Geophysical Journal International*, 217:703–713, doi:10.1093/gji/ggz026.

Zhao, X., Housen, B., Solheid, P., and Xu, W. (1998). Magnetic Properties of Leg 158 cores: the origin of remanence and its relation to alteration and mineralization of the active TAG mound. *Proceedings of the Ocean Drilling Program, Scientific Results*, 158:337–351.

Zheglova, P. and Farquharson, C. G. (2016). Joint level set inversion of gravity and travel time data: Application to mineral exploration. In *SEG Technical Program Expanded Abstracts 2016*, pages 2165–2169–R30, doi:10.1190/segam2016–13864508.1.

Zheglova, P., Lelièvre, P. G., and Farquharson, C. G. (2018). Multiple level-set joint inversion of traveltime and gravity data with application to ore delineation: A synthetic study. *Geophysics*, 83:R13–R30, doi:10.1190/GEO2016–0675.1.

Zhu, W., Tivey, M. K., Gittings, H., and Craddock, P. R. (2007). Permeability-porosity relationships in seafloor vent deposits: Dependence on pore evolution processes. *Journal of Geophysical Research: Solid Earth*, 112(B5).

Zierenberg, R. A., Fouquet, Y., Miller, D., Bahr, J., Baker, P., Bjerkgård, T., Brunner, C., Duckworth, R., Gable, R., Gieskes, J., et al. (1998). The deep structure of a sea-floor hydrothermal deposit. *Nature*, 392(6675):485–488.